

Wing Design and Analysis for Micro Air Vehicle Development

(versão final após defesa)

Rúben Emanuel Moreira Ferreira

Dissertação para obtenção do Grau de Mestre em
Engenharia Aeronáutica
(mestrado integrado)

Orientador: Prof. Doutor André Resende Rodrigues da Silva

Maiο de 2021

Agradecimentos

Primeiramente, gostaria de agradecer ao meu orientador, Professor Doutor André Resende Rodrigues da Silva pela ajuda, material disponibilizado e a oportunidade de desenvolver este trabalho que tanto me ensinou.

Não esquecendo também o laboratório *AEROG - Aeronautics and Astronautics Research Center*, pela oportunidade de investigação e pelo sentimento de presença nesta grande família. Não existem palavras de agradecimento suficientes para todos os membros do AEROG, especialmente ao aluno de doutoramento Emanuel Camacho por saber ouvir, aconselhar e motivar na realização desta dissertação.

Ao técnico de laboratório, Senhor Rui Manuel Tomé Paulo, gostaria de agradecer pelo auxílio na construção da instalação experimental, assim como ao Professor Abílio Manuel Pereira da Silva pela ajuda e aconselhamento na parte da manufatura. Não poderia deixar de referenciar os conselhos do Professor António Domingos Reis relativos ao sistema elétrico e ao Professor Kouamana Bousson pelas recomendações fornecidas na implementação do filtro do ruído elétrico.

Aos meus amigos mais próximos, gostaria de agradecer pela amizade e suporte ao longo dos anos que passamos juntos na Covilhã. Especialmente, à Ana Oliveira por todo o apoio incondicional, por não me deixar desistir quando as coisas pareciam mais complicadas ao longo desta aventura que foi a dissertação, bem como todo o curso de Engenharia Aeronáutica.

Por último, mas não menos importante, gostaria de expressar a minha gratidão para com toda a minha família e cunhado, em particular aos meus pais, à minha irmã e à minha prima pelo apoio e ajuda proporcionada, apesar da distância.

Resumo

O voo natural sempre funcionou como uma fonte de inspiração para o ser humano, e com isto o ser humano aprendeu com a natureza e por várias vezes tentou reproduzir aquilo que observava. Assim novos desafios apareceram, tal como novas soluções com o desenvolvimento de novas tecnologias, sendo que a área da biomimética foi uma das áreas que ganhou espaço de aplicabilidade e interesse no seio da investigação na comunidade aeronáutica.

O objetivo principal da presente dissertação é a avaliação experimental da influência da forma e estrutura da asa no seu desempenho e comportamento aerodinâmico. De modo a atingir tal objetivo, oito asas foram projetadas (recorrendo a dois métodos diferentes) e posteriormente construídas e testadas a diferentes velocidades de escoamento (0 m/s até 4 m/s) de modo a comparar os resultados com valores de frequência, amplitude, potência média e os seus associados parâmetros adimensionais correspondentes. Após analisar os resultados, foi observado que o intervalo de amplitude se encontrava entre os 0,12 m e 0,27 m, a frequência entre os 4 Hz e os 15 Hz, a potência média entre os 0,7 W e os 1,8 W, e os números de Strouhal e Reynolds com os seus limites inferiores e superiores de 0,15 a 2,2 e $4,2 \times 10^3$ a $2,8 \times 10^4$, respetivamente. É de salientar que as asas projetadas consumiram menos potência por ciclo de batimento com o aumento da velocidade de escoamento, podendo indicar um aumento de desempenho propulsivo.

Palavras-chave

Biomimética; Frequência; Forma da asa; Estrutura da asa; Número de Strouhal

Abstract

Natural flight was always a source of inspiration to the human being, and with this, humans learned from observing it, even trying to reproduce multiple times what they saw. So new challenges emerged, and as new improvements with the evolution of technology, biomimetic gained new applicability, and great interest among the aeronautical scientific research community.

The main objective of the present dissertation is to evaluate experimentally the influence of the shape, and structure in the wing, on their behavior and performance. To accomplish that goal, eight wings were designed (with two different methods), and afterward built, and tested at different airflow speeds (from 0 m/s up to 4 m/s) to compare their results as a function of their frequency, amplitude, average power, and their associated dimensionless parameters. After analyzing the results, it was seen that the amplitude ranges were between 0,12 m and 0,27 m, frequency between 4 Hz and 15 Hz, average power between 0,7 W and 1,8 W, Strouhal and Reynolds numbers have lower and upper limits of 0,15 to 2,2 and from $4,2 \times 10^3$ up to $2,8 \times 10^4$, respectively. Also, it is important to mention that the designed wings produced less power per flapping cycle with the increase of the airflow velocity.

Keywords

Biomimetic; Frequency; Wing Shape; Wing Structure; Strouhal number

Index

Agradecimientos	iii
Resumo	v
Abstract.....	vii
Index	ix
List of Figures	xiii
Nomenclature	xxi
List of Acronyms	xxiii
1.Introduction	1
1.1Motivation	1
1.2 Literature Review	2
1.2.1 Aerodynamic review on flapping-wings	2
1.2.2 Morphing-wing.....	4
1.2.3 Design and morphology of wings	14
1.2.4 Wing manufacturing and materials	24
1.3 Objectives	25
1.4 Outline.....	25
2.Experimental Study	27
2.1 Introduction	27
2.2 Design and construction	27
2.2.1 Design point selection and wing design	27
2.2.2 Structural design.....	30
2.2.3 Manufacturing process	31
2.2.4 Electrical system	33
2.3 Experimental Rig	34
2.3.1 BionicBird by XTIM	35
2.3.2 Wind tunnel	36
2.3.3 Wood support	36
2.3.4 High-speed camera.....	37
2.3.5 Illumination	37
2.3.6 PicoScope	38
2.3.7 Electrical System.....	38
2.3.8 DC power supply.....	39

2.3.9 Anemometer.....	39
2.3.10 Pressure and temperature sensor.....	39
2.4 Results Acquisition.....	40
2.4.1 Methodology.....	40
2.5 Post-processing.....	41
2.5.1 Amplitude and frequency determination.....	41
2.5.2 Data filtering.....	43
2.5.3 Power consumption.....	44
2.5.4 Error propagation estimation.....	44
3.Results and Discussion.....	47
3.1 Introduction.....	47
3.2 High-speed camera tests.....	47
3.2.1 BionicBird original wing.....	48
3.2.2 Rectangular wing & Rectangular wing 2.....	49
3.2.3 Elliptical wing & Elliptical wing 2.....	50
3.2.4 Raven wing & Raven wig m.....	52
3.2.5 Swallow wing & Swallow wing m.....	53
3.3 Picoscope tests.....	55
3.3.1 BionicBird original wing.....	55
3.3.2 Elliptical wing 2.....	56
3.3.3 Swallow wing m.....	57
3.3.4 Elliptical wing.....	58
3.4 Wings Comparation.....	58
3.4.1 High-speed camera tests.....	59
3.4.2 Picoscope tests.....	62
4.Conclusions and Future work.....	66
4.1 Conclusions.....	66
4.2 Future work.....	67
References.....	68
Appendix.....	75
Appendix A - Theta vs Frequency for the nine wings).....	77
Appendix B - Dimensionless amplitude values at U=0 m/s for the nine wings.....	81
Appendix C - Average Power vs Frequency and Dimensionless Power vs Strouhal number for the nine wings.....	85

Appendix D - Dimensionless power values at $U=0$ m/s for the nine wings.....89

List of Figures

Figure 1.1	Da Vinci's ornithopter [1].....	1
Figure 1.2	a) Even though bones from bats and birds are different, they both resist effectively to flight loads, (i.e.), to bending and torsion loads. b) Birds wing folding/extension, wrist flexion/extension and wrist supination/pronation [2].....	3
Figure 1.3	Wingtip paths of different animals. a) albatross, fast gait. b) pigeon, slow gait. c) blowfly. d) locust. e) horseshoe bat, fast flight. f) horseshoe bat, slow gait. g) june beetle. h) fruit fly [3].....	3
Figure 1.4	Snapshots of the modified ornithopter with the passive morphing mechanism applied [6].....	6
Figure 1.5	a) Location of the compliant spine on the ornithopter's wing b) Connection between the compliant spine and the two parts of the rigid spar. The two parts of the spar are connected to the compliant spine by two bolts and glue [7].....	7
Figure 1.6	Comparison between torsional spring of Billingsley et al., the compliant spine from Wissa et al., and a rigid spar. The Y-axis (F) represents the forces during a flapping cycle and the X-axis ($Z_{\text{deflection}}$) represents the compliant spine tip bending deflection [7].....	7
Figure 1.7	a) Lift results of the three different angles on the Delrin housing. b) Thrust results of the three different angles on the Delrin housing [7].....	8
Figure 1.8	a) Stiff hinge folding wing mechanism. b) Flexible Delrin hinge mechanism. c) compliant carbon fiber hinge mechanism [8].....	9
Figure 1.9	Representation of three main stages of the folding of the wing, being fully extended on C, partially extended on B and fully folded on A [9].....	10

Figure 1.10	a) Conceptual design of a wrinkled wing. b) Wing fabricated made of a film with spanwise wrinkles. c) Wing fabricated made of a film with chordwise wrinkles [10].....	11
Figure 1.11	Front view and representation of the flapping cycle of the SmartBird [11].....	11
Figure 1.12	Sideview and representation of half of the flapping cycle of the BionicSwift [13].....	12
Figure 1.13	Comparison between the mechanisms used on the drone and the structure of the bat [14].....	13
Figure 1.14	Representation of the bat-like micro aerial vehicle with NiTi SMA capable of performing active morphing [15].....	13
Figure 1.15	Wing shapes design obtained from birds, and their principal purposes [17].....	14
Figure 1.16	Morphology and platform shape of the wing used during the tests [22].....	15
Figure 1.17	a) Lift coefficient (C_L) as a function of advance ratio (J) of the four different wings. b) Thrust coefficient (C_T) as a function of advance ratio (J) of the four different wings. c) Four different wings with: A - wing with a carbon rod and mylar membrane, B - wing with a carbon rod and paper membrane, C/D - wings with titanium alloy frames and parylene-C membrane [23].....	16
Figure 1.18	Morphology and shape of the four wings used on the tests [24].....	17
Figure 1.19	Morphology of the wings used on the tests [25].....	18
Figure 1.20	Morphology of the wings used on the tests [26].....	18
Figure 1.21	Morphology of the wings used on the tests [27].....	19
Figure 1.22	Compliant wing utilized on the test in [28].....	20

Figure 1.23	Platform shape and spar location of the three wings used on the first test [8].....	20
Figure 1.24	a) Ornithopter Cybird P2, b) Definition of the stroke plane angle (α_{sp}) [29].....	21
Figure 1.25	Platform shape and spar location of the three wings used on the measurement [30].....	21
Figure 1.26	a) Platform shape of the three wings used on the experiments, b) Cross-section of the three wings [31].....	22
Figure 2.1	Process used to design the rectangular wing.....	28
Figure 2.2	Main spar of the rectangular wing.....	31
Figure 2.3	Oven Carbolite used to cure Biresin CR122-3.....	31
Figure 2.4	Glued wings on the first stage of gluing.....	32
Figure 2.5	Glued wings on the second stage of gluing.....	32
Figure 2.6	The 8 pairs of wings that were manufactured.....	33
Figure 2.7	Electrical system.....	34
Figure 2.8	Experimental installation.....	35
Figure 2.9	a) BionicBird By XTIM. b) Components of BionicBird.....	35
Figure 2.10	a) Wind tunnel; b) Wind tunnel frequency controller; c) Wind tunnel guillotine.....	36
Figure 2.11	a) Back view of the wood support; b) Lateral view of the wood support.....	37
Figure 2.12	Photron FASTCAM mini UX50 with Canon EF-S 18-55mm lens.....	37
Figure 2.13	Kaiser video light 6 utilized in the tests [57].....	38

Figure 2.14	PicoScope 2024A used in the tests [58].....	38
Figure 2.15	PeakTech DC Power Supply 6070 used in the tests.....	39
Figure 2.16	Anemometer Airflow TA410 used in the tests.....	39
Figure 2.17	Pressure and temperature sensor used in the experiments.....	40
Figure 2.18	Amplitude, theta and horizontal distance determination.....	42
Figure 2.19	Reference used in $v = 0$ m/s for BionicBird original wing.....	42
Figure 2.20	Connection of the cable of the picoscope to the resistance.....	43
Figure 2.21	Graph of voltage for the Swallow wing for an airflow velocity of 4 m/s at a throttle of 25% with the original data at blue and the filtered that at orange.....	44
Figure 3.1	a) Downward motion of the Swallow wing for an airflow velocity of 1 m/s at a throttle of 50%. b) Upward motion of the Swallow wing at a throttle of 50% for an airflow velocity of 1 m/s	48
Figure 3.2	a) Amplitude vs Frequency at various airflow velocities of BionicBird original wing. b) Dimensionless Amplitude vs Reduced Frequency at different values of Reynolds for BionicBird original wing.....	48
Figure 3.3	Rectangular wings and Rectangular wings 2 shape.....	49
Figure 3.4	a) and c): Amplitude vs Frequency at different airflow velocities of Rectangular wing and Rectangular wing 2, respectively. b) and d): Dimensionless Amplitude vs Reduced Frequency at various values of Reynolds for Rectangular wing Rectangular wing 2, respectively.....	50
Figure 3.5	Shape of Elliptical wing and Elliptica wing 2.....	51
Figure 3.6	a) and c): Amplitude vs Frequency at various airflow velocities of Elliptical wing and Elliptical wing 2, respectively. b) and d): Dimensionless Amplitude vs Reduced Frequency at different values of Reynolds for Elliptical wing and Elliptical wing 2, respectively.....	51

Figure 3.7	a) Shape of Raven wing m. b) Shape of Raven wing.....	52
Figure 3.8	a) and c): Amplitude vs Frequency at various airflow velocities of Raven wing and Raven wing m, respectively. b) and d): Dimensionless Amplitude vs Reduced Frequency at different values of Reynolds for Raven wing and Raven wing m.....	53
Figure 3.9	a) Swallow wing m shape. b) Swallow wings shape.....	53
Figure 3.10	a) and c): Amplitude vs Frequency at various airflow velocities of Swallow wing and Swallow wing m, respectively. b) and d): Dimensionless Amplitude vs Reduced Frequency at different values of Reynolds for Swallow wing and Swallow wing m, respectively.....	54
Figure 3.11	Average power vs Throttle at an airflow velocity of 0 m/s of BionicBird original wing.....	55
Figure 3.12	a) Average vs Frequency of the BionicBird original wing for different airflow velocities. b) Dimensionless Power vs Strouhal number of the BionicBird original wing at various Reynolds numbers.....	56
Figure 3.13	a) Average Power vs Frequency for different airflow velocities of the Elliptical wing 2. b) Dimensionless Power vs Strouhal number at various Reynolds numbers of the Elliptical wing 2.....	56
Figure 3.14	a) Average vs Frequency for various airflow velocities of the Swallow wing m. b) Dimensionless Power vs Strouhal number at different Reynolds numbers of the Swallow wing m.....	57
Figure 3.15	a) Average Power vs Frequency at different airflow velocities of Elliptical wing. b) Dimensionless Power vs Strouhal number of the Elliptical wing at various Reynolds numbers.....	58
Figure 3.16	Amplitude vs Frequency for all wings for an airflow velocity of: a) 0 m/s. b) 1 m/s. c) 2 m/s. d) 4 m/s.....	60
Figure 3.17	Dimensionless Amplitude vs Reduced Frequency, for all wings, at an airflow velocity of: a) 1 m/s. b) 2 m/s. c) 4 m/s.....	61

Figure 3.18	Average Power vs Frequency for all wings at an airflow velocity of: a) 0 m/s. b) 1 m/s. c) 2 m/s. d) 4 m/s.....	63
Figure 3.19	Dimensionless Power vs Strouhal, for all wings, at an airflow velocity of: a) 1 m/s. b) 2 m/s. c) 4 m/s.....	64
Figure A.1	Theta vs Frequency at different airflow velocities for: a) BionicBird original wing. b) Rectangular wing. c) Rectangular wing 2. d) Elliptical wing. e) Elliptical wing 2.....	79
Figure A.2	Theta vs Frequency at different airflow velocities for: a) Raven wing. b) Raven wing m. c) Swallow wing. d) Swallow wing m.....	80
Figure C.1	a), c) and e): Average Power vs Frequency at different airflow velocities for Rectangular wing, Rectangular wing 2 and Raven wing, respectively. b), d) and f): Dimensionless Power vs Strouhal number for Rectangular wing, Rectangular wing 2 and Raven wing, respectively, at different Reynolds numbers.....	87
Figure C.2	a) and c): Average Power vs Frequency at different airflow velocities for Raven wing m and Swallow wing, respectively. b) and d): Dimensionless Power vs Strouhal number for Raven wing m and Swallow wing, respectively, at different Reynolds numbers.....	88

List of Tables

Table 1.1	The history of morphing-wing concepts adapted from [5].....	5
Table 1.2	Materials used on wing membrane, structure and his manufactured technique.....	23
Table 1.3	Materials used on wing membrane, structure, and his manufactured technique (continuation).....	24
Table 2.1	Features of each pair of projected wings and the BionicBird wings. The designation m represents the wings designed using Matlab.....	29
Table 2.2	Main values of each pair of wings that were subjected to experimental tests.....	30
Table B.1	Dimensionless amplitude for the nine wings at $U=0$ m/s.....	83
Table D.1	Dimensionless power for the nine wings at $U=0$ m/s.....	91

Nomenclature

Symbol	Designation	Units
A	Stroke Amplitude	[m]
A_{down}	Down Stroke Amplitude	[m]
A_{up}	Upper Stroke Amplitude	[m]
b	Wingspan	[m]
c	Aerodynamic Mean Chord	[m]
C_L	Lift Coefficient	—
c_r	Root Chord	[m]
C_T	Thrust Coefficient	—
d_{down}	Down horizontal distance	[m]
d_{up}	Upper horizontal distance	[m]
f	Motion Frequency	[Hz]
g	Gravity Acceleration	[ms ⁻²]
h	Dimensionless Amplitude	—
I	Electrical Current	[A]
J	Advance Ratio	—
k	Reduced Frequency	—
m	Mass	[kg]
p	Flapping Period	[s]
P	Atmospheric Pressure	[Pa]
P^*	Reference Power	[W]
r	Resistance Value	[Ω]
R	Ideal Gas Constant	[JK ⁻¹ mol ⁻¹]
Re	Reynolds Number	—
S	Wing area	[m ²]
St	Strouhal Number	—
S_T	Sutherland Temperature	[K]
T	Room Temperature	[K]
T_o	Reference Temperature in Sutherland's law	[K]

U, U _∞	Airflow Velocity	[ms ⁻¹]
V	Voltage	[V]
W	Weight	[N]

Greek Symbols

Symbol	Designation	Units
δA	Amplitude Error	[m]
δc	Ruler Error	[m]
δd	Horizontal Distance Error	[m]
δf	High-Speed Camera Error	[Hz]
δh	Dimensionless Amplitude Error	—
δk	Reduced Frequency Error	—
δP	Air Pressure Sensor Error	[Pa]
δRe	Reynolds Number Error	—
δSt	Strouhal Number Error	—
δT	Temperature Sensor Error	[°C]
δU _∞	Anemometer Error	[ms ⁻¹]
δθ	Stroke Error	[°]
δμ	Dynamic Viscosity Error	[kgm ⁻¹ s ⁻¹]
δρ	Air Density Error	[kgm ⁻³]
θ	Stroke Angle	[°]
θ _{down}	Down Stroke Angle	[°]
θ _{up}	Upper Stroke Angle	[°]
μ	Dynamic Viscosity	[kgm ⁻¹ s ⁻¹]
μ _o	Dynamic Viscosity at T _o	[kgm ⁻¹ s ⁻¹]
ξ	Correction Factor	—
ρ	Air Density	[kgm ⁻³]
ν	Kinematic Viscosity	[m ² s]

List of Acronyms

AoA	Angle of Attack
AWG	Arbitrary Waveform Generator
CFRP	Carbon Fibre Reinforced Plastic
CH	Compliant Hinges
CVD	Chemical Vapour Deposition
FWAV	Flapping-Wing Air Vehicle
FWMAV	Flapping-Wing Micro Air Vehicle
GNATSpar	Gear-driven Autonomous Twin Spar
HECS	Hyper-Elliptic Cambered Spar
MAW	Mission Adaptive Wings
MEMS	Micro-Electro-Mechanical System
PET	Polyethylene terephthalate
PVC	Polyvinyl Chloride
SADE	Smart high lift devices for next-generation wings
SMA	Shape Memory Alloy

Chapter 1

Introduction

This chapter is divided into four subchapters. In the first sub-chapter, the motivation of the dissertation will be discussed, while on the second, the literature review was written with the knowledge found about the subject until recently. In the third and fourth subchapters, the objectives and outline of the dissertation are presented, respectively.

1.1 Motivation

Since the earliest moments in history, humans always had the dream to fly, and with a constant observation of nature, that dream inspired many scientists in the past as Daedalus, that build a set of wings from real feathers, or Eilmer, a monk that was able to glide 200 yards from a tower of Malmesbury Abbey in 1060, or even Da Vinci that designed the first ornithopter powered by man, shown in Figure 1.1.

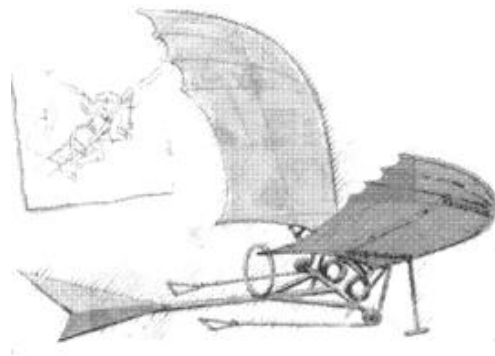


Figure 1.1: Da Vinci's ornithopter [1].

At the time Da Vinci's ornithopter was developed, it was ahead of his time with a mechanical transmission that converted a rowing motion into the vertical flapping movement. Over the last few years and with the improvement of technology, humans are closer than ever to fulfil their dream, and with the help of technology, we can finally understand and in some level replicate what is observed in nature, such as the mechanics of birds and insects flight. Many companies and researchers have devoted their efforts to improve flapping-wing air vehicles (FWAV), such as BionicBird, Festo among others.

1.2 Literature Review

In this subchapter, some topics regarding the research of FWAV will be explored and explained such as:

- Morphing-wing;
- Wing design and morphology;
- Wing manufacturing and materials selection.

1.2.1 Aerodynamic review on flapping-wings

The flapping-wing flight is more intriguing than fixed-wing flight, due to the unsteady flow dynamics and the structural kinematics. Although flapping-wing flight has advantages over fixed-wings, such as high aerodynamic efficiency and maneuverability, at least at lower length and velocity scales.

In nature, flying animals have natural structures, like the ones observed in birds (porous wings) and bats (non-porous wings) that have different bones, being the ones of birds larger in diameter and having a thinner cortical wall so that they can withstand the torsion and bending of the wing during the flight. On the other hand, bats have larger bones closer to the body, small diameter bones farther away and a small thin-walled membrane, giving the wing a lower moment of inertia, which reduces power requirements (Figure 1.2a) [2].

However, in biological flight, wings not only move forward and backward but also up and down, plunge and sweep. While flapping, birds twist one wing downward (pronation), reducing the angle of attack (AoA) while the other wing is twisted upward (supination) (Figure 1.2b) so in that way the bird increases lift. Since the bird can deform and twist its wings in multiple instances, it can adapt its skeletal and muscular systems to the environmental conditions. Besides this the bird can also change the camber and flex the wing spanwise between upstroke and downstroke, increasing its performance during flight.

When flying animals move their wings up and down, they generate both lift and thrust. If they keep their wings stretched, they can still use their gliding mode by using their gravity force as a velocity control system. To a bird/bat maintain level flight, they must produce both lift and thrust, so in that way, its drag keeps the flow direction, and its gravity force keeps vertical direction.

In gliding, the animal body tilts slightly downwards about the air through which it moves. When that happens, the resulting angle between the direction of movement and the air becomes the gliding angle. The gliding angle directly controls the lift-to-drag ratios which typically increases with the Reynolds number, a parameter that varies with the animal size and flight speed. Larger animals will fly at higher Reynolds numbers and generally will have higher lift-to-drag-ratios.

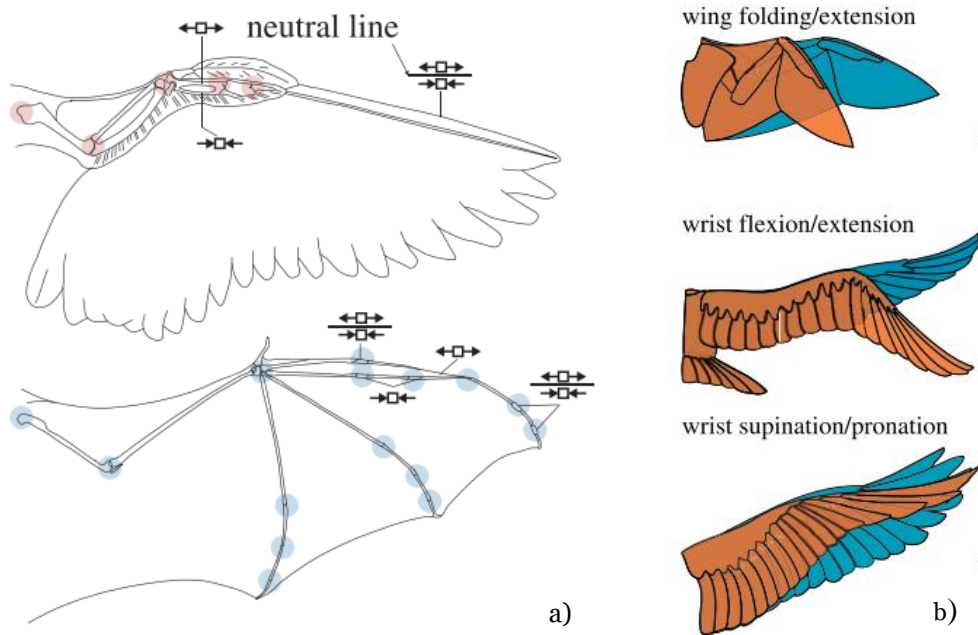


Figure 1.2: a) Even though bones from bats and birds are different, they both resist effectively to flight loads, (i.e.), to bending and torsion loads. b) Birds wing folding/extension, wrist flexion/extension and wrist supination/pronation [2].

To fly at a higher velocity, biological flyers move their wings up and down with higher amplitudes and frequencies, increasing in that way thrust and thus, speed. Biological flyers can apply various flapping patterns, depending on the situation, and the animal. In Figure 1.3 we can observe some animals and their wingtip paths.

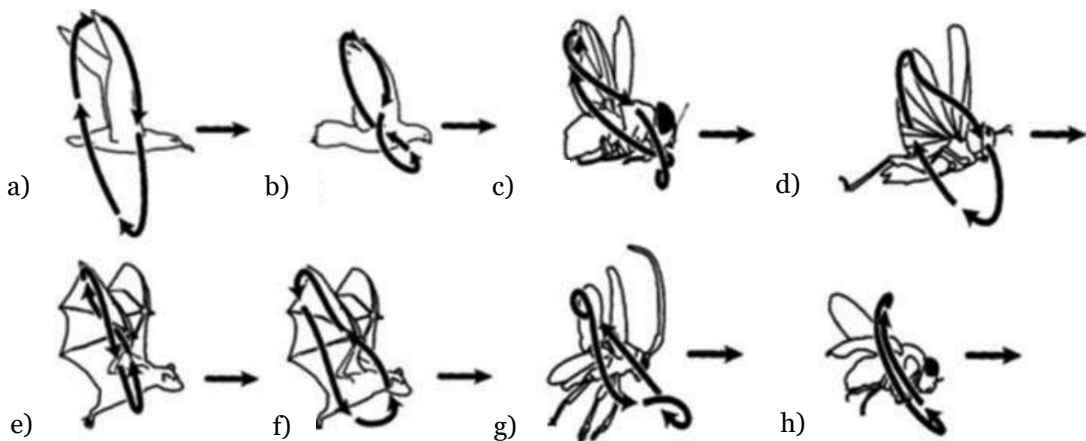


Figure 1.3: Wingtip paths of different animals. a) albatross, fast gait. b) pigeon, slow gait. c) blowfly. d) locust. e) horseshoe bat, fast flight. f) horseshoe bat, slow gait. g) june beetle. h) fruit fly [3].

To quantify the flapping efficiency of flying and swimming animals, a dimensionless parameter is used. This parameter is the Strouhal number and it is defined as [4]:

$$St = \frac{fA}{U_\infty} \quad (1.1)$$

with f being the stroke frequency, A the stroke amplitude and U is the forward speed. Taylor et al. [3] showed that bird flight converges to a St number between 0,2 and 0,4, with this range being considered the optimal range in nature. Further experiments with pitching and heaving foils were performed, and results exhibited a high efficiency on this interval. So, a flapping-wing is to be considered efficient operating at a Strouhal number in that range.

Another important parameter is the reduced frequency (k) and is given by equation (1.2), where f is the motion frequency, c the mean chord, and U_∞ the airflow speed.

$$k = \frac{2\pi fc}{U_\infty} \quad (1.2)$$

The motion amplitude can be divided by the mean chord obtaining the dimensionless amplitude (h) presented in equation (1.3), with A being the stroke amplitude and c the mean chord.

$$h = \frac{A/2}{c} \quad (1.3)$$

Another parameter that governs flapping wing aerodynamics is the Reynolds number which is defined as:

$$Re = \frac{cU_\infty}{\nu} \quad (1.4)$$

with c being the mean chord, U_∞ the airflow speed, and ν the kinematic viscosity.

1.2.2 Morphing-wing

Morphing wings have a good potential to improve the overall performance of aircraft and in our case, ornithopters, just like natural fliers do in nature. Even though this still a recent technology with much more to explore, the results gathered until now seem promising.

There are various types of morphing, but in this dissertation, the two main groups of morphing will be presented, being these:

- Passive morphing;
- Active morphing.

In Table 1.1, we can observe some of the studies conducted until now about morphing.

Table 1.1: The history of morphing-wing concepts adapted from [5].

Year	Information	Concept	Wind tunnel	Flight
1903	Wright Brother's flyer	twist morphing		×
1920	Parker variable – camber wing	variable camber	×	
1979 – 1989	AFTI/F – 111 MAW	variable sweep & camber	×	×
1995 – 1999	Smart wing Program Phase I concepts	variable camber	×	
1996 – 2001	Active aeroelastic wing	variable camber	×	×
1997 – 2001	Smart wing Program Phase I concepts	variable camber	×	
1999	Active hydrofoil	variable camber	×	
1999	Finger concept by DLR	variable camber		
2000	Belt – rib concept by DLR	variable camber		×
2000	FlexSys mission – adaptive compliant wing	variable camber	×	×
2003 – 2006	Lockheed Martin Z – wing concept	folding wing	×	
2003 – 2006	NextGen aeronautics bat – wing concept	variable sweep	×	
2003	SMA reconfigurable aerofoil	variable camber	×	
2003	HECS wing	span morphing		
2004	Multi – section variable – camber wing	variable camber	×	
2004	Variable – gull – wing morphing aircraft	folding wing		×
2004	Virginia Polytechnic Institute and State University telescoping-wing aircraft	span morphing	×	×
2005	Morphing inflatable wing	variable camber & twist morphing	×	×
2006	Morphing HECS wing	variable sweep & twist morphing	×	
2007	Pneumatic telescoping wing	span morphing	×	
2007	Supekar morphing wing	span morphing	×	
2008	Antagonistic SMA-based morphing aerofoil	variable camber		
2008	Bistable composite morphing-wing concepts	variable sweep		
2008	Morphlet (morphing winglet)	folding wing		
2009	Adaptive wing with SMA torsion actuators	variable camber		
2010	Warp-controlled twist morphing wing	twist morphing		
2011	Spa extending morphing wing	span morphing	×	
2012	Multisegmented Folding Wing	folding wing	×	
2012	SADE: seamless aeroelastic wing	variable camber		
2013	Adaptive bending–twist coupling wing	twist morphing		
2013	Bat-like morphing-wing	folding wing	×	
2014	Compliant adaptive wing leading edge	variable camber		
2015	Span-extending blade tip	span morphing		
2015	variable-span morphing wing	span morphing	×	
2015	Spanwise morphing trailing edge	variable camber	×	
2016	GNATSpar wing	span morphing	×	
2016	Twist morphing wing segment	twist morphing	×	
2016	morphing wingtip	variable camber	×	
2016	Compliant structures-based wing and wingtip morphing devices	variable camber	×	
2017	Feathered wing	folding wing		×
2017	Aquatic micro air vehicle	variable sweep		×

Passive morphing wing

Some engineers inspired themselves on nature, seeing that birds fold their wings toward their bodies during the upstroke, decreasing the air resistance, and consequently reducing the magnitude of negative lift forces. On the other side, during the downstroke, the bird fully extends his wings, so it can increase the wing area and consequently produce more lift.

Billingsley et al. [6] applied morphing to a modified version of the Park Hawk series of the ornithopter created by Sean Kinklade. He accomplished this by installing a unidirectional torsional spring on the primary wing spar, allowing the angular deflection and mimicking the function of an elbow. Besides this, he also applied a small bridge of aluminum above the torsional spring. This would prevent the wing from bending when moving downwards and when moving upwards the wing would fold, reducing the wing area and reducing the negative lift forces. On the other hand, when the wing moves downwards the wings would be fully extended and thus increase lift production. In Figure 1.4 we can see the upward and downward movement of the wings of the ornithopter with the morphing mechanism applied by Billingsley et al.

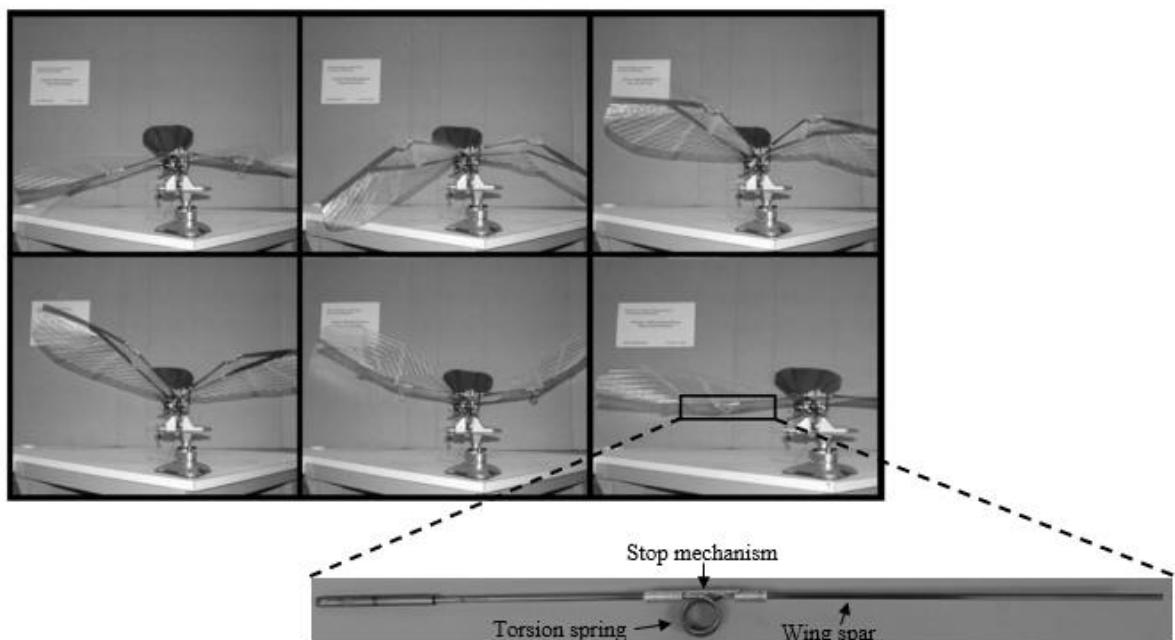


Figure 1.4: Snapshots of the modified ornithopter with the passive morphing mechanism applied [6].

While testing, Billingsley et al. noticed that with the passive morphing mechanism, the wing produced more than 300% net lift, but had a great penalty on the produced thrust, resulting in a slower ornithopter, that would initially fly forward but after that it would slow down to the hover condition, descending towards the ground afterwards. This means that the ornithopter did not have enough velocity to produce lift and forward flight.

In [7], Wissa et al. developed a novel compliant spine for passive morphing (Figure 1.5) that was very stiff during the downstroke and flexible during the upstroke. This happens because when the wing moves downward the segments of the compliant spine come in contact with each other, not allowing the wing to bend. When the wing moves upward, the space between the gaps is increased and the semi-circular compliant hinges (CH) do not allow the wing to bend in excess but allows them to bend the necessary to decrease the wing area hence diminishing the negative lift.

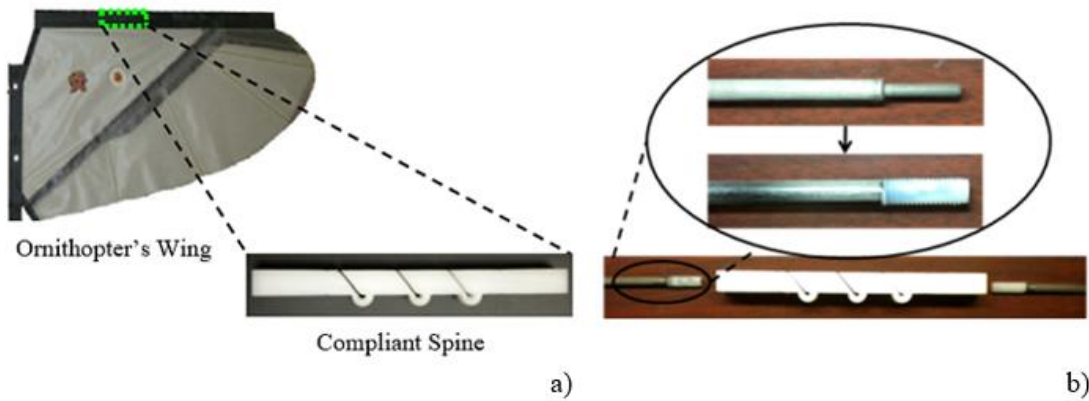


Figure 1.5: a) Location of the compliant spine on the ornithopter's wing b) Connection between the compliant spine and the two parts of the rigid spar. The two parts of the spar are connected to the compliant spine by two bolts and glue [7].

With this mechanism, at 37% of the wing half span, Wissa et al. noticed that the ornithopter consumed 45% less power, got an additional 16% in lift gain, and flapped at a higher frequency when compared with the ornithopter without the compliant spine. In Figure 1.6 we can see a comparison of the torsional spring of Billingsley et al., the compliant spine from Wissa et al., and a rigid spar. So, as we see on the graph, the compliant spine joins the best of two worlds, since it acts as a rigid spar during the downstroke, preventing excessive bending, and acts as a torsional spring during the upstroke, promoting the bending.

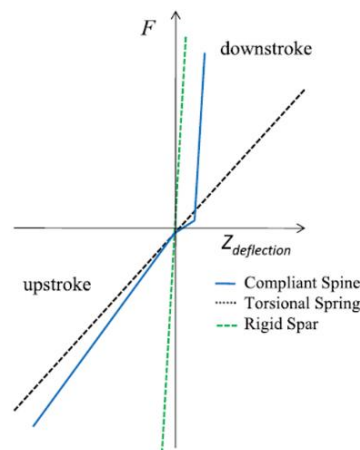


Figure 1.6: Comparison between torsional spring of Billingsley et al., the compliant spine from Wissa et al., and a rigid spar. The Y-axis (F) represents the forces during a flapping cycle and the X-axis ($Z_{deflection}$) represents the compliant spine tip bending deflection [7].

Mueller et al. [8] designed and tested three different compliant passive morphing mechanisms. The first mechanism presented on the paper was composed of a Delrin hinge that was designed to limit the motion of the carbon fiber spar attached to the pinned joint as we can see in Figure 1.7 a). This first mechanism was tested for three different angles on the Delrin housing. Since there is no spring or resistance on the pinned joint, the carbon fiber spar moved freely with the aerodynamic loadings, so that when the wings move downward the carbon fiber spar moves up, due to the aerodynamic loadings on the spar, and then hits the Delrin; this will make the wing re-extend. During the upstroke the carbon spar moves down, because of the aerodynamic loadings on the spar, and hits the Delrin; this makes the wing fold. This mechanism was tested for three different angles on the Delrin housing, 15°, 25°, and 35°, with the angle equal to 35° being the one that got higher values of lift and the angle equal to 15° being the one with the higher values of thrust, as we can see on Figure 1.7 a) and b).

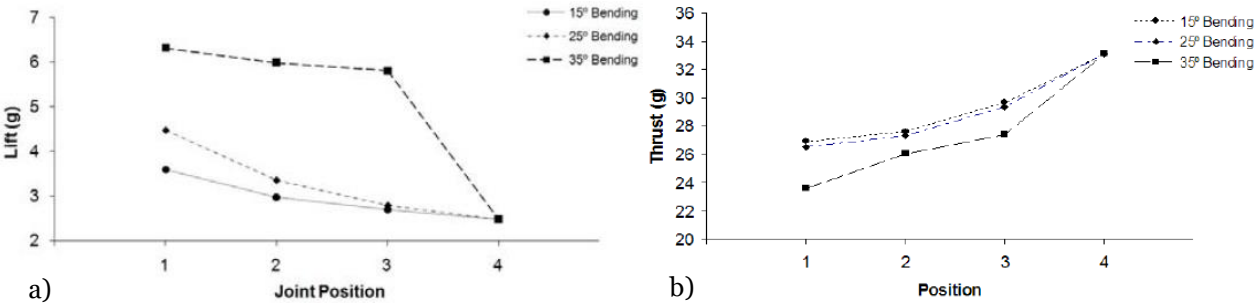


Figure 1.7: a) Lift results of the three different angles on the Delrin housing. b) Thrust results of the three different angles on the Delrin housing [7].

On the second mechanism, presented in Figure 1.8 a), we can observe that the mechanism is composed of a Delrin part that was designed to act as a folding member, (i.e.), the carbon fiber spar coming from the ornithopter body is inserted on the Delrin part, as shown in Figure 1.8 b), and the carbon fiber spar that goes to the wingtip in inserted on the other side of the Delrin. When the wing moves downward the Delrin finds bending resistance on the carbon fiber spar and keeps the wings stretched. During the upstroke, the Delrin bends because of its lower thickness, and the wings fold.

In Figure 1.8 c) the third mechanism designed by Mueller et al. [8] may be seen. This mechanism has the carbon fiber spar coming out of the Delrin, it also as a compliant carbon fiber spar, with a smaller diameter, and another Delrin part, connected to the main carbon spar, that leads to the leading edge, and to the carbon fiber spar with a smaller diameter. During the downstroke and upstroke, this mechanism works in the same way as the one in Figure 1.8 b).

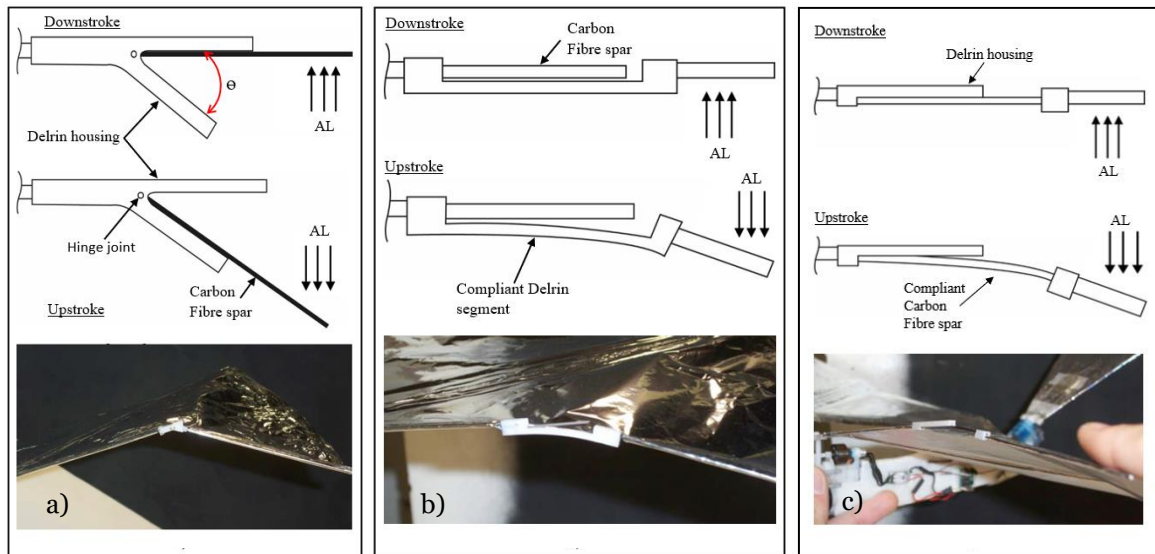


Figure 1.8: a) Stiff hinge folding wing mechanism. b) Flexible Delrin hinge mechanism. c) compliant carbon fiber hinge mechanism [8].

When conducting tests, Mueller et al. observed that the ornithopter with morphing-wings does not compromise the overall lift and can maintain the payload capacity, even though it reduces the ornithopter forward velocity by about 30% and his climb rate by 50%, when compared to a non-folding wing ornithopter.

Stowers et al. [9], built a passive morphing mechanism that consists of an unactuated hand wing connected to the wing arm with a wrist joint (Figure 1.9). Their investigation consisted of the unfolding behavior of the wings and the situations where wings impacted at constrains with different speeds and different flapping frequencies, promoting the folding of the wings. Their results showed that the unfolding of the wing was related to the centrifugal accelerations generated by the flapping motion, contradicting Mueller et al. [8], which affirmed that passive morphing was mainly caused by aerodynamic forces.

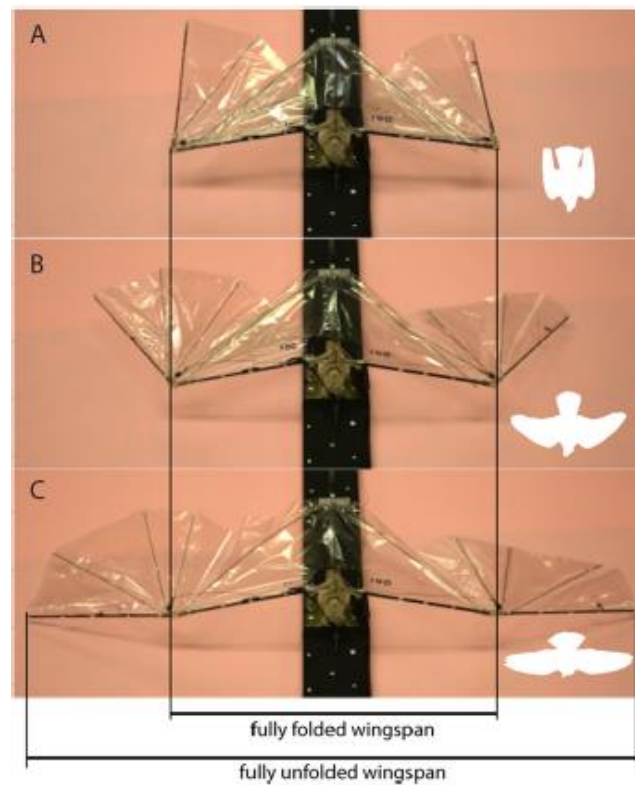


Figure 1.9: Representation of three main stages of the folding of the wing, being fully extended on C, partially extended on B, and fully folded on A [9].

Tanaka et al. [10], tested a different type of wing made with carbon fiber reinforced plastic (CFRP) frames and a parylene-C membrane with microscale wrinkles (Figure 1.10 a), one with unidirectional wrinkles in the chordwise direction (Figure 1.10 c) and other with unidirectional wrinkles on spanwise direction, as we can see on Figure 1.10 b. These wrinkles were designed to enhance the flexural stiffness and diminish the tensile stiffness of the wing. The results showed that chordwise unidirectional wrinkles could prevent fluttering near the trailing edge and produce more lift compared with the flat wing and the wing with spanwise unidirectional wrinkles. Even though there are some flaws, since there is not much experimental support on the reduction of the tensile stiffness using this technology, it may show us a new way to fabricate morphing-wings.

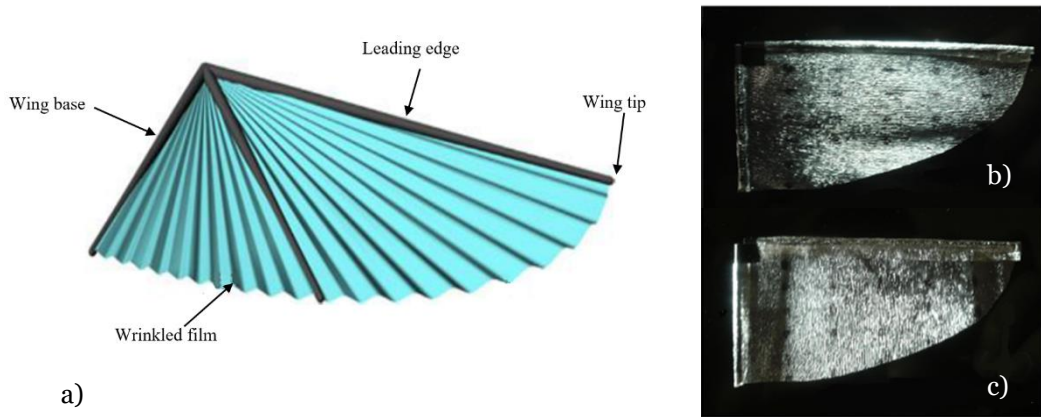


Figure 1.10: a) Conceptual design of a wrinkled wing. b) Wing fabricated made of a film with spanwise wrinkles. c) Wing fabricated made of a film with chordwise wrinkles [10].

Active morphing wing

Nowadays, active morphing wings are essentially used on fixed-wing aircraft, for example on airplane flaps. In FWAV this is still a new technology with very much potential to be explored. One of the recent advances in this area is the smart materials because they would reduce the need for additional weight (traditional ways would require the use of DC motors to synchronize both flapping and morphing), that active morphing wing usually demands.

One of the biggest examples of this kind of morphing is the Festo SmartBird [11,12], shown in Figure 1.11. Inspired on a seagull, it has a wingspan of 2 meters, a mean chord of 0,25 m, and its wings flap at an average frequency of 2 Hz, flying at a speed of 5 m/s. Each wing of Festo Smart Bird was built with two main parts: an arm wing spar and a hand wing spar and besides these two parts, there is also a trapezoidal joint and a pivot axis located on the torso. The two main parts of the wing have different functions, with the wing arm producing lift and the hand wing producing thrust.



Figure 1.11: Front view and representation of the flapping cycle of the SmartBird [11].

The Smart bird also has active torsion and partial linear kinematics, meaning that when their wings move upward, the servomotor (located on the end of the outer wing) twists the wingtip of the outer part of the wing to a positive AoA, which is afterward replaced by a negative AoA on the same flapping cycle.

Another recent creation of Festo is BionicSwift [13] and just like its name suggests, it is based on a swift and represented in Figure 1.12. It has a wingspan of 68 cm and weighs 42 g. Their wings are built with various lamellae (to replace traditional feathers) made of ultralight and flexible foam; with this kind of design the BionicSwift needs less power to oscillate the wing, since when the wings move upward the individual lamellae turns sideways to let the airflow through the wing, reducing aerodynamic resistance, and when the wings move down the lamellae keeps straight increasing lift and thrust of the BionicSwift.

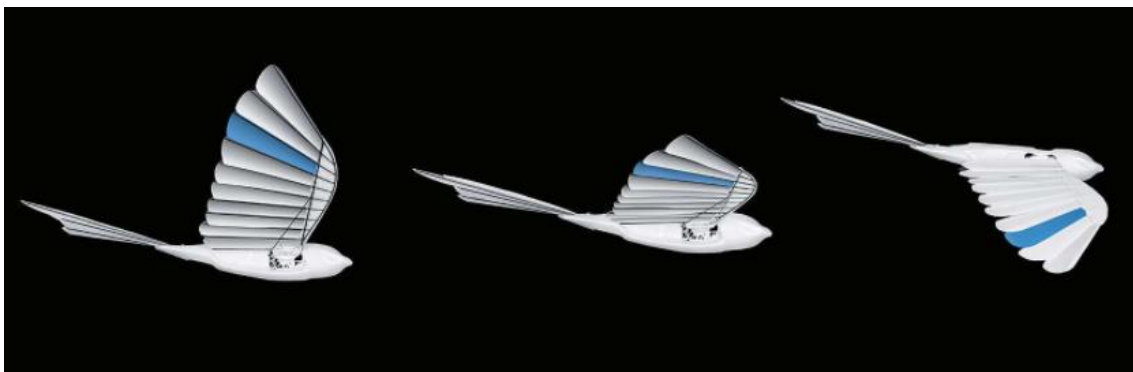


Figure 1.12: Sideview and representation of half of the flapping cycle of the BionicSwift [13].

This drone also has an advanced control system, as it can adjust the tail AoA and the frequency of the flapping cycle to complete the different maneuvers.

As mentioned before, some authors use smart materials to decrease the overall weight of the FWAV. One example is Bunget et al. [14], which used a shape memory alloy (SMA) on a bat-inspired flapping air vehicle. SMA wires were used to mimic animal muscles, while the hinges were built to make use of the superelasticity of the SMA.

In Figure 1.13 we can observe the superelastic flexible hinges used on the bat-inspired flapping air vehicle as well as SMA wires, shown in red.

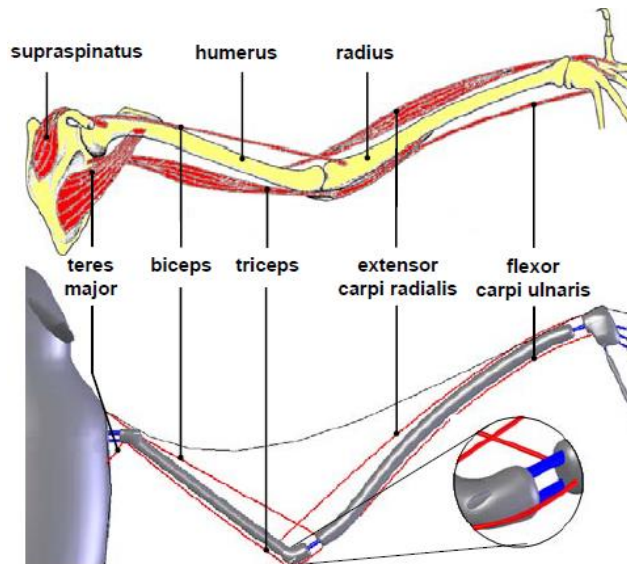


Figure 1.13: Comparison between the mechanisms used on the drone and the structure of the bat [14].

In [15], Colorado et al. designed and fabricated a bat-like micro aerial vehicle (Figure 1.14) with NiTi SMA acting as artificial muscles, and in that way being able to mimic the movement made by bats during flight. One of the main objectives was to use the electricity in the drone to adjust the morphing wing motions for each desired movement, retracting or extending.

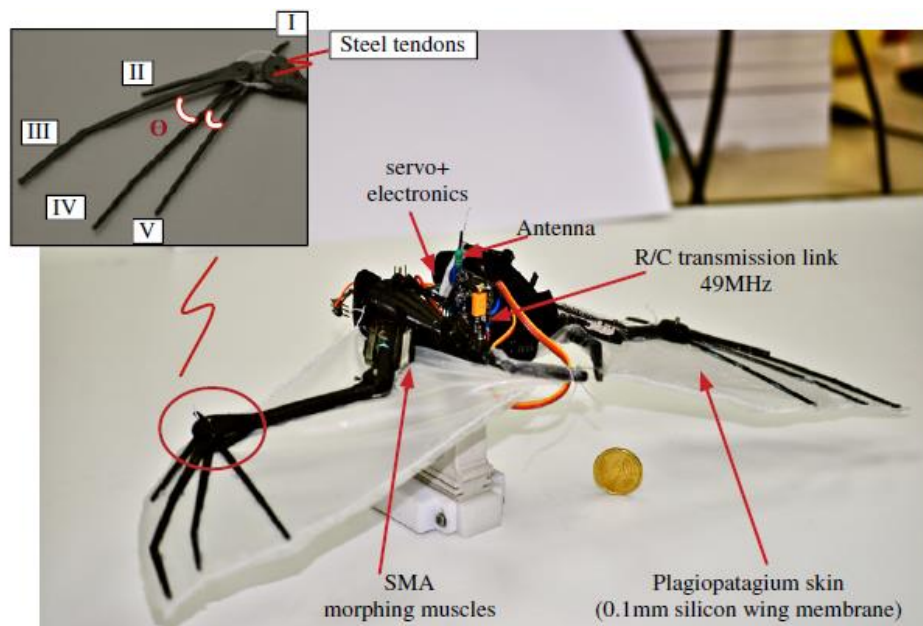


Figure 1.14: Representation of the bat-like micro aerial vehicle with NiTi SMA capable of performing active morphing [15].

Colorado et al. after performing some experiments concluded that with the morphing mechanism, this bat-like micro aerial vehicle was capable of a cruising speed of 5 m/s at a frequency of 2.5 Hz.

1.2.3 Design and morphology of wings

The process of choosing and designing wings to an ornithopter is a process that requires time and knowledge. Most engineers get their ideas from nature, observing the different birds and recognizing how their wings are (their shape and aspect ratio) and what use each bird gives to these structures, because each bird uses their wings on their own way, for their own profit, (i.e.), for each flight phase the bird will adapt as necessary. Usually, most birds follow one of the six flapping styles according to the shape of their wings [16,17]:

- short, broad, cupped wings for fast take-off and short-haul flight;
- short and broad wings with grooved primary feathers for soaring;
- flat moderately long, thin, and triangular wings for maneuverability and high-speed flight;
- long, thin, high, and flat pointed wings for long-distance and gliding flight;
- pointed and rollback wings for hovering or motionless flight.

In Figure 1.15 we can observe some of the possible wing shapes planforms that are observed in birds in their flapping flight and their flight purpose.

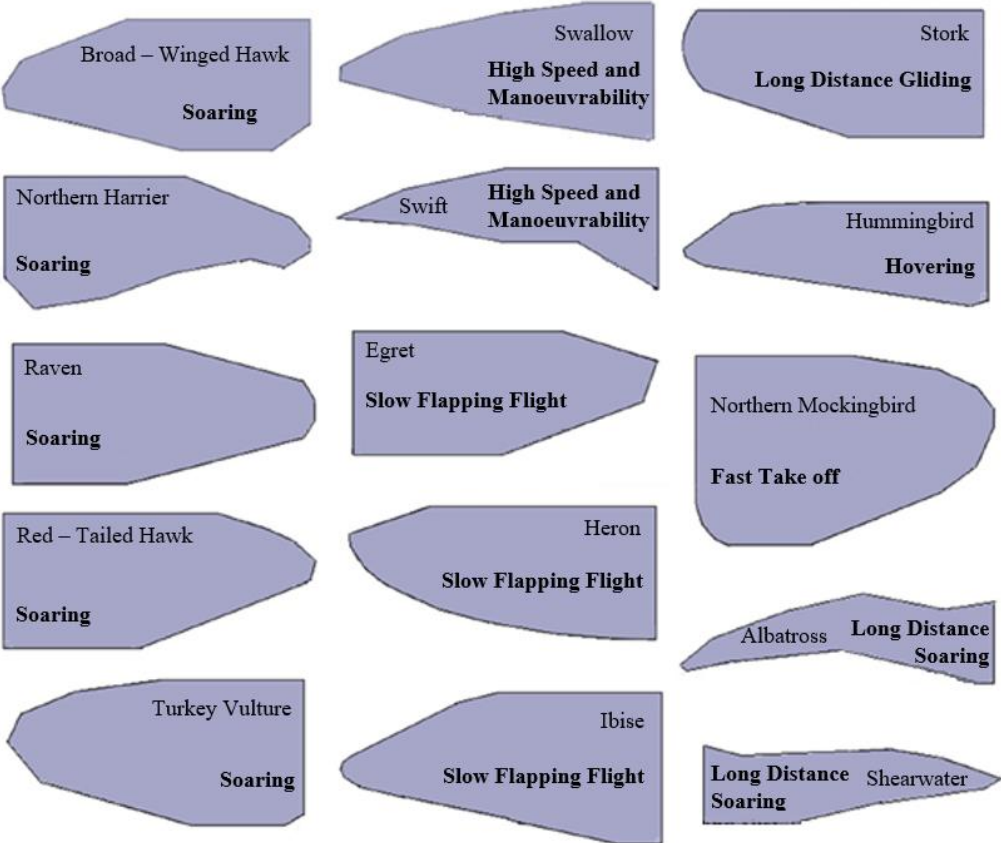


Figure 1.15: Wing shapes design obtained from birds, and their principal purposes [17].

Some investigators like Barata et al. [18,19], focused their studies on the take-off, landing phases and locomotion of animals, investigating more deeply the existing forces during take-off and mechanisms used in the locomotion of animals, concluding that the bird used in the tests can

generate against perch four times their weight on take-off and that both thrust and lift should not be considered separately, respectively.

On the other hand, Pennycuick [20] observed different species of low-frequency birds, with a frequency no more than 13 Hz. With these observations the author gathered 47 samples on cruising flight, that were used to obtain the equation below, helping to estimate the flapping frequency.

$$f = m^{\frac{3}{8}} g^{\frac{1}{2}} b^{-\frac{23}{24}} S^{-\frac{1}{3}} \rho^{-\frac{3}{8}} \quad (1.5)$$

m is the body mass, g is the gravity acceleration, b is the wingspan, S is the alar load, and ρ the air density. Based on the equation, f increases with the increase of m and g , and decreases with the increase of b , S and ρ .

Afterward Hassanalian et al. [17] modified Pennycuick equation so it could be used for flapping-wing micro air vehicles (FWMAV) at low flapping frequency. The modification consisted of the addition of a correction factor ξ as observed on the equation (1.6), that varies with the type of the FWMAV, and its value is recommended to be between 1.2 and 4.7.

$$f = \xi m^{\frac{3}{8}} g^{\frac{1}{2}} b^{-\frac{23}{24}} S^{-\frac{1}{3}} \rho^{-\frac{3}{8}} \quad (1.6)$$

On the other hand, Greenwalt et al. [21], proposed a correlation between wing flapping frequency (f) and wingspan (b) based on statistical data and is shown in equation (1.7).

$$fb^{1.15} = 3.54 \quad (1.7)$$

While Pennycuick [20] and Greenwalt [21] based their studies on statistical data to develop equations (1.5) and (1.7) respectively, other authors decided to test different characteristics of ornithopters wings like Hu et al. [22], that designed and tested three wings with different membrane materials, wood, nylon, and latex, so that they could evaluate the influence that the membrane material could have on the production of lift and drag. All three wings have the same rigid glass fiber frames, the same elliptical platform shape, and dimensions, as we can observe in Figure 1.16. The rigid wing (wood wing) was only used for comparison with the other two wings, for more accurate results on the impact of the flexibility of the membranes.

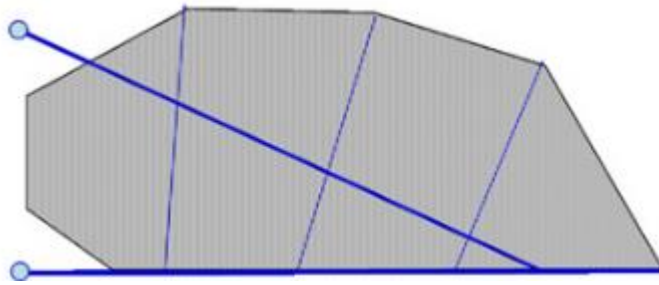


Figure 1.16: Morphology and platform shape of the wing used during the tests [22].

The tests showed that flexible membrane wings had better overall aerodynamic performance (i.e. lift-to-drag ratio) in comparison with the rigid wing for soaring flight. This happened especially for higher velocities or considerably high AoA, although the rigid wing had better lift production for flapping flight in general. The latex wing had the biggest flexibility of the three wings and presented the best thrust values for flapping flight, while the nylon wing had the best overall aerodynamic performance for soaring flight. However, the nylon wing had the worst values regarding flapping flight performance.

Pornsir-Sirirak et al. [23], designed and fabricated four different wings, being divided into two groups: the ones that used MEMS-based wing technology and the ones that did not. The two wings that did not use MEMS-based wing technology were fabricated with carbon fiber rods and paper/mylar as wings membranes and the wings that were using MEMS-based wing technology were fabricated with a parylene-C wing membrane and titanium-alloy wing frames, as it can be observed on Figure 1.17 c).

As we can observe in Figure 1.17 a) and 1.17 b) wings B and D had higher lift coefficients at lower advance ratios while wings C and D had higher thrust coefficients. Tests showed that the wing D showed the best results in terms of lift, thrust, and power required, and could be actuated until 30 Hz of flapping frequency.

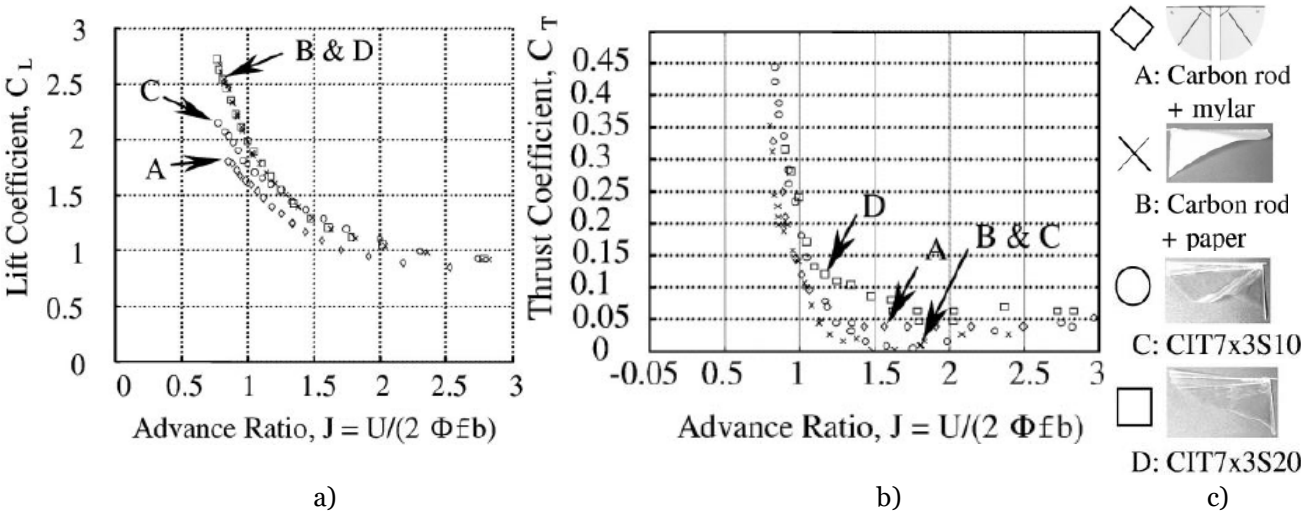


Figure 1.17: a) Lift coefficient (C_L) as a function of advance ratio (J) of the four different wings. b) Thrust coefficient (C_T) as a function of advance ratio (J) of the four different wings. c) Four different wings with: A - wing with a carbon rod and mylar membrane, B - wing with a carbon rod and paper membrane, C/D - wings with titanium alloy frames and parylene-C membrane [23].

The MEMS wings technology showed us a new way of fabricating wings, with a lighter and stronger material (parylene-C as the membrane) capable of withstanding higher frequencies, presenting in this way a more efficient wing as we observed before.

On reference [24], Ghommem et al. designed and tested four wings on a biplane flapping-wing nano air vehicle. All the wings had the same wing shape, area and were all fabricated with mylar film on the membrane and carbon rods as stiffeners, being their difference the location of the stiffeners, as we can see in Figure 1.18.

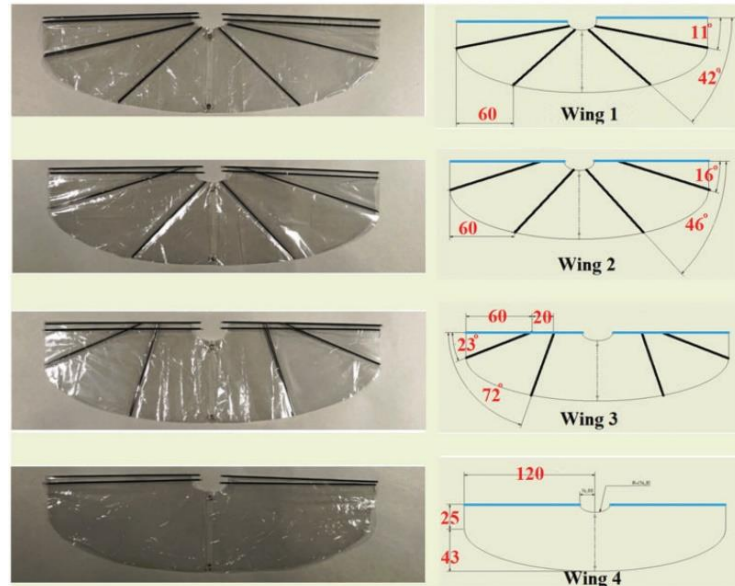


Figure 1.18: Morphology and shape of the four wings used on the tests [24].

There were two main tests: on the first one, Ghommem et al. measured the thrust produced as a function of the flapping frequency, and on the second one, they measured the power consumption as a function of the flapping frequency. Results showed that on the first test, the first wing had the best overall performance, i.e., produced higher thrust for almost the full range of flapping frequencies (20 Hz to 47 Hz). On the second test, experimental measurements showed that the fourth wing is the one that spends less power for the full range of the flapping frequency. Combining the two studies Ghommem et al. presented thrust-to-power ratio and considered it as the performance indicator, seeing that the first wing showed the best overall results, being considered the optimal wing with the best location for the stiffeners.

Mazaheri et al. [25, 26], designed, fabricated, and tested different wings. In [25], there were two main tests: on the first test the objective was to understand the effect of the variation of the structural stiffness of the wing on the aeroelastic performance of the wing. To do that Mazaheri et al. constructed 5 wings with the same structure (shown in Figure 1.19) and materials but with different rib thickness, with wing 1 having a rib thickness of 0,7 mm, and wing 5 a rib thickness of 4 mm. They obtained the power usage, the thrust and the thrust-to-power-usage of the wing as a function of the flapping frequency, evaluating the best wing for hovering flight. On the second test, Mazaheri et al. only tested wings 1,3, and 5 on his experiments, and calculated the thrust, the cruise speed, and the thrust-to-power-usage as a function of the flapping frequency, to estimate the best wing for cruise flight with a wind tunnel velocity of 8 m/s.

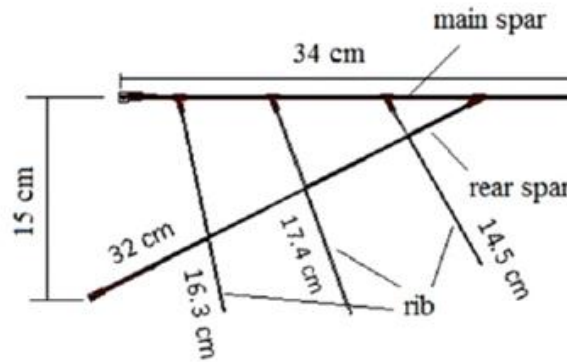


Figure 1.19: Morphology of the wings used on the tests [25].

Results showed that wing 1 has the least power consumption but has the least thrust production of all the considered wings. On the other hand, wing 5 has the best thrust production but also has a larger power consumption. The biggest difference appeared on the thrust to power usage as a function of the flapping frequency, where the performance of wing 1 was about 30% better than the wing 3 and 5 and slightly better than the wing 2 and 4. On the cruise flight test, the results showed that wing 1 had the best results on all experiments (thrust, cruise speed, and thrust-to-power-usage). With these tests, Mazaheri et al. affirmed that the more flexible wings have about 20% less thrust production for higher frequencies but have more than 30% on the overall wing performance, for hovering flight, when compared to more stiff wings.

Mazaheri et al. [26], performed tests on a low-speed wind tunnel to measure the lift and thrust of the membrane of the flapping-wing for different AoA and multiple flow speeds. Following the steps mentioned in [25], Mazaheri et al. [26] used the same wing structure as wing 1 (Figure 1.19) and the shape of the membrane is represented in Figure 1.20.

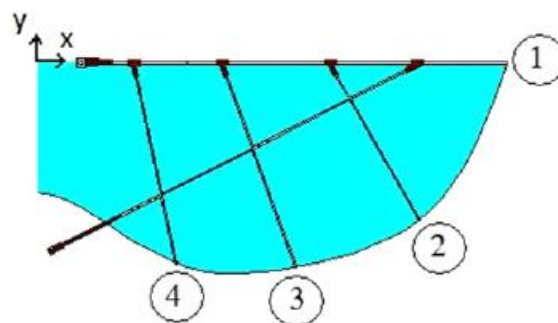


Figure 1.20: Morphology of the wings used on the tests [26].

Results showed that thrust increases with the increase of the flapping frequency but is higher for the lower velocities of the flow, and smaller AoA. On the other side, lift increases linearly with AoA and for low AoA, it almost has a quadratic relationship at high flapping frequencies.

Lin et al. [27] designed, manufactured, and tested two wings with different morphology, as we can see in Figure 1.21, but with the same materials. Another main difference of the wings is their span, while the wing in Figure 1.21 a) has a span of 60 cm, the wing in Figure 1.21 b) has a span of 40 cm.

The main objective was to measure the lift and thrust of the mechanical membrane on the flapping wing with different frequencies, speeds, and AoA. All the experiments were made on a wind tunnel and used the same flapping mechanism. Both wings were manufactured using the same materials (epoxy reinforced carbon fiber composite frames and PVC plastic film membrane).



Figure 1.21: Morphology of the wings used on the tests [27].

According to Lin et al. while testing wing a), the lift value stayed almost constant for an AoA of 0° for the various frequencies, and increases with the increase of wind speed, while for an AoA of 15° , the lift value increases with the increase of wind speed and with the increase of frequency. On the other hand, the lift values of wing b) increase with the increase of frequency and wind speed for an AoA of 15° . Other results showed that both wings, with a fixed frequency, would increase the lift force while increasing the wind speed and AoA.

On the other side, thrust increases for wing b) with the increase of frequency and wind speed for an AoA of 15° , while for wing a) increases with the increase of wind speed until a certain frequency, decreasing afterward for an AoA of 15° . In the last experiment, Lin et al. showed that flying speed is higher for smaller AoA and increases with frequency.

Mueller et al. [28], designed a compliant wing intending to compare the differences of thrust and lift at different frequencies, and besides, observed the effect of compliance on the generation of extra thrust and lift at the beginning and end of upstrokes and downstrokes of the flapping motion.

In Figure 1.22 it can be observed the compliant wing used in the test as its spars. The primary spar helps to control the stability of the wing at high frequencies and changes the effective velocity of the mid chord points of the wing as the projected wing area along the flapping axis.

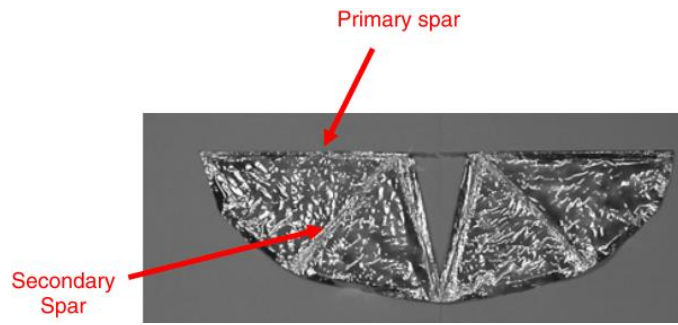


Figure 1.22: Compliant wing utilized on the test in [28].

Results showed that the higher the frequency, the bigger is the value of thrust and lift, and that with the compliant wing, and its reduction of 20 degrees between the upstroke and the downstroke, reduced the drag force by 40%, even though velocity suffered a loss of 25%.

Mueller et al. [8] designed, manufactured, and tested three wings with the same material on the membrane and spars, but with a different number of spars and their location, to evaluate the thrust generated and the flapping rate of the wings.

Several experiments were made to find the best wing for the ornithopter. On the first test three wings (Figure 1.23) were tested to find the one with the best thrust production and lower flapping rate. Wing 1 has one leading edge spar, the wing 2 has two spars, the one on the leading edge and another one with a 60° angle to the leading edge, while the wing 3 has two spars, one on the leading edge and another one with a 30° angle to the leading edge.

In the second experiment, Mueller et al. constructed multiple wings with different sizes to investigate the lift and thrust generated as a function of the wing dimension.

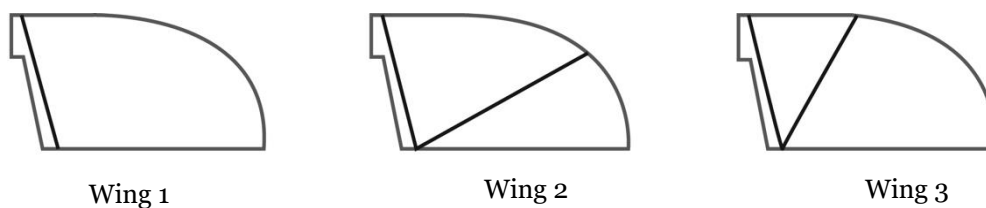


Figure 1.23: Platform shape and spar location of the three wings used on the first test [8].

Results on the first experiment showed that wing 2 and wing 3 produced more thrust than wing 1, even though, the wing that produced higher thrust was wing 3. On the other hand, wing 2 had a lower value of flapping frequency, having less 0,5 Hz than the other wings, but as one of the objectives was to reduce the noise generated, having a lower flapping rate would help to accomplish this goal. In the second experiment Mueller et al. observed that frequency and lift decreased almost constantly with the increase of the wing area, while thrust increased almost constantly with the increase of the wing area.

Krashanitsa et al. [29] performed some tests with a modified Cybird P2 (Figure 1.24 a) ornithopter, on a wind tunnel with the control surfaces, fixed in the stable position and with a motor at a constant throttle setting to control the flapping motion of the wings.

All coefficients were estimated using the same conditions (a stream velocity of 7.25 m/s and a stroke plane vary from 0° to 40°), with the stroke plane condition being presented in Figure 1.24 b).

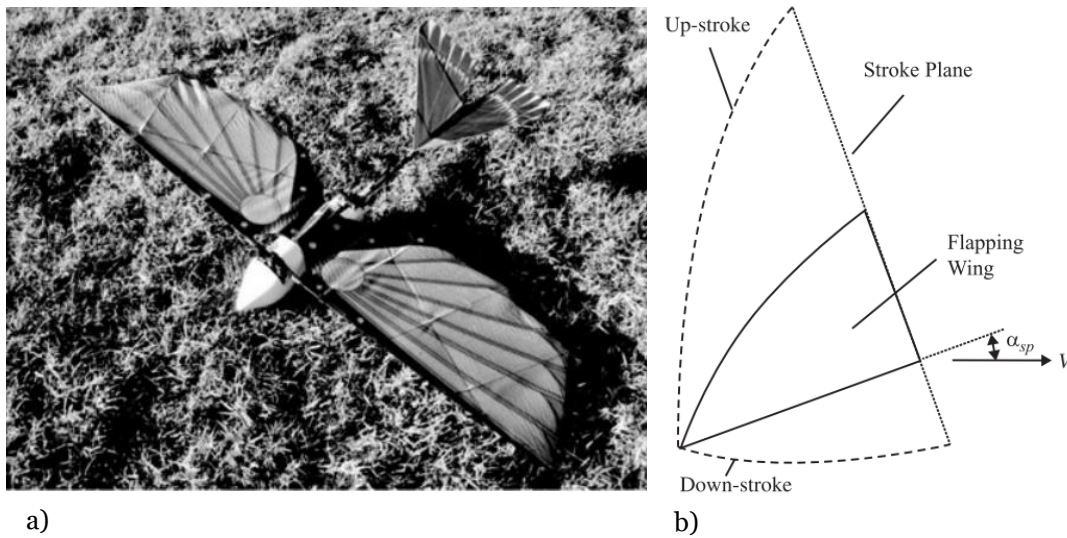


Figure 1.24: a) Ornithopter Cybird P2, b) Definition of the stroke plane angle (α_{sp}) [29].

Results of Krashanitsa et al. experiments showed that flapping frequency and free stream velocity increased with the increase of throttle, while the increase of the α_{sp} represented a decrease of the flapping frequency and increased with the increase of the throttle. The pitching moment is almost independent of the throttle and decreases with the increase of α_{sp} .

In [30], Yang et al. manufactured, designed, and tested three wings built with the same materials and fabrication process but with different morphology which presented in Figure 1.25. The tests consisted of measuring the span/chord-wise bending as a function of the flapping angle of the wing and measuring lift and thrust during the flapping cycle.

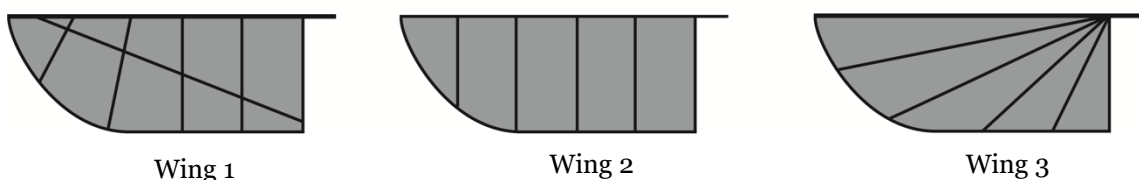


Figure 1.25: Platform shape and spar location of the three wings used on the measurement [30].

According to Yang et al., wing 1 obtained the maximum lift and the mid-value of thrust production of the three wings while on the span/chordwise bending it had the mid-value of the three wings. Wing 2 had the highest value of span/chordwise bending and thrust production but had the lowest value on lift production of the three wings. On the other hand, wing 3 had the lowest value of

span/chordwise bending and thrust production and had the mid-value on the lift production of the three wings.

Srigrarom et al. [31] designed, constructed, and tested 3 wings built with different materials and different camber but with the same shape as observed in Figure 1.26. The wings that were tested are: on the top (1) is a polyethylene terephthalate (PET) cambered thin wing, on the middle (2) an orcon cambered thick wing, and on the bottom (3) an orcon flat wing.

The main objectives of these experiments were to evaluate thrust and lift production of the three wings at different flapping frequencies, and evaluation of the lift production of the three wings for the various phase angles, among others.

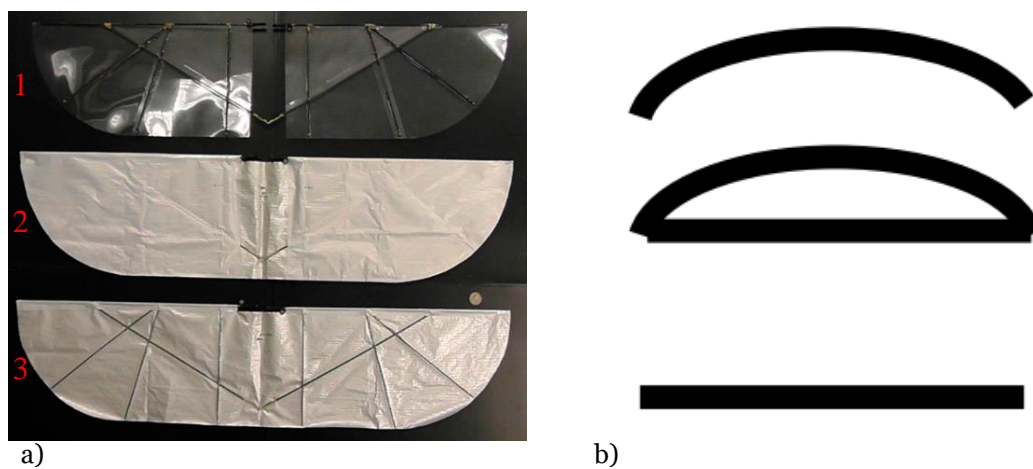


Figure 1.26: a) Platform shape of the three wings used in the experiments, b) Cross-section of the three wings [31].

Results showed that for frequencies below 3 Hz the wing that produced more thrust was wing 1 while for frequencies above 3 Hz, the wing with higher thrust production was wing 2. The wing with the higher peak in lift production was wing 2, even though if wing 3 was the only one that produced lift at medium oscillation speed (2.71 Hz).

1.2.4 Wing manufacturing and materials

Table 1.2: Materials used on wing membrane, structure, and his manufactured technique.

Author	Reference	Wing membrane material	Wing structure material	Manufacturing technique (material)
Billingsley et al.	[6]	Ripstop polyester	Carbon fibre	Glued (tape)
Mueller et al.	[8]	Mylar	Carbon fibre	
Stowers et al.	[9]	Mylar	Carbon fibre	Glued (weldwood contact cement)
Tanaka et al.	[10]	Parylene-C	CFRP	Chemical vapour deposition (CVD)
Hu et al.	[22]	Wood, nylon, latex	Glass fibre	
Pornsirak et al.	[23]	Mylar, paper, silicon	Carbon fibre, parylene-C	Glued (glue), photolithography technology
Ghommem et al.	[24]	Mylar	Carbon fibre	Glued (tape, glue)
Mazaheri et al.	[25][26]	Nylon	Carbon fibre	
Lin et al.	[27]	PVC plastic	Epoxy reinforced carbon fibre	
Mueller et al.	[28]	Mylar	Carbon fibre	
Krashanitsa et al.	[29]	Nylon	Carbon fibre	
Yang et al.	[30]	Mylar	Carbon fibre	Glued (resin adhesive)
Srigrarom et al.	[31]	Orcon, PET	Carbon fibre	
Park et al.	[32]	Polypropylene film	Carbon fibre prepreg	Moulding
Mishra et al.	[33]	Mylar	Carbon fibre	
Altenbuchner et al.	[34]	Ripstop polyester	Carbon fibre	
Hassanalian et al.	[35]	Mylar	Carbon fibre	
Pourtakdoust et al.	[36]	Mylar	Carbon fibre	

Table 1.3: Materials used on wing membrane, structure, and his manufactured technique (continuation).

Author	Reference	Wing membrane material	Wing structure material	Manufacturing technique (material)
Kim et al.	[37]	PVC film	Graphite/epoxy	
Farmand-Ashtiani et al.	[38]	Mylar	Carbon fibre	Glued (gorilla glue)
Jackowski	[39]	Dacron, 1/2 oz polycarbonate coated ripstop polyester	Carbon fibre	Glued (3M VHB adhesive tape)
Floreano et al.	[40]	Mylar	Carbon fibre, balsa-carbon sawdwich	
Hsu et al.	[41]	PET		Glued (double-sized adhesive tape)
Bejgerowski et al.	[42]	Mylar	Carbon fibre	
Nguyen et al.	[43]	Mylar	Carbon fibre	
Chand et al.	[44]	Vinyl tarpaulin	Carbon fibre	
Yang et al.	[45]	Parylene film	Titanium alloy	
Grauer et al.	[46]	Rip-stop polyester	Carbon fibre	Glued (dacron tape)
Harmon et al.	[47]	Rip-stop nylon	Carbon fibre	Glued (dacron tape)
Muniappan et al.	[48]	Mylar	Balsa	
Mahardika et al.	[49]	Polypropylene film	Carbon fibre	
Tsai et al.	[50]	Ethylene		
Moreira	[51]	Mylar	Carbon fibre	Glued
Croon et al.	[52]	Mylar	Balsa	
Bakhtiari et al.	[53]	Mylar	Carbon fibre	

1.3 Objectives

As it can be seen in the literature review, many different studies were made on a different type of wings, where some of them kept the same wing platform and varied the number of spars or its locations; others tried different wings with different shapes and with different materials while others kept the number and location of the spars and the shape of the wing and only changed the membrane material. All these experiments had the same objective of understanding what would change in their results with all the variables, that each of them implemented. So, for this dissertation, the main objective was to determine the influence of wing size, shape, structure in their aerodynamic behavior, and some parameters. To achieve it, several tasks were established:

- Design and build an experimental facility capable of testing the biomimetic drone;
- Develop an electrical system to control the drone work without its original battery;
- Develop a manufacturing process to build the wings;
- Report the obtained results of amplitude, dimensionless amplitude, frequency, reduced frequency, average power, and dimensionless power for each wing and compare their results between the different airflow velocities for every wing;
- Compare performance results between two design processes and among wings with a structural difference.

1.4 Outline

This dissertation is organized into four chapters: Introduction, Experimental study, Results and Discussion, and Conclusion.

In this first chapter, an introduction to the biomimetic was made alongside with the motivation to this study. Besides this, a literature review was presented to describe the studies made in this area, as the objectives listed and explained.

In the second chapter, the description of the experimental study will be presented. The design and manufacturing process of the wings will be explained, as well as the development of the electrical system used to control the drone. Besides this, the experimental rig will be shown, as all components and their characteristics that were used to obtain the results of the tests. Finally, the results acquisition will be explained as well as the post-processing method.

The third chapter of this dissertation is dedicated to the presentation of the results and their respective analysis. This chapter is divided into three subchapters, were in the first one the high-speed camera tests for each wing are presented, with the graphs of the non-dimensionless parameters and with the dimensionless parameters. The second subchapter shows the picoscope tests for the several wings with their graphs as a function of dimensional parameters and

dimensionless parameters. On the last subchapters, the graphs are shown where the comparison of all wings are conducted.

On the fourth and last chapter, the conclusions of the dissertation are presented as well as future work recommendations.

Chapter 2

Experimental Study

2.1 Introduction

This chapter is divided into four sub-chapters. In the first sub-chapter, the wing design will be explained, as well as the structural design, material selection, the manufacturing process, and the electrical system designed to operate the drone. In the second sub-chapter, the experimental rig will be presented, and afterward, the specifications of every component used on the test will be shown individually. In the third sub-chapter, the methodology used in the experiments will be explored. Finally, in the fourth sub-chapter, the measurement techniques will be explained as well as the filter that was used to remove the noise of the electrical system.

2.2 Design and construction

In this dissertation, the design and manufacturing of the wings were one of the most important parts. In this sub-chapter, it will be explained in more detail the design part, the material selection, the structural design, the manufacturing process, and the changes made to the biomimetic drone so that it could work without a battery and instead, use an electrical system.

2.2.1 Design point selection and wing design

One of the objectives of this experiment was to test different wings with different geometries found in nature and use some standard wings, like the rectangular wing, elliptical wing, and triangular wing to act as a base of comparison to the other wings. So, to do this, the wing design was based on the shapes shown in Hassanalian et al. [17]. Knowing this, 8 different wings were initially designed, 4 standard (rectangular, elliptical, and 2 different triangular wings), and 4 based on what is observed in nature (heron, storks, raven and swallow wing).

After some research on which materials should be used it was decided based on Table 1.2 and Table 1.3, to use mylar as the membrane material of the wing, and XT-CF20 as the structural material of the wing. The wing's structural design was chosen to be similar to the original wings from BionicBird by XTIM, i.e., with only one main spar that was glued to the membrane (the manufacturing process will be explained ahead).

Afterward, the BionicBird was dismantled and every part of it was weighted separately. After this, the weight of the drone (W_{T1}) could be obtained by summing the weight of the different parts of the drone. With the help of millimetric paper, the wing area, S_1 , of the original BionicBird wings was estimated and W_{T1}/S_1 was calculated.

In Figure 2.1 it can be observed the design process used to design the rectangular wing, as an example to the other wings, with the only difference being on the S equation that varies with the wing designed at the moment. The root chord (C_r) was considered the same for every wing.

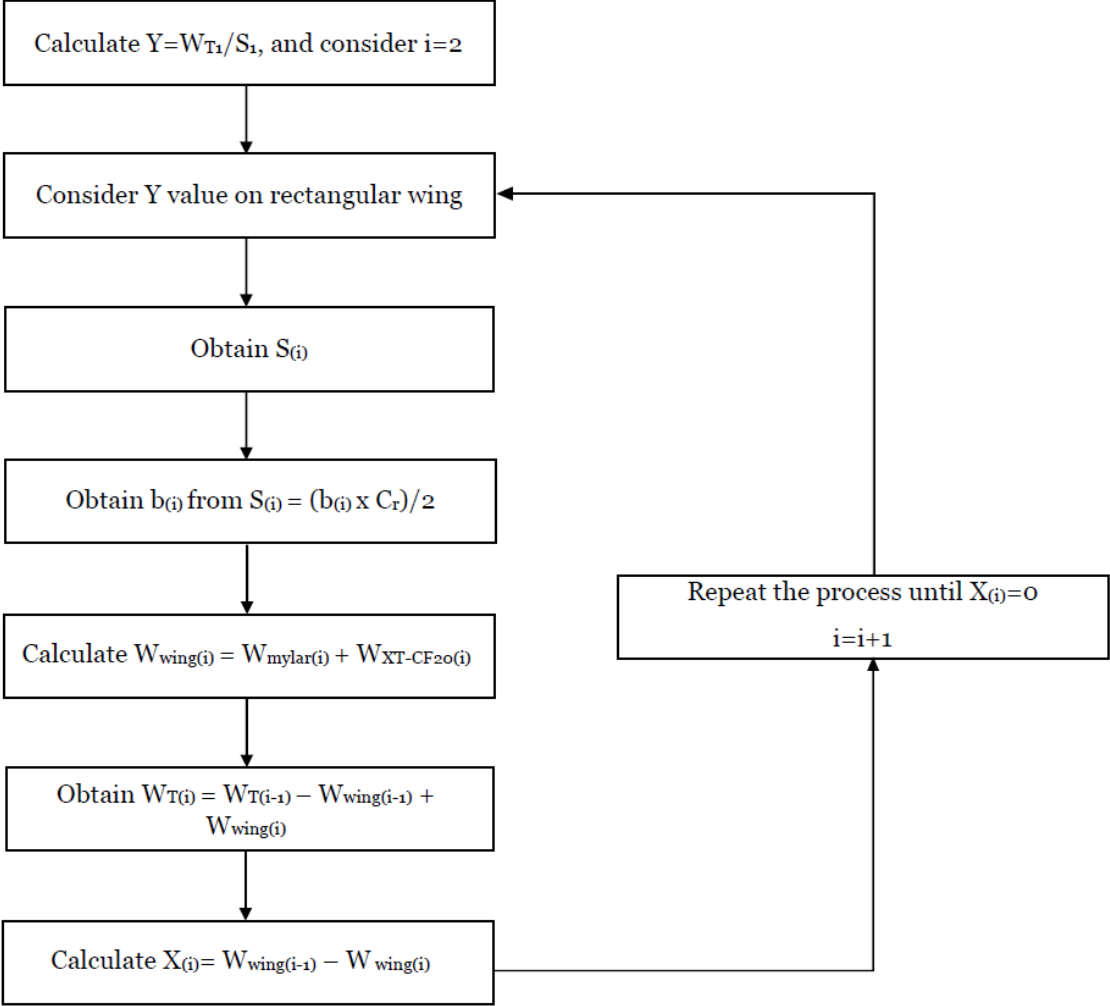
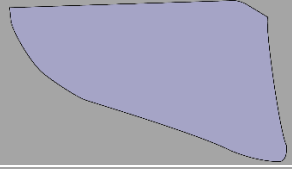

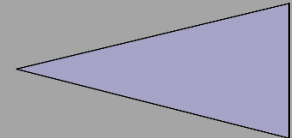
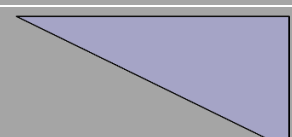
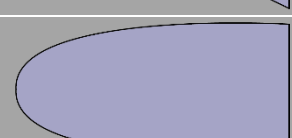
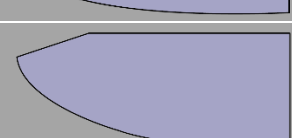


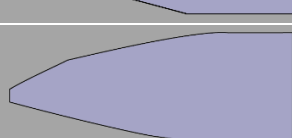


Figure 2.1: Process used to design the rectangular wing.

With the design process shown in Figure 2.1, all the wings designed had the same design point (W/S).

Besides this process another design process was used. In this second method, a Matlab code was developed; this code binarizes the wings images (obtained from Figure 1.14) and with a reference (typically the root chord), it was possible to get the wing area, S , the wingspan, b , and other geometric values. In Table 2.1 the geometrical features of each pair of the designed wings and the BionicBird wings can be observed.

Table 2.1: Features of each pair of projected wings and the BionicBird wings. The designation m represents the wings designed using Matlab.

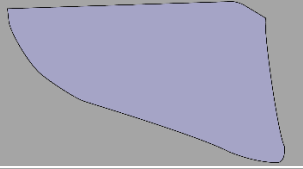


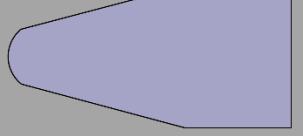
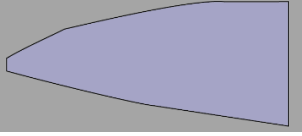
Wing shape	Name	c [cm]	S [cm ²]	W/S [Pa]	b [cm]
	Bionicbird wing	6.5	195.2	5.03	30.0
	Rectangular wing	8.5	225.6	5.03	26.5
	Triangular wing 1	4.3	231.3	5.03	54.4
	Triangular wing 2	4.3	231.1	5.03	54.4
	Elliptical wing	6.7	227.6	5.03	34.1
	Heron wing	7.0	227.0	5.03	32.4
	Heron wing m	6.9	265.1	4.42	38.7
	Stork wing	7.1	215.1	5.03	30.2
	Stork wing m	7.4	294.9	3.88	39.7
	Raven wing	7.3	227.4	5.03	31.3
	Raven wing m	7.0	254.7	4.58	36.5
	Swallow wing	6.1	228.3	5.03	37.6
	Swallow wing m	5.8	221.0	5.18	38.2

In Table 2.1 it can be observed 9 wings with different shapes and 13 wings with different dimensions. Of that 9 wings with different shapes 4 are standard wings, 4 are based on natural flyers and 1 is the original wing of BionicBird. The difference between the wings that were designed using the two methods is because on the first method the equations were obtained mathematically and on the second method, they were completely designed with the Matlab code.

After these two different processes to design the wings shown in Table 2.1, it was decided to reduce the number of wings that would be tested. The wings that are going to be tested experimentally are shown in Table 2.2.

It was decided to remove the triangular wings from the experimental test due to their huge wingspan value. About the wings based on natural flyers, the ones that were selected to be subjected to the experimental tests were the raven wings and the swallow wings, since the birds that they are based on, are smaller and more similar to the BionicBird. Another reason is that the raven and swallow wings are capable of soaring and high speed, and maneuverability, respectively. The heron and stork wings have functions of slow flapping flight and long-distance gliding, respectively.

Table 2.2: Main values of each pair of wings that were subjected to experimental tests.

Wing shape	Name	c [cm]	S [cm ²]	W/S [Pa]	b [cm]
	Bionicbird wing	6.5	195.2	5.03	30.0
	Rectangular wing	8.5	225.6	5.03	26.5
	Elliptical wing	6.7	227.6	5.03	34.1
	Raven wing	7.3	227.4	5.03	31.3
	Raven wing m	7.0	254.7	4.58	36.5
	Swallow wing	6.1	228.3	5.03	37.6
	Swallow wing m	5.8	221.0	5.18	38.2

2.2.2 Structural design

In the previous sub-section, it was mentioned that mylar would be used for the membrane of the wing and XT-CF20 to the spar. All wings were designed on Solidworks 2020. Every spar of each different wing was initially designed the same way, i.e., the part that fits the BionicBird is the same for every wing and their dimensions are 2.1 x 1.9 mm. For the thinner part on the front, it was made a test where 4 rectangular wings were manufactured, from 0.5 x 0.5 mm to 0.8 x 0.8 mm.

In Figure 2.2 the main spar used in the rectangular wing can be observed.



Figure 2.2: Main spar of the rectangular wing.

The results of this test showed that the main spar of the wings with a cross-section of 0.5 x 0.5 mm and 0.6 x 0.6 mm broke when the BionicBird started flapping its wings. The main spar of the wing with 0.7 x 0.7 mm reached plastic deformation but did not break and the main spar of the wing with 0.8 x 0.8 mm did not reach plastic deformation, so it was considered ideal to be used in all wings.

Besides the wings that were already mentioned to be subjected to experimental tests, 2 more wings were developed. These two wings have the same dimensions as rectangular and elliptical wings but with a small difference in the structure of the main spar. The difference consists in the taper of the thinner part of the main spar, i.e., starting with 0.8x0.8 mm and finishing with 0.5x0.5 mm on the tip of the main spar. These two wings were built and tested to observe if the taper makes any difference in the performance of the wing. With this, the number of wings that are going to be tested is 9.

2.2.3 Manufacturing process

After using the Solidworks 2020 to draw the main spars, the manufacturing process started with the help of a Prusa i3 mk3s, where the spars were 3D printed using XT-CF20.

With the spars already printed and with the 5-micron mylar cut, it was time to glue them together. Epoxy resins are often used to glue carbon and glass fibers, so it was decided to use Biresin CR122-3 developed by Sika AG [54].

Each epoxy resin has its own curing time, and for Biresin CR122-3 the curing time was 12 hours at room temperature (from 18 to 35°C) and 8 hours on an oven Carbolite (Figure 2.3) [55] at a temperature between 55-60°C.



Figure 2.3: Oven Carbolite used to cure Biresin CR122-3.

The wings were glued using 2 to 3 stages. The first stage is the same for all the wings and is when the main spar is glued to the mylar. Figure 2.4 shows some wings after Biresin CR122-3 had been applied, with some weights (to keep XT-CF20 in place) and Teflon film so that the wing would not glue the table or the weights. Twelve hours later the wings were subjected to 8 hours inside the oven to finish the first cure of the epoxy resin.



Figure 2.4: Glued wings on the first stage of gluing.

As it can be observed in Figure 2.4 the spar was not glued on the edge of the mylar planform, this happens because on the second stage of gluing the part of the mylar that is above the main spar is going to be bent to give additional resistance to the wing so that it does not break on the thinner part of the XTCF-20.

The second stage is when Biresin CR122-3 is applied on the upper part of the mylar and then it is bent. After this, it is useful to use weights and Teflon film to prevent the wings from sticking to the table and the weights like it can be observed in Figure 2.5. The rectangular wing is the only one that needs 2 stages to be completed since it does not have a curved main spar, so the upper part of the mylar can all be glued at once, while on the wings with a curve main spar, the upper part of the mylar was cut so that mylar could follow the main spar.



Figure 2.5: Glued wings on the second stage of gluing.

The third and final stage is when the last pieces of the mylar film that could not be glued on the second stage are glued. This stage only exists because as we can see in Figure 2.5 when the weights are added to keep the mylar bent it is impossible to bend all the mylar pieces at once. To save time on the manufacturing of the wings, it was decided that the wings that needed the third stage, could do so after 12 hours of room temperature after the second stage was completed, and in that way spare 8 hours to the oven, and only after the two stages they would go to the oven for 8 hours to complete the gluing process.

At the end of the manufacturing process, there were 8 pairs of wings fabricated as can be observed in Figure 2.6.



Figure 2.6: The 8 pairs of wings that were manufactured.

2.2.4 Electrical system

The main objectives of the development of the electrical system were to not limit the tests to the battery duration time and remove any battery aging effects or battery-related problems.

To implement the electrical system, the BionicBird battery had to be removed and 2 wires were welded to the wires that were connected to the battery so that it could be easily connected to a breadboard. The battery was a lithium battery with a voltage of 3.7 V and a current of 55 mAh, so to stay within the BionicBird operational limits, the breadboard had a DC power supply connected. The DC power supply was set to 3.7 V and an electrical current with a maximum of 1000 mA so that the drone would work without any lag. The lag happens when the drop of current is so high that the biomimetic drone is not capable of flapping the wings continuously.

The electrical system used is presented in Figure 2.7.

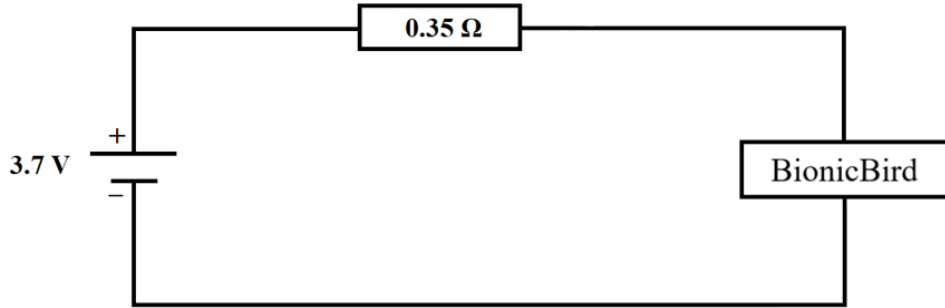


Figure 2.7: Electrical system.

2.3 Experimental Rig

The experimental installation (Figure 2.8) used in this dissertation used a biomimetic drone, a wind tunnel, a wood support, a high-speed camera, a light focus, a picoscope, an electrical system, an anemometer, and a temperature and pressure sensor.

The biomimetic drone (BionicBird by XTIM) (1) was placed in the wood support (2) so in that way, it was unable to move. Both (1) and (2) are placed on the exit of the wind tunnel (3). The DC power supply (4) and the picoscope (5) are connected to the electrical system (6), which consequently is connected to (1). The (5) is also connected to the computer so it can record the values of current and voltage.

At the beginning of each experiment, the tip of the anemometer (7) was placed on the exit of (3) to register the temperature and airflow velocity. The value of atmospheric pressure and the room temperature was obtained with a temperature and pressure sensor (8).

Finally, for proper image acquisition, a light focus (9) and a high-speed camera (10) were required. All the components and their characteristics will be presented in the next subsections.



Figure 2.8: Experimental installation.

2.3.1 BionicBird by XTIM

In this dissertation, a biomimetic drone created by XTIM [56] was used, as mentioned in the last sub-section. The biomimetic drone is Bionic Bird (Figure 2.9a), the model developed before MetaBird. In Figure 2.9b) it can be observed the inside components of the BionicBird. It was designed to fly up to 8 m/s, has a wingspan of 33 cm, weighs 9.5 g, and can be operated within a range of 150 m with the BionicBird control app.



Figure 2.9: a) BionicBird by XTIM. b) Components of BionicBird.

2.3.2 Wind tunnel

To evaluate the effect of the airflow on the BionicBird wings' performance, a wind tunnel (Figure 2.10a) was used on three different velocities (one, two, and four meters per second). To control the airflow velocities, a controller was used (Figure 2.10b), which operates between a frequency of 25 up to 45 Hz, and the wind tunnel guillotine (Figure 2.10c), which can be changed between 0 and 15 cm. With these two ways to control the airflow velocity and with a wind tunnel exit section of 300 x 402 mm, the airflow velocity can reach values up to 6 m/s.

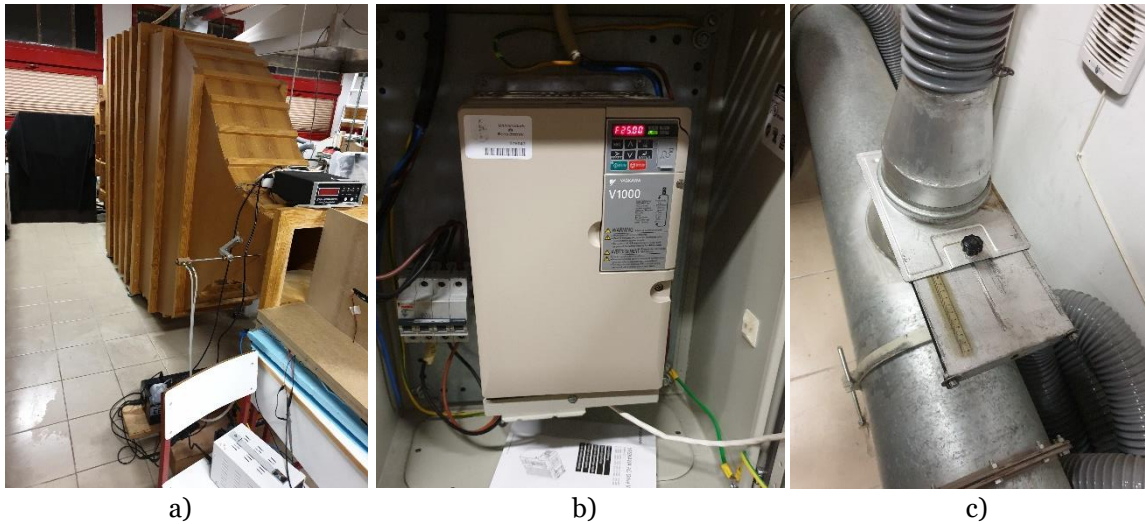


Figure 2.10: a) Wind tunnel; b) Wind tunnel frequency controller; c) Wind tunnel guillotine.

2.3.3 Wood support

To maintain BionicBird in the same position on the front of the wind tunnel, a wood support was manufactured (Figure 2.11b). This support was positioned on the wind tunnel output and was not centered with the section output because the main objective was to evaluate the reaction of the right-wing to the airflow. So, to that happen it had to be placed 9 cm to the left side (Figure 2.11a) of the wind tunnel output.

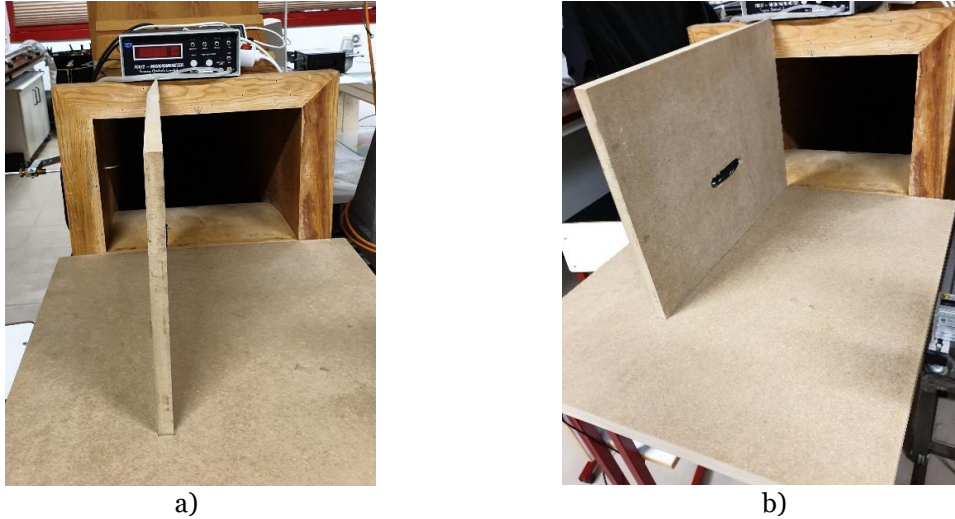


Figure 2.11: a) Back view of the wood support; b) Lateral view of the wood support.

2.3.4 High-speed camera

To ensure that the quality of the images during the tests was adequate, several tests were performed before starting the final tests. This was made using a Photron FASTCAM mini UX50 with a 1.3-megapixel resolution with a frame rate of up to 2000 frames per second (fps). The lens used is a Canon EF-S 18-55 mm. Both lens and high-speed camera are presented in Figure 2.12. For the high-speed camera tests, the frame rate used was 500 fps with a resolution of 1280x1024.



Figure 2.12: Photron FASTCAM mini UX50 with Canon EF-S 18-55mm lens.

2.3.5 Illumination

To improve the image acquisition, a powerful light focus was used. The light focus is Kaiser video light 6 (Figure 2.13), which has a halogen lamp of 1000 W and a safety glass diffuser [57].



Figure 2.13: Kaiser video light 6 utilized in the tests [57].

2.3.6 PicoScope

The data acquisition was essential in the experimental study to estimate power consumption. For this process, a PicoScope 2204A (Figure 2.14) was used. It has 2 oscilloscope channels with a bandwidth of 10 MHz, an arbitrary waveform generator (AWG) with a bandwidth of 100 kHz and a vertical resolution of 8 bits up to 12 bits [58].

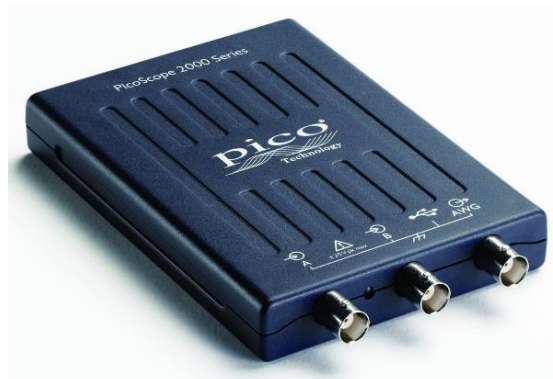


Figure 2.14: PicoScope 2204A used in the tests [58].

2.3.7 Electrical System

As it was described in a previous subsection the electrical system was an important part of this dissertation, so in that way, Bionic Bird would work without the restriction of the battery. The main reason for the use of the electrical system was that with the resistance placed on the breadboard, and using the PicoScope, it was possible to measure the electric current of the system.

2.3.8 DC power supply

A PeakTech DC Power Supply 6070 presented in Figure 2.15 was used, with a voltage set to 3.7 V and a current value variable between 0 and 1200 mA.



Figure 2.15: PeakTech DC Power Supply 6070 used in the tests.

2.3.9 Anemometer

During the experiments, the airflow velocities and temperatures on the wind tunnel exit were measured at the start of each test. For this, the anemometer of Figure 2.16 was used.



Figure 2.16: Anemometer Airflow TA410 used in the tests.

2.3.10 Pressure and temperature sensor

Before every experiment, the room temperature and atmospheric pressure were measured. For this, a sensor of pressure and temperature was used and is shown in Figure 2.17.



Figure 2.17: Pressure and temperature sensor used in the experiments.

With this measurements, viscosity and air density were obtained using Sutherland's law (equation 2.1) and perfect gas law (equation 2.2), respectively.

$$\mu = \mu_0 \left(\frac{T}{T_0} \right)^{3/2} \frac{T_0 + S_T}{T + S_T} \quad (2.1)$$

$$\rho = \frac{P}{RT} \quad (2.2)$$

2.4 Results Acquisition

To guarantee the validity of the results, and that they all were made with similar conditions, a methodology was created and followed. The experiment can be divided into two main tests:

- High-speed camera tests - the main objective was to record the BionicBird from behind for each different wing so that it could be possible to get the amplitude and the period of the flapping cycle;
- Picoscope tests - the objective was to get the electric current and voltage values for each different wing tested.

2.4.1 Methodology

High-speed camera tests

- Adjust airflow velocity of the wind tunnel;
- Register environment temperature, atmospheric pressure, and airflow temperature;
- Turn on DC power supply;
- Turn on high-speed camera;
- Turn on illumination;

- Take a snapshot with the measurement reference;
- Turn on Bionic bird and choose the desired throttle;
- Start filming;
- Turn off Bionic bird;
- Save video record;
- Repeat from the beginning.

Picoscope tests

- Adjust airflow velocity of the wind tunnel;
- Register environment temperature, atmospheric pressure, and airflow temperature;
- Turn on DC power supply;
- Open picoscope 2024A software in the computer;
- Turn on Bionic bird and choose the desired throttle;
- Register electric current intensity and voltage;
- Turn off Bionic bird;
- Save data;
- Repeat from the beginning.

2.5 Post-processing

In this last sub-chapter, the measurement techniques used and the data treatment (frequency, amplitude, voltage, and electric current measurements, among others) will be explained as well as the error of measurements used and its propagation.

2.5.1 Amplitude and frequency determination

For the amplitude determination, the images taken with the high-speed camera were used. To ensure better measurements, two amplitudes (A_{up} , A_{down}) were calculated alongside with two thetas (θ_{up} , θ_{down}) and two horizontal distances (d_{up} , d_{down}), as it is shown in Figure 2.18.

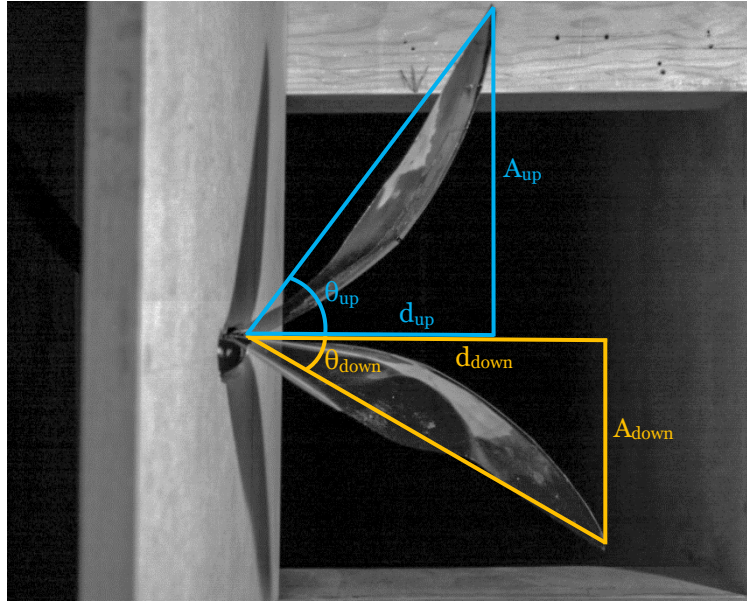


Figure 2.18: Amplitude, theta, and horizontal distance determination.

Besides this, to transform the amplitude measurement from pixels to cm, a reference (Figure 2.19) was needed, so in that way, it was possible to get the size of the pixel and with that, calculate the corresponding amplitude. Since every wing had four tests for each airflow velocity, a reference would be taken to be sure of the validity of the results. Although, for every test conducted, 5 amplitude measurements were taken to ensure the precision of amplitude calculation.



Figure 2.19: Reference used in $U = 0$ m/s for BionicBird original wing.

After this to get both A and θ , equations (2.3) and (2.4) were used, respectively.

$$A = A_{up} + A_{down} \quad (2.3)$$

$$\theta = \theta_{up} + \theta_{down} \quad (2.4)$$

For the frequency determination, the period (p) of the flapping cycle of the wing was obtained, and then equation (2.5) was used.

$$f = \frac{1}{p} \quad (2.5)$$

For each test conducted, and just like the amplitude, 5 periods of the flapping cycle of the wing were measured, and consequently, 5 frequencies were obtained.

2.5.2 Data filtering

The function of the picoscope 2024A was to measure the values of electric current (I) and voltage (V) of the electrical system. Thus, one of the channels of the picoscope was connected to the resistance (Figure 2.20), so the value of I could be calculated.

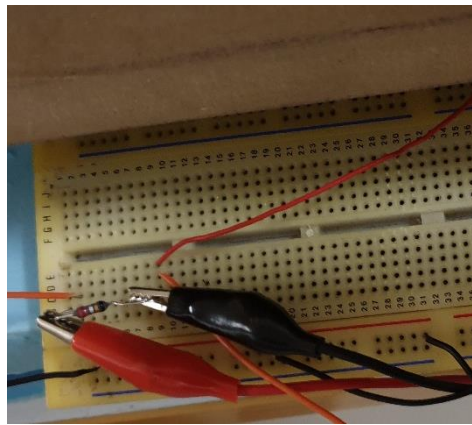


Figure 2.20: Connection of the cable of the picoscope to the resistance.

After obtaining the voltage, the electrical current was calculated using Ohm's law, defined as

$$I = \frac{V}{r} \quad (2.6)$$

where I is the electric current, r the resistance, and V the voltage.

The other channel of the picoscope was connected to the BionicBird, so in that way, it is possible to register the values of the voltage on the drone.

After measuring the electrical data (V and I), a filter was deemed necessary due to high levels of electrical noise. So, to filter the data, two filters were considered, to remove the noise. The first filter is based on the one developed by Bousson et al. [59], but only performed well for the data obtained at a throttle of 100%. The second filter was based on the moving-average filter (1D-filter) that was already implemented in the Matlab program [60] for all obtained throttles.

2.5.3 Power consumption

To get the power consumption of the BionicBird the value of electric current and voltage were multiplied after being filtered by the aforementioned moving-average filter. That filter code was inserted in the middle of the power consumption code, so it could filter the data (V and I) and automatically show the power consumption graph. In Figure 2.21 a graph of V of the Swallow wing with the original data (presented in blue) and the filtered data (orange) at a throttle of 25% and an airflow velocity of 4m/s.

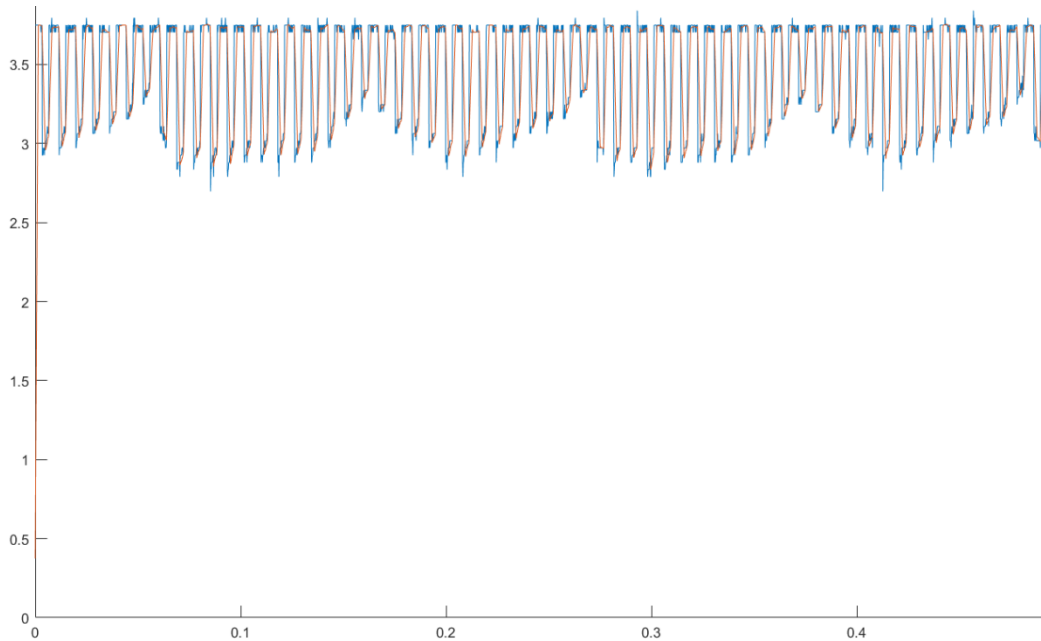


Figure 2.21: Graph of voltage for the Swallow wing for an airflow velocity of 4 m/s at a throttle of 25% with the original data at blue and the filtered that at orange

After this, a way to present the average power into a dimensionless power was considered. Thus, the reference power in equation (2.7) was chosen.

$$P^* = \frac{1}{2} \rho c^3 f^3 S \quad (2.7)$$

where ρ is the air density, c the mean chord, f the motion frequency, and S the wingspan.

2.5.4 Error propagation estimation

Every instrument has a measurement error, and with that, every data obtained should be subjected to an error propagation analysis.

In equation (2.8) the error associated with the air density calculation is presented, where R is the ideal gas constant, T , is the room temperature, P the atmospheric pressure, δT the error of the temperature sensor, and δP the error of the air pressure sensor.

$$\delta\rho = \left| \frac{1}{RT} \right| |\delta P| + \left| -\frac{P}{RT} \right| |\delta T| \quad (2.8)$$

The error associated with the dynamic viscosity of the fluid (air) is presented in equation (2.9), μ_o is the dynamic viscosity at temperature T_o which is the reference temperature according to Sutherland's law. T is the room temperature, S_T the Sutherland temperature, and δT the error of the temperature sensor.

$$\delta\mu = \left| \mu_o \left[\frac{\sqrt{T}}{T_o^{3/2}} \left(\frac{T_o + S_T}{T + S_T} \right) - \left(\frac{T}{T_o} \right)^{3/2} \left(\frac{T_o + S_T}{(T + S_T)^2} \right) \right] \right| |\delta T| \quad (2.9)$$

In equation (2.10) the error associated with the Reynolds number is presented, and it depends on ρ , the air density, c the mean chord, U_∞ the airflow velocity, μ the dynamic viscosity, δU_∞ the error of the anemometer, δc the error associated to the ruler, $\delta\mu$ error of the dynamic viscosity of the fluid and $\delta\rho$ the error of the air density.

$$\delta Re = \left| \frac{U_\infty c}{\mu} \right| |\delta\rho| + \left| \frac{\rho c}{\mu} \right| |\delta U_\infty| + \left| \frac{\rho U_\infty}{\mu} \right| |\delta c| + \left| \frac{\rho U_\infty c}{\mu^2} \right| |\delta\mu| \quad (2.10)$$

The error associated with the motion amplitude is presented on equation (2.11), with A being the stroke amplitude, c the mean chord, δA the error of the amplitude and δc the error associated with the ruler.

$$\delta h = \left| -\frac{A/2}{c^2} \right| |\delta c| + \left| \frac{1}{c} \right| |\delta A| \quad (2.11)$$

In equation (2.12) it can be seen the error of the reduced frequency, where f is the motion frequency, U_∞ the airflow velocity, c the mean chord, δc the error associated with the ruler, δf the error of the high-speed camera, and δU_∞ the error of the anemometer.

$$\delta k = \left| \frac{2\pi f}{U_\infty} \right| |\delta c| + \left| \frac{2\pi c}{U_\infty} \right| |\delta f| + \left| -\frac{2\pi f c}{U_\infty^2} \right| |\delta U_\infty| \quad (2.12)$$

The error associated with the Strouhal number is presented in equation (2.13), with A being the stroke amplitude, U_∞ the airflow velocity, f is the motion frequency, δf the error of the high-speed camera, δA the error of the amplitude, and δU_∞ the error of the anemometer.

$$\delta St = \left| \frac{A}{U_\infty} \right| |\delta f| + \left| \frac{f}{U_\infty} \right| |\delta A| + \left| -\frac{f A}{U_\infty^2} \right| |\delta U_\infty| \quad (2.13)$$

In equation (2.14) the error of the stroke angle is presented, with A being the stroke amplitude, d is the horizontal value for the value of A , δA the error of the amplitude, and δd the error of the horizontal distance.

$$\delta\theta = \left| \frac{1}{d(1 + (A/d)^2)} \right| |\delta A| + \left| \frac{1}{d^2(1 + (A/d)^2)} \right| |\delta d| \quad (2.14)$$

Chapter 3

Results and Discussion

3.1 Introduction

In this chapter, the results of the high-speed camera and picoscope tests will be presented and discussed individually, for the four airflow velocities (0, 1, 2, and 4 m/s) and throttle positions of 25, 50, 75, and 100%. As the value of frequency always increases with the increase of throttle in every graph, the first point of every graph will present the 25% throttle value, the second point the 50% throttle, and so on.

The wings that are going to be tested are the:

- BionicBird original wing (presented in table 2.2);
- Rectangular wing (presented in table 2.2);
- Rectangular wing 2 (mentioned in a previous chapter, has the same measures as a rectangular wing but with a tapering in the thinner part of the main spar);
- Elliptical wing (presented in table 2.2);
- Elliptical wing 2 (referred in a previous chapter, has the same measures as an elliptical wing but a tapering in the thinner part of the main spar);
- Raven wing (presented in table 2.2, developed with geometrical equations);
- Raven wing m (presented in table 2.2, developed with Matlab code);
- Swallow wing (presented in table 2.2, developed with geometrical equations);
- Swallow wing m (presented in table 2.2, developed with Matlab code).

Afterward, the results will be compared between the tested wings to identify the ones that had better power consumption, for each case.

3.2 High-speed camera tests

As mentioned before, the high-speed camera tests were performed to obtain the values of amplitude, frequency, and wingtip opening angle relative to the wing root (θ) for each wing. Besides this, the dimensionless amplitude and reduced frequency were also calculated for each wing. Regarding θ graphs, they are presented in Appendix A.

In Figure 3.1 the upward and downward movement of the Swallow wing for an airflow velocity of 1m/s and a throttle of 50% is shown, as an example of how the upward and downward motions have some differences, since the wings have a higher bending on the upper movement.

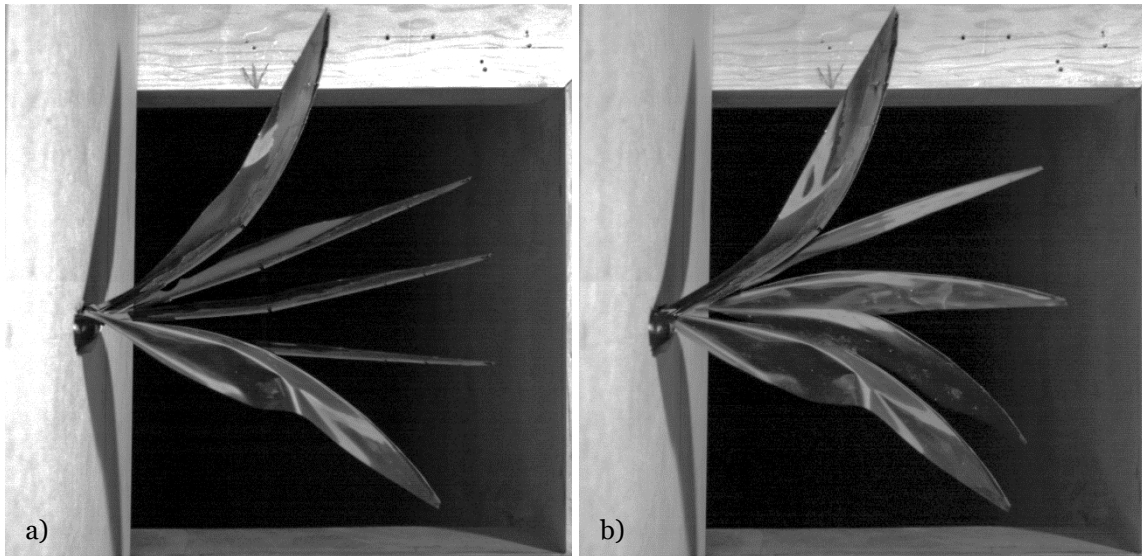


Figure 3.1: a) Downward motion of the Swallow wing for an airflow velocity of 1 m/s at a throttle of 50%.
 b) Upward motion of the Swallow wing at a throttle of 50% for an airflow velocity of 1 m/s.

3.2.1 BionicBird original wing

In Figure 3.2 the graph of Amplitude vs Frequency is shown at multiple airflow velocities (0, 1, 2, and 4 m/s) and the graph of Dimensionless Amplitude vs Reduced Frequency at different Reynolds numbers for the BionicBird original wing. For an airflow velocity of 0 m/s, Re and k were not considered as the latter is mathematically not defined, and because of that, values of h for that airflow velocity for this type of graph and each of the 9 wings will be presented in Appendix B.

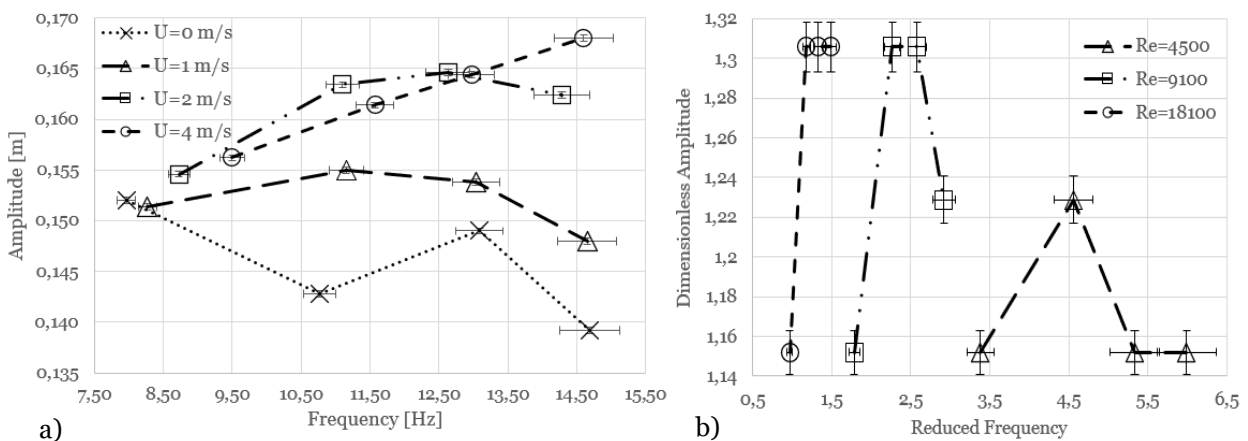


Figure 3.2: a) Amplitude vs Frequency at various airflow velocities of BionicBird original wing. b) Dimensionless Amplitude vs Reduced Frequency at different values of Reynolds for BionicBird original wing.

As it is shown in Figure 3.2 a), amplitude values seem to increase with the increase of the airflow velocity. For an airflow velocity of 0 m/s, the behavior is oscillatory being the higher amplitude located at a throttle of 25%. For 1 and 2 m/s, its behavior seems like a parabolic curve and their

maximum amplitude is for a throttle of 50% and 75% respectively. Finally, for an airflow velocity of 4 m/s the higher the throttle is, the higher is the amplitude, which shows a linear dependency on the throttle.

In Figure 3.2 b), it is seen that with the increase of the Reynolds number, the reduced frequency decreases, and the dimensionless amplitude increases. For a Reynolds number of 4500, the higher dimensionless amplitude is at a throttle of 50%. Even though if for the other throttles it seems stable, for a Reynolds number of 9100 the higher dimensionless amplitude are for throttles of 50 and 75%. For a Reynolds number of 18100 it remains constant after the 50% reaching its higher dimensionless amplitude.

3.2.2 Rectangular wing & Rectangular wing 2

Figure 3.3 shows the rectangular wing and rectangular wing 2 shape. Although similar, they differ on the structure of the main spar. In Figure 3.4, the graph of Amplitude vs Frequency and Dimensionless Amplitude vs Reduced Frequency is shown at different airflow velocities, and various Reynolds numbers for both wings separately.



Figure 3.3: Rectangular wings and Rectangular wings 2 shape.

As it is presented in Figure 3.4 a) the amplitude behavior of the rectangular wing for an airflow velocity of 0 m/s seems oscillatory with its maximum being at throttle of 50%. For 1 m/s it is almost constant with a maximum value at a throttle of 75%, while for 2 and 4 m/s it increases monotonically, with the exception on the 50% of throttle for 2 m/s, with its higher values being on the throttle of 100%. On the other hand, in Figure 3.4 c) the amplitude seems to behave in a similar way to an airflow velocity of 0 and 2 m/s with its maximum being for a throttle of 50%, while for 1 and 4 m/s the amplitude behaves in the opposite way since for 1 m/s its value decreases, and for 4 m/s it increases and so, their biggest values are for a throttle of 25 and 100% respectively.

It can be observed in Figure 3.4 b) and in Figure 3.4 d) that the value of reduced frequency decreases for higher values of the Reynolds number. In Figure 3.4 b) it seems that for the lower Reynolds number (7000) the dimensionless amplitude is constant, while for the other values (14000 and 28200) its value is higher to a throttle of 100%. On the other hand, in Figure 3.4 d) for a Reynolds number of 27700 and 6900 their maximum value occurs at a throttle value of 100% and 50% respectively, though for the other Reynolds number (13900) it is constant.

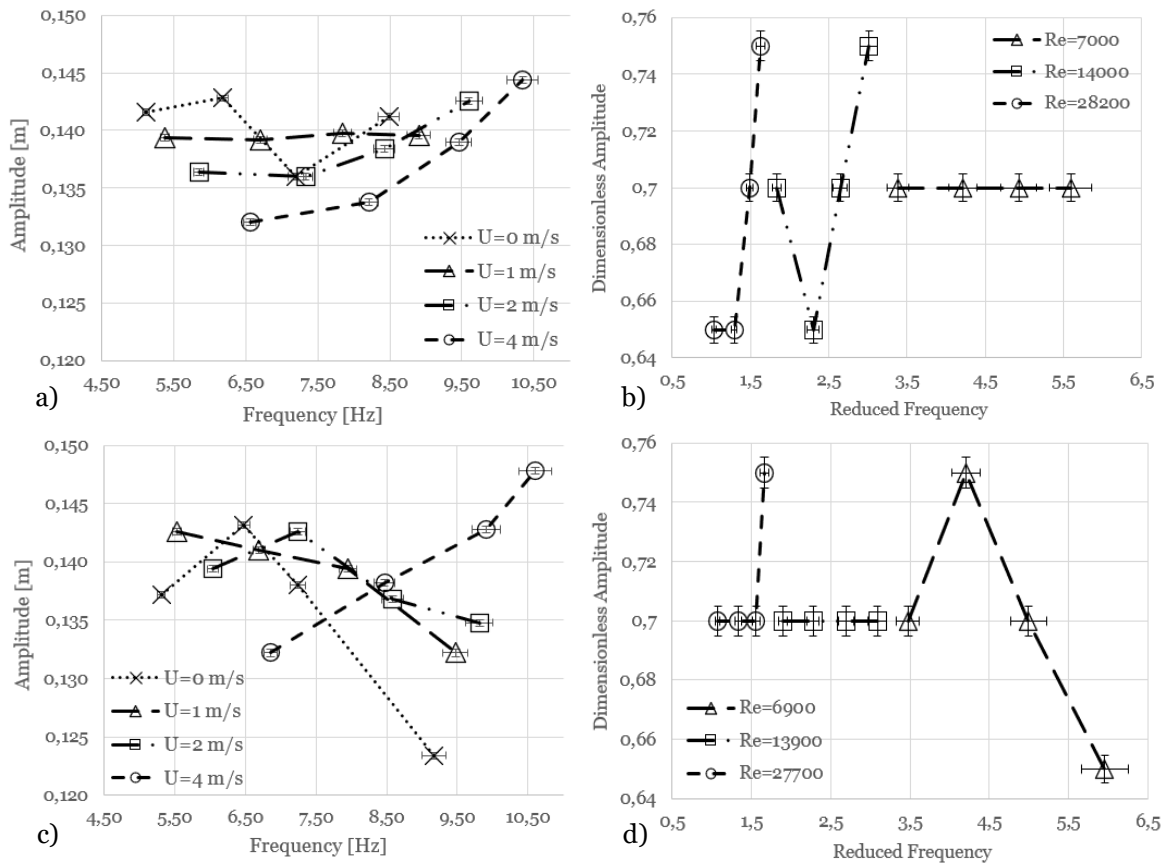


Figure 3.4: a) and c): Amplitude vs Frequency at different airflow velocities of Rectangular wing and Rectangular wing 2, respectively. b) and d): Dimensionless Amplitude vs Reduced Frequency at various values of Reynolds for Rectangular wing Rectangular wing 2, respectively

Besides the latest observations, both wings share similar values of frequency/reduced frequency and amplitude/dimensionless amplitude even though if the range of the amplitude values of the rectangular wing 2 is slightly bigger than the one from the rectangular wing, i.e., Rectangular wing presented the higher and lower values of amplitude.

3.2.3 Elliptical wing & Elliptical wing 2

In Figure 3.5 the shape of wings elliptical and elliptical 2 are presented, since their only difference is on their main spar. While in Figure 3.6 the graphs of Amplitude vs Frequency and Dimensionless Amplitude vs Reduced Frequency will be shown for different airflow velocities and Reynolds numbers for both wings, respectively. It should be referred that for the elliptical wing and for the higher value of airflow velocity and Reynolds number the last two tests (for a throttle of 75 and 100%) should not be considered, since these tests were conducted with a new wing, since, unfortunately, the wing being used, broke and with that, a new one had to be manufactured.



Figure 3.5: Shape of Elliptical wing and Elliptical wing 2.

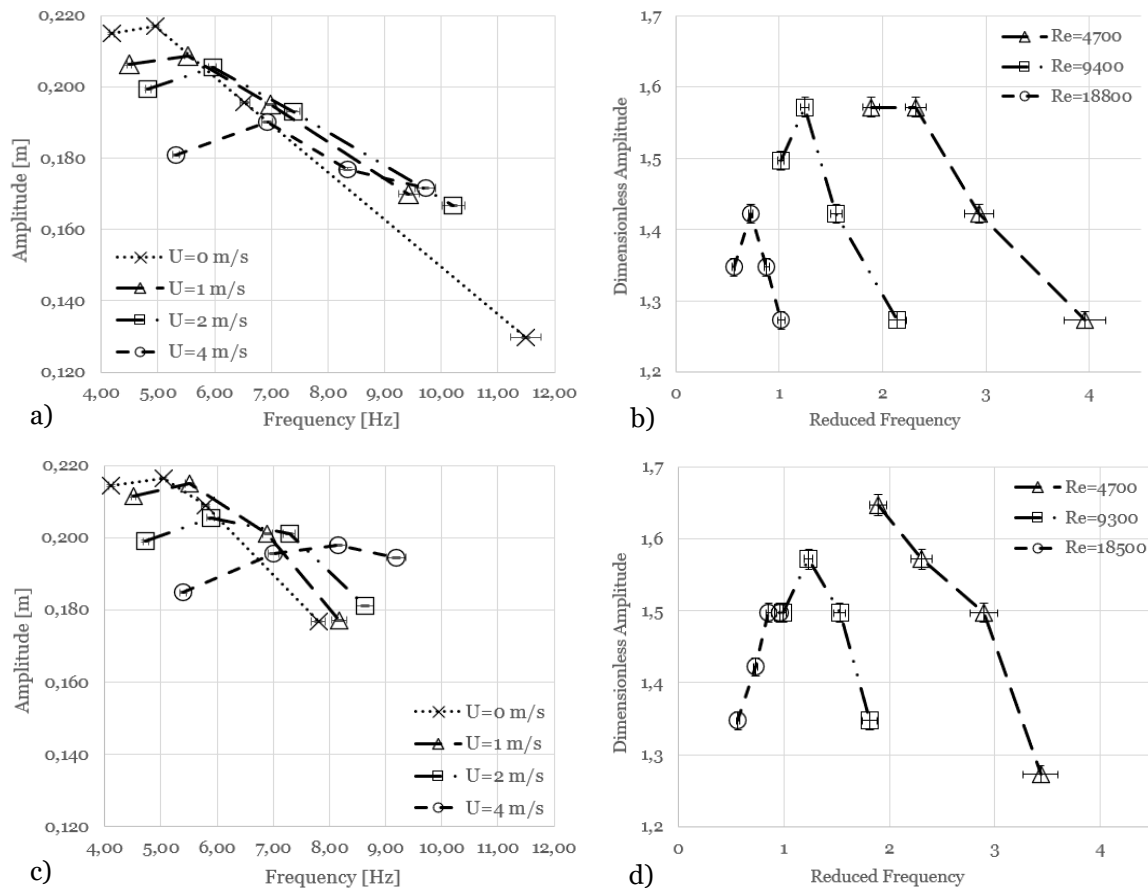


Figure 3.6: a) and c): Amplitude vs Frequency at various airflow velocities of Elliptical wing and Elliptical wing 2, respectively. b) and d): Dimensionless Amplitude vs Reduced Frequency at different values of Reynolds for Elliptical wing and Elliptical wing 2, respectively.

In the graph of Figure 3.6 a) it seems that all the airflow velocities present a similar outline until a throttle of 50%. Also, in Figure 3.6 c) the higher amplitude occurs for a throttle of 50% and an airflow velocity of 0, 1, and 2 m/s, with the airflow velocity of 4 m/s being the only exception with its maximum value at a throttle of 75%.

The values of reduced frequency decrease with the increase of the Reynolds number as is shown in Figure 3.6 b) and Figure 3.6 d). Besides this, in Figure 3.6 b), for the lower Reynolds numbers (4700) the behavior of the dimensionless amplitude gives the idea to be different from the other Reynolds numbers (9400 and 18800), since its constant until a throttle of 50% and also has its higher value of dimensionless amplitude on those throttles positions, while on the other Reynolds numbers they are achieved only at a throttle of 50%. In Figure 3.6 d), the higher value of the

dimensionless amplitude is presented at a throttle of 25, 50, and 75% for Reynolds number of 4700, 9300, and 18500, with a difference noted at the higher Reynolds number since the value of dimensionless amplitude remains constant after a throttle of 75%.

When a comparison of the results is performed on both wings, it can be noticed that the elliptical wing seems to have a bigger range of amplitude and frequency values than the elliptical wing 2, while elliptical wing 2 have a slightly higher range of dimensionless amplitudes, i.e., the non-tapered wing presented a higher range of amplitude values.

3.2.4 Raven wing & Raven wing m

It is presented, in Figure 3.7 the shape of both wings (raven and raven m), and in Figure 3.8 the graphs of Amplitude vs Frequency and Dimensionless Amplitude vs Reduced Frequency at different airflow velocities and Reynolds numbers.



Figure 3.7: a) Shape of Raven wing m. b) Shape of Raven wing.

The amplitude in Figure 3.8 a) and Figure 3.8 c) seem to present its higher value for a throttle of 50% for all airflow velocities with the exception being in Figure 3.8 a) for an airflow velocity of 0 and 4 m/s where the higher value occurs at a throttle of 75%.

As it is shown in Figure 3.8 b) and Figure 3.8 d), the dimensionless amplitude has its maximum at a throttle of 50% for the lower and mid-Reynolds number (5100 and 10100) and the lower and higher Reynolds numbers (4900 and 19800) respectively. For a Reynolds number of 20300 (Figure 3.8 b) and 9900 it increases monotonically, and so their biggest value is at a throttle of 100%. Besides this, the achievable reduced frequency reduces with the increase of the Reynolds number for Figure 3.8 b) and Figure 3.8 d).

Despite this, the range of amplitude, frequency, and dimensionless amplitude of the raven wing m seems bigger than the one presented by the raven wing, although they present a similar interval of reduced frequency.

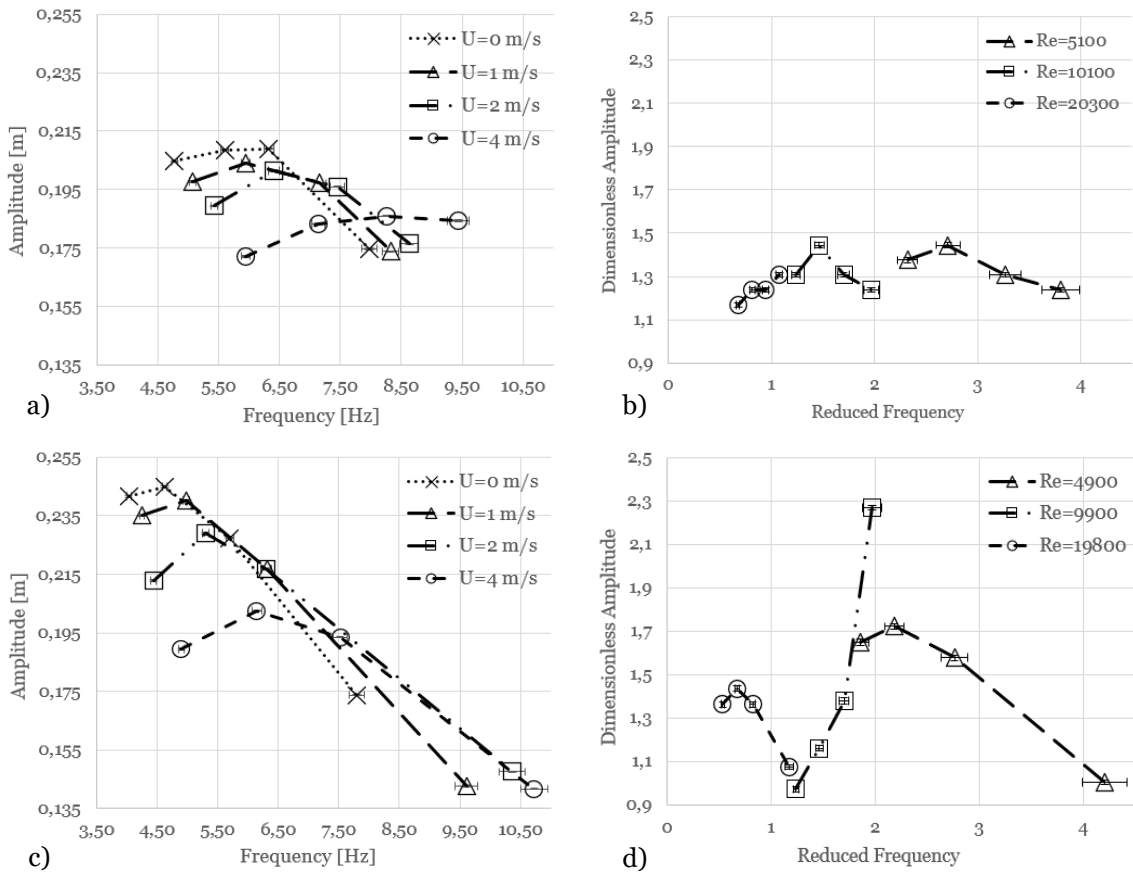


Figure 3.8: a) and c): Amplitude vs Frequency at various airflow velocities of Raven wing and Raven wing m, respectively. b) and d): Dimensionless Amplitude vs Reduced Frequency at different values of Reynolds for Raven wing and Raven wing m.

3.2.5 Swallow wing & Swallow wing m

It can be observed in Figure 3.9 the shape of the Swallow wing and Swallow wing m, while in Figure 3.10, the Amplitude vs Frequency and the Dimensionless Amplitude vs Reduced Frequency graphs for different airflow velocities and Reynolds numbers is shown.



Figure 3.9: a) Swallow wing m shape. b) Swallow wings shape.

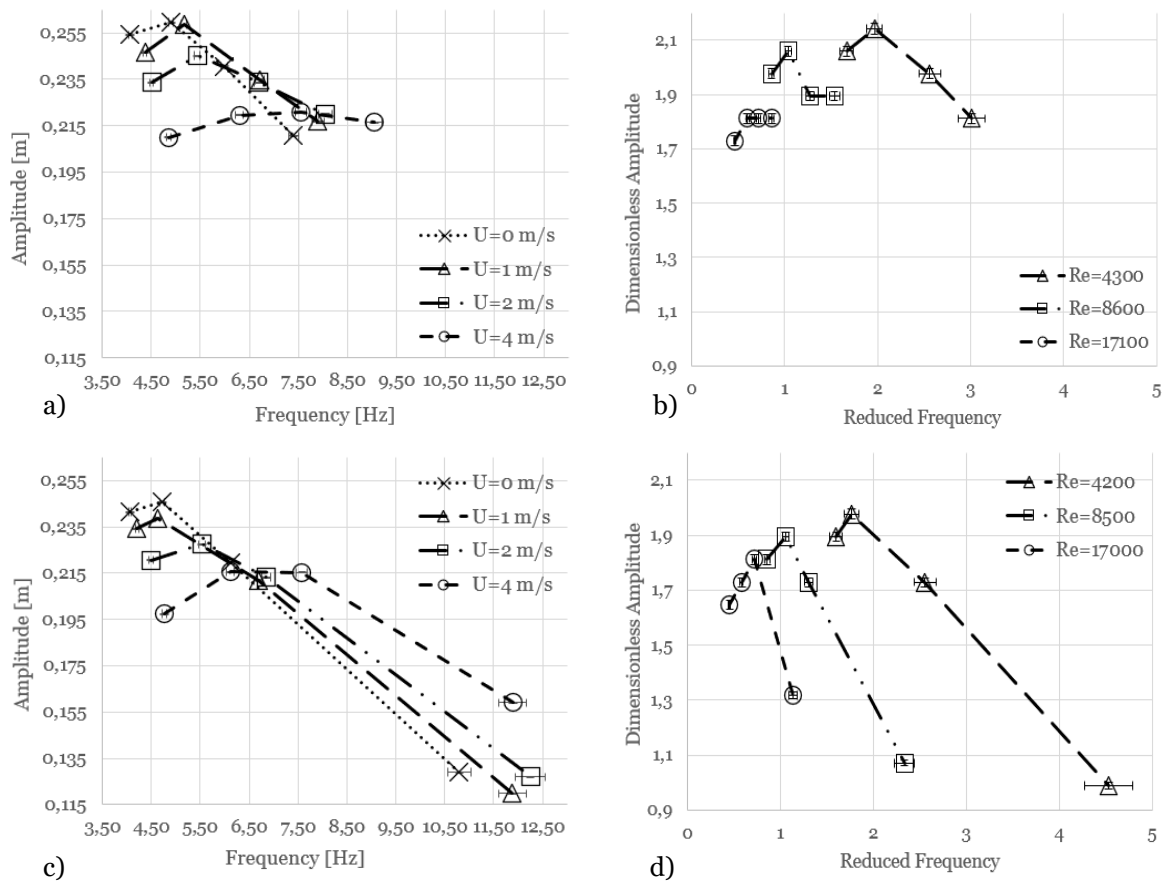


Figure 3.10: a) and c): Amplitude vs Frequency at various airflow velocities of Swallow wing and Swallow wing m, respectively. b) and d): Dimensionless Amplitude vs Reduced Frequency at different values of Reynolds for Swallow wing and Swallow wing m, respectively.

As it is presented in both Figure 3.10 a) and Figure 3.10 c), the amplitude seems to be maximized, for almost every studied case, at a throttle of 50% despite the airflow velocity, with the exception being at 4 m/s, where for Figure 3.10 a), its higher value is for a throttle of 75% and in Figure 3.10 c), it is seen somewhere between 50 and 75% of throttle position.

In the graphs presented in Figure 3.10 b) and Figure 3.10 d), reduced frequency shows a decrease at higher Reynolds numbers, although the higher value of the dimensionless amplitude is shown at 50% throttle for most cases. For a Reynolds number of 17000, in Figure 3.10 d) the dimensionless amplitude reaches its maximum at 75%, and in Figure 3.10 b) after a throttle of 50%, the dimensionless amplitude remains constant.

It is also important to mention that the swallow wing m presents a wider a range when compared to every case studied in this subsection. It should be noted that the range regarding The Swallow wing m is bigger for every case studied in this section when compared to the Swallow wing, even if the higher values are presented by Swallow wing.

3.3 Picoscope tests

The main objective of the picoscope tests was to evaluate the average power used by the drone with different types of wings. So, graphs for each wing of average power as a function of frequency and dimensionless power as a function of Strouhal number were obtained. It was decided to present only some of the graphs since some of them show similar tendencies, although the remain graphs will be presented in Appendix C. Besides that, a graph of Average power vs throttle was created for Bionibird's original wing so a reference of the normal functioning of the drone would be obtained.

3.3.1 BionicBird original wing

In this subsection, two figures will be shown, wherein Figure 3.11, an Average power vs Throttle graph for an airflow velocity of 0 m/s is presented, while in Figure 3.12, graphs of the Average Power vs Frequency and Dimensionless Power vs Strouhal number at different airflow velocities and Reynolds numbers, respectively.

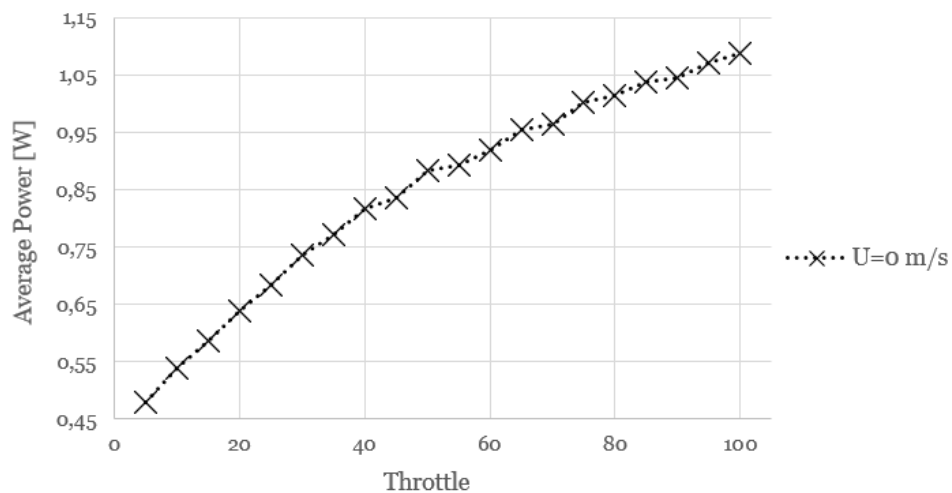


Figure 3.11: Average Power vs Throttle at an airflow velocity of 0 m/s of BionicBird original wing.

The average power seems to increase with the throttle for an airflow velocity of 0 m/s, as shown in Figure 3.11.

For an airflow velocity of 0 m/s, the Reynolds and Strouhal numbers were not considered, so, the values of dimensionless power for that airflow velocity and for each of the other 9 wings are presented in Appendix D.

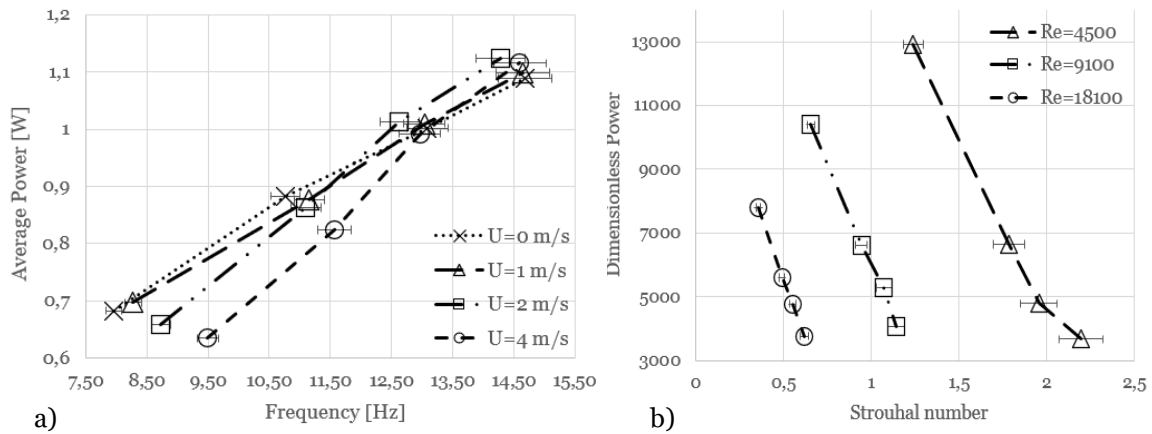


Figure 3.12: a) Average Power vs Frequency of the BionicBird original wing for different airflow velocities. b) Dimensionless Power vs Strouhal number of the BionicBird original wing at various Reynolds numbers.

Concerning average power, in Figure 3.12 a) it seems that when increasing the throttle position, higher is the power consumption regardless the airflow velocity. Important to notice that for lower throttle positions (25 and 50%) the average power decreases with the increase of the airflow velocity.

Regarding Figure 3.12 b), the dimensionless power seems to be smaller at higher throttle positions and decreases with the increase of the Reynolds number. The same is verified with the Strouhal number since higher Strouhal numbers (higher throttle positions) reduce the dimensionless power.

3.3.2 Elliptical wing 2

Figure 3.13 presents graphs of Average power vs Frequency and Dimensionless Power vs Strouhal number for different airflow velocities and Reynolds numbers respectively. These graphs concern the Elliptical wing 2, even though these graphs are very similar to the ones observed in the graphs of Rectangular wing, Rectangular wing 2, Raven wing and Swallow wing.

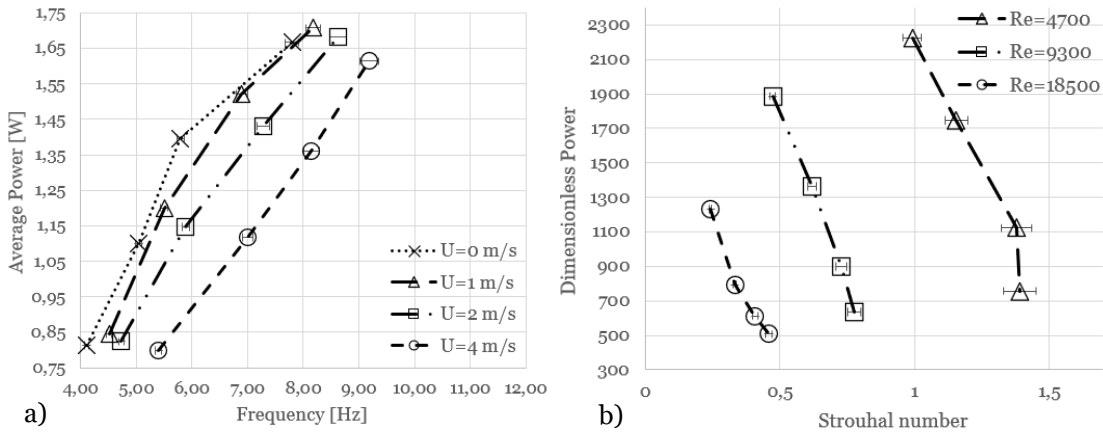


Figure 3.13: a) Average Power vs Frequency for different airflow velocities of the Elliptical wing 2. b) Dimensionless Power vs Strouhal number at various Reynolds numbers of the Elliptical wing 2.

In the graph of Figure 3.13 a), the average power seems to increase constantly with the increase of throttle independently of the airflow velocity. Despite this, the average power reduces with the increase of airflow velocity independently of the throttle position.

In Figure 3.13 b), with the increase of throttle and regardless of the Reynolds number, the dimensionless power seems to always decrease. Also, both Strouhal number and dimensionless power are lower for the higher Reynolds numbers.

3.3.3 Swallow wing m

It is shown in Figure 3.14, the graph of Average power vs Frequency and Dimensionless Power vs Strouhal number at various airflow velocities and Reynolds numbers for the Raven wing m.

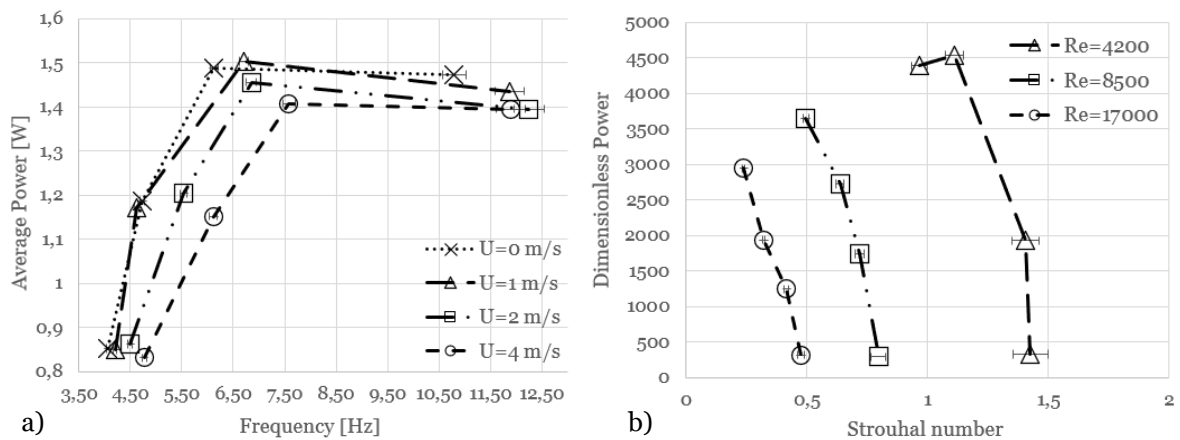


Figure 3.14: a) Average vs Frequency for various airflow velocities of the Swallow wing m. b) Dimensionless Power vs Strouhal number at different Reynolds numbers of the Swallow wing m.

As it is presented in Figure 3.14 a), the maximum of average power occurs for a throttle of 75% regardless of the airflow velocity. Also, independently of the throttle, the average power decreases for most cases.

On the other hand, dimensionless power and Strouhal number decrease with the increase of Reynolds in Figure 3.14 b). For the lower Reynolds numbers, the higher value is achieved at a throttle of 50%, while for the other two Reynolds numbers, it occurs at a throttle of 25%, decreasing then after.

3.3.4 Elliptical wing

In Figure 3.15 the graph of Average power vs Frequency and the graph of Dimensionless Power vs Strouhal number can be seen at multiple airflow velocities and Reynolds numbers respectively, for the Elliptical wing. Even though most of the outline of these graphs seems to be like the ones presented in Figure 3.14, it has a major difference on 75% and 100% throttle positions, at least for Figure 3.15 a) for an airflow velocity of 4 m/s. As it was mentioned before, a new wing was manufactured to perform these tests at the mentioned conditions, which can make those tests not viable.

Although, when compared with Elliptical wing 2 presented before, it was observed that their ranges are almost identical, even though if the Elliptical wing 2 presents a linear increase of the average power with frequency, while Elliptical wing increases differently.

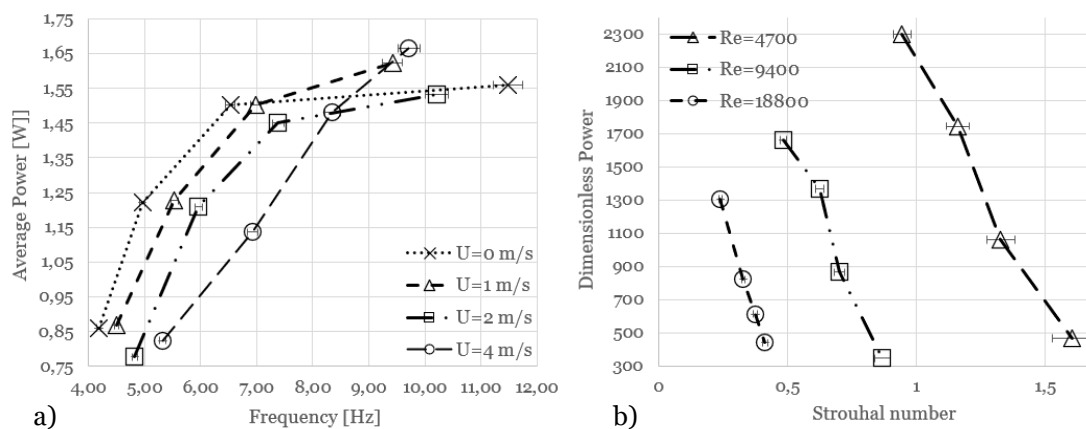


Figure 3.15: a) Average Power vs Frequency at different airflow velocities of Elliptical wing. b) Dimensionless Power vs Strouhal number of the Elliptical wing at various Reynolds numbers.

3.4 Wings Comparison

In this sub-chapter, a comparison between all wings (manufactured and the original) will be presented concerning average power, frequency, amplitude, dimensionless power, reduced frequency, dimensionless power, and dimensionless amplitude for the tested airflow velocities.

Before analyzing the results, it should be mentioned that all the manufactured wings had at least double the weight that the BionicBird original wing had, since it was impossible to achieve a manufacturing process similar to the one implemented on the BionicBird original wing. Despite that, the material of the membrane of the original wing is thinner than the used in the manufacturing process, and the spar material is also different and much heavier.

3.4.1 High-speed camera tests

This subsection contains both Figure 3.16 and Figure 3.17, each one of them with a set of 4 and 3 graphs, respectively. Amplitude vs Frequency for all wings and each of the airflow velocities will be shown in Figure 3.16, while in Figure 3.17, graphs of Dimensionless amplitude vs Reduced Frequency will be shown for all wings and the airflow velocities of 1, 2, and 4 m/s.

In the graphs of Figure 3.16, the higher amplitude belongs to the Swallow wing for a throttle of 50%, except for an airflow velocity of 4 m/s, where it also belongs to the Swallow wing but for a throttle of 75%. The minimum values of amplitude occur at a throttle of 100 (Rectangular wing 2) and 25% (Rectangular wing and Rectangular wing 2), for 0, 1, 2 m/s and for 4m/s respectively. It should also be referred that the increase of the airflow velocity seems to reduce amplitude values, being the higher ones the most affected.

Concerning the frequency, in Figure 3.16, the higher value of the 9 wings, always occurred for a throttle of 100% by the BionicBird original wing, while the manufactured wing that presents the higher frequency is at an airflow velocity of 0 m/s for the Elliptical wing, while for the airflow velocities of 1, 2 and 4 m/ they were achieved by Swallow wing m. The smaller values of the frequency were presented by Raven wing m, at 0 and 2 m/s, and Swallow wing m for 1 and 4 m/s, both wings at a throttle of 25%.

Besides this, the graphs also show the isolines of Strouhal numbers. As mentioned before, the optimal range of the Strouhal number for natural flyers is between 0.2 and 0.4 and it is seen that it happens for airflow velocity values of 2 and 4 m/s. For 2 m/s, the only wing within that range is the Rectangular wing for a throttle of 25%, while for 4 m/s most of the manufactured wings until at least until 75% throttle, except for Swallow wing, Swallow wing m and Elliptical wing 2, are within the range. On the other hand, the BionicBird wing seems to be in the optimal range only for a throttle of 25%. Rectangular wing, Rectangular wing 2 and Raven wing m are in the optimal range for every studied throttle position. It is noteworthy that even though the 0.2 to 0.4 was the optimal range observed in nature, it is just being used as a reference, since no propulsive efficiency was conducted.

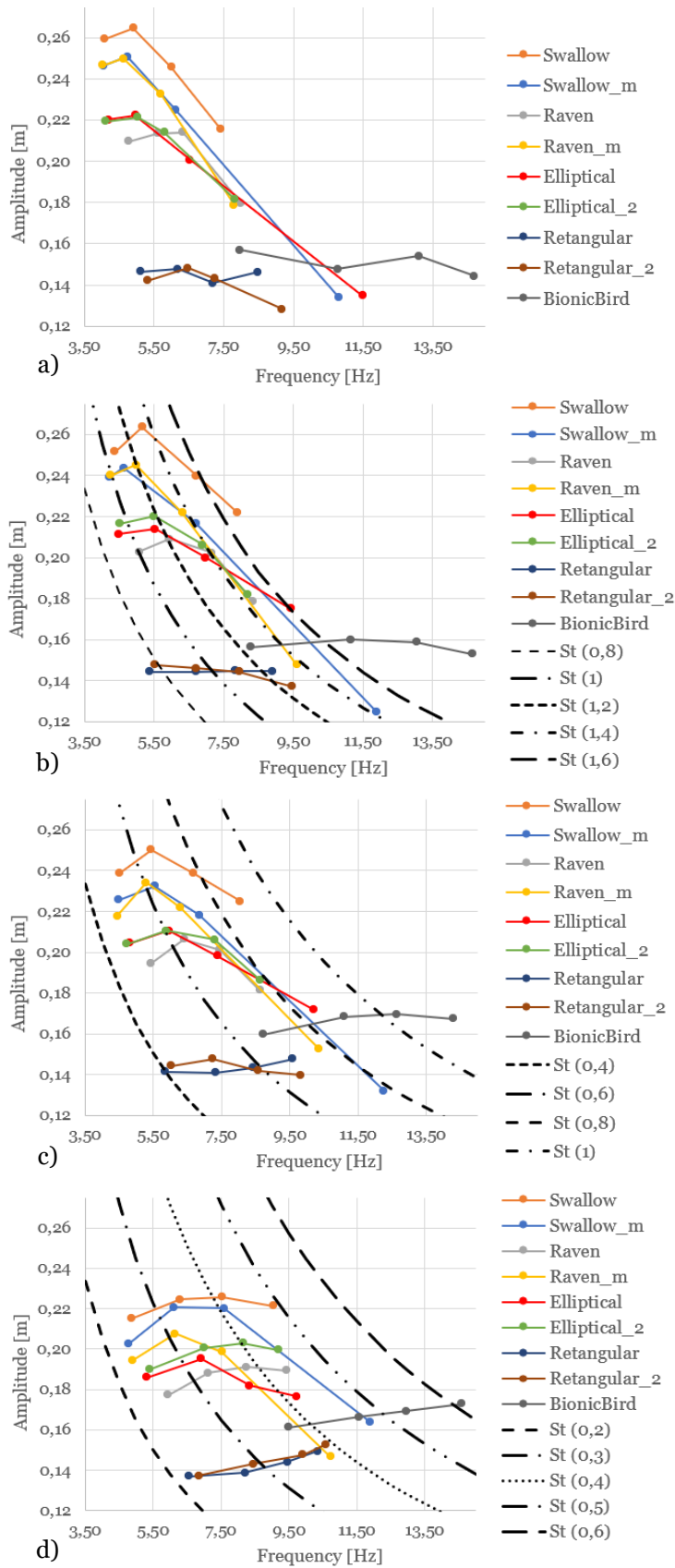


Figure 3.16: Amplitude vs Frequency for all wings for an airflow velocity of: a) 0 m/s. b) 1 m/s. c) 2 m/s. d) 4 m/s

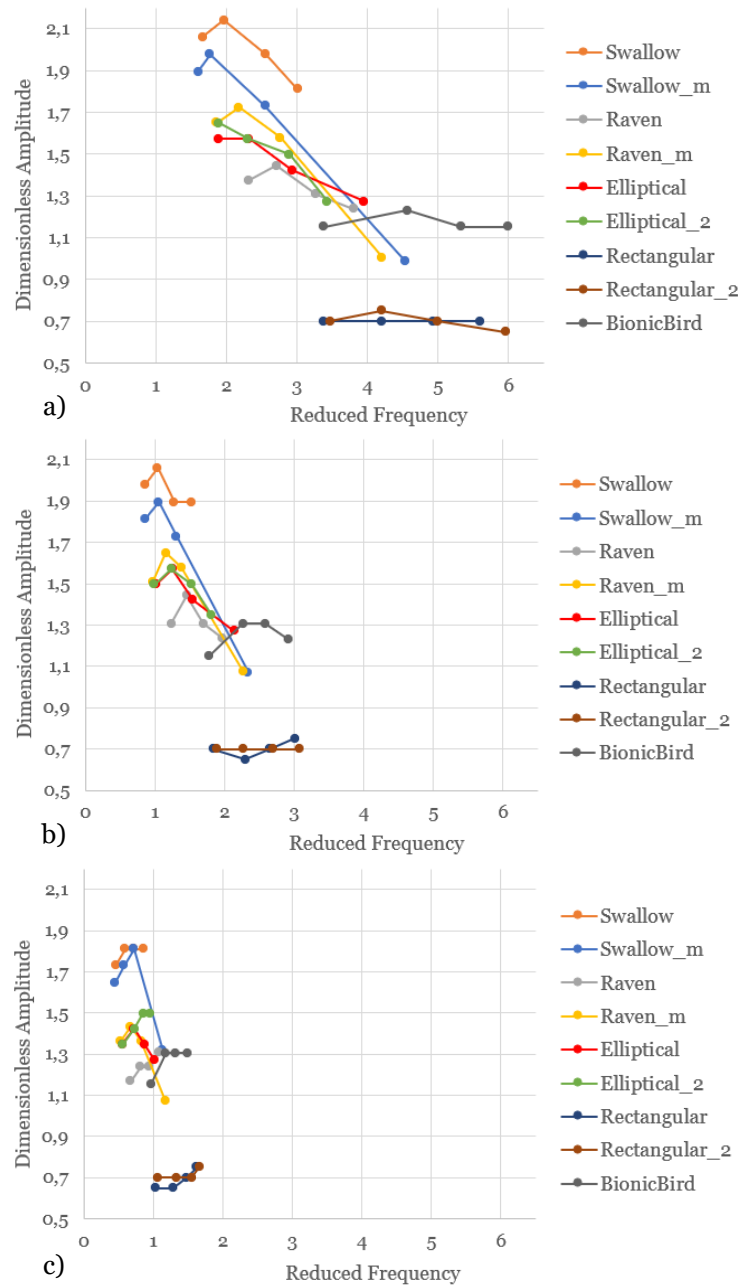


Figure 3.17: Dimensionless Amplitude vs Reduced Frequency, for all wings, at an airflow velocity of: a) 1 m/s. b) 2 m/s. c) 4 m/s.

The dimensionless amplitude, shown in Figure 3.17 seems to reduce with the increase of the airflow speed. Besides this, the higher values of dimensionless amplitude at a throttle of 50% by the Swallow wing for airflow velocities of 1 and 2 m/s, while for the 4 m/s it is from the Swallow wing (from a throttle of 50 to 100%) and the Swallow wing m at a throttle of 75%. For the lower dimensionless amplitudes, it is presented by the Rectangular wing 2 at an airflow velocity of 1 m/s and for a throttle of 100%. For an airflow velocity of 2 m/s at a throttle of 50% it is achieved by Rectangular wing, while for an airflow velocity of 4 m/s the rectangular wing also has the lower value but for two throttle positions of 25 and 50%.

For the values of reduced frequency, the lower one of the graphs of Figure 3.17, belongs to the Swallow wing at a throttle of 25%, regardless of the airflow velocity. Regarding the higher values of the reduced frequency, they seem to be achieved by the BionicBird original wing for an airflow velocity of 1 m/s, with the Rectangular wing 2 being the highest value for the manufactured wings, while for 2 and 4 m/s they are achieved by the Rectangular wing 2, both of them at a throttle of 100%.

3.4.2 Picoscope tests

In this last subsection, two sets of graphs will be presented into two Figures (Figure 3.18 and Figure 3.19), with the first one showing four graphs, one for each of the airflow velocity studied, of Average Power vs Frequency, and the second one displaying three graphs, for the airflow velocities of 1, 2 and 4 m/s, of Dimensionless Power vs Strouhal number.

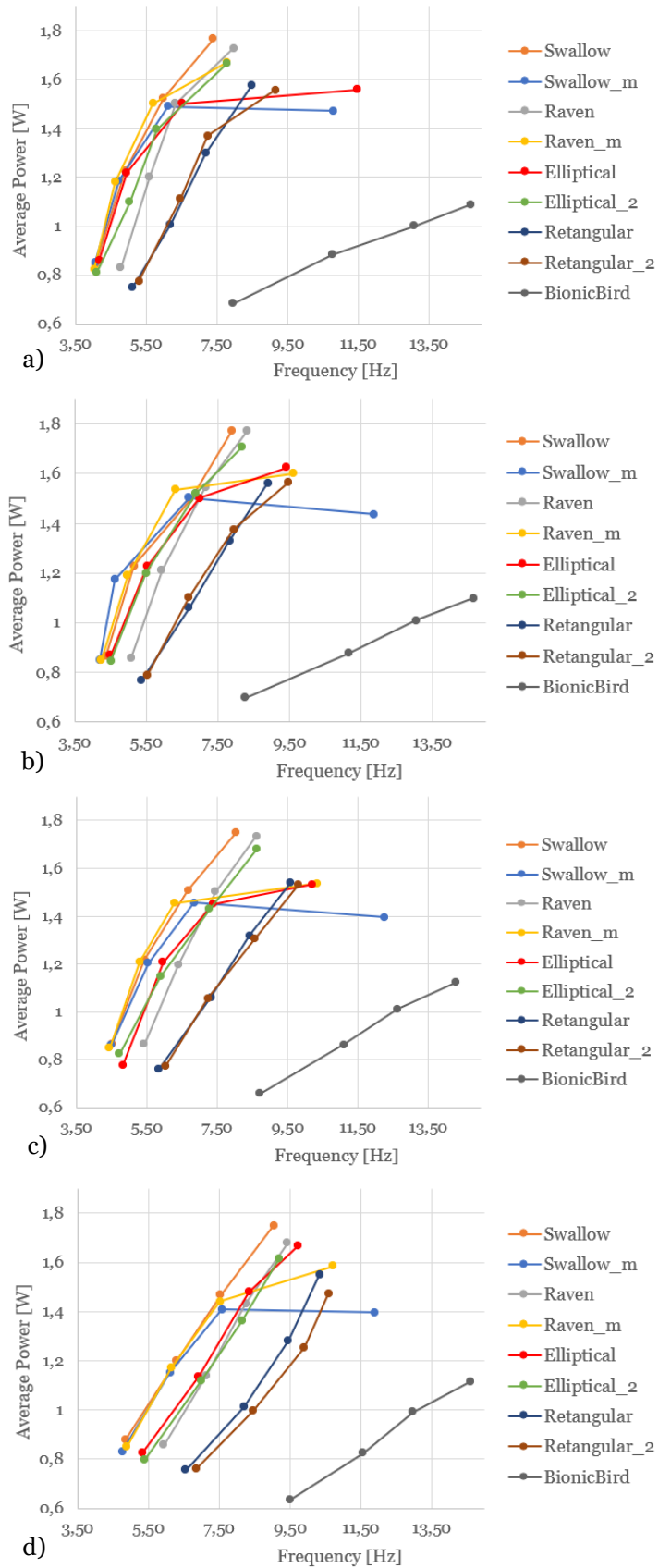


Figure 3.18: Average Power vs Frequency for all wings at an airflow velocity of: a) 0 m/s. b) 1 m/s. c) 2 m/s. d) 4 m/s.

As it is shown the bigger value of the average power, at a throttle of 100%, seems to be obtained by the Swallow wing for all the graphs of Figure 3.18, even though for an airflow velocity of 1 m/s, its value seems tied up with the maximum value of the Raven wing. Regarding the lower values of average power, they belong to the BionicBird original wing at a throttle of 25%, while to the manufactured wings it belongs to the Rectangular wing at a throttle of 25%. Also, it should be noted that the increase of the airflow velocity seems to reduce the P/f ratio, i.e., designed wings consumed fewer watts per hertz with the increase of the velocity.

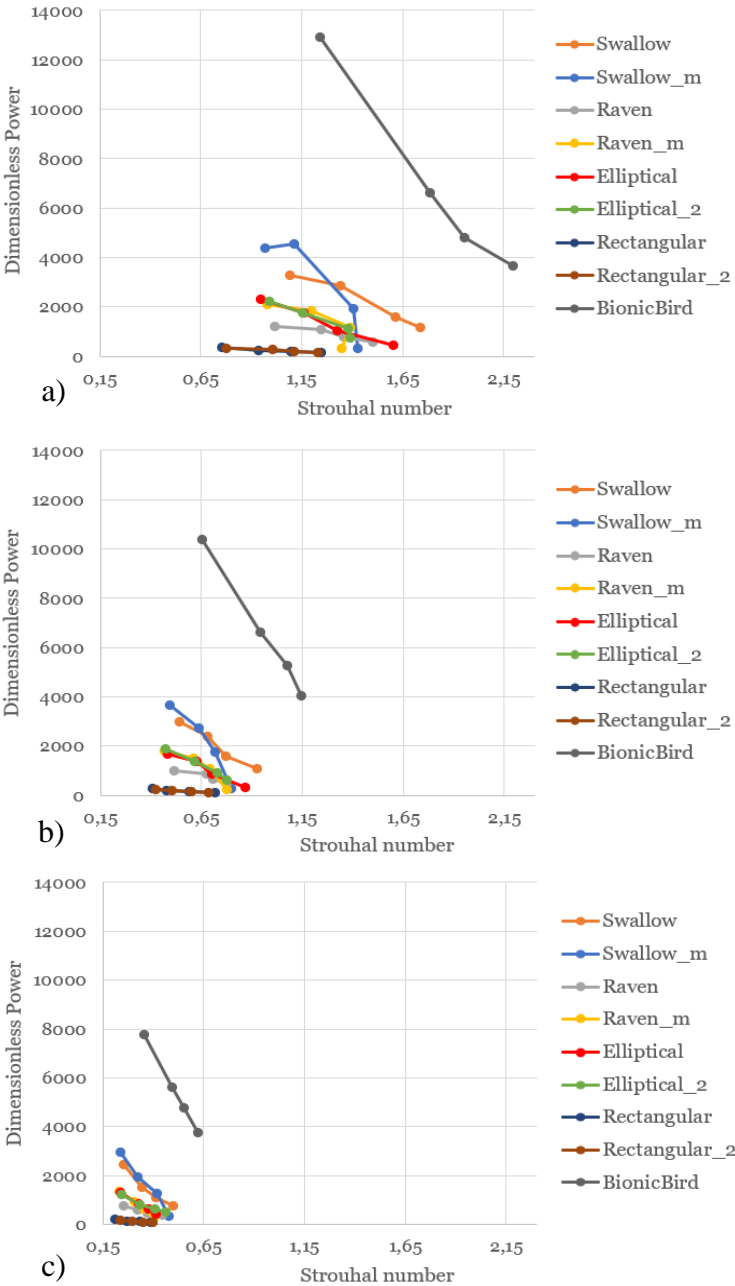


Figure 3.19: Dimensionless Power vs Strouhal, for all wings, at an airflow velocity of: a) 1 m/s. b) 2 m/s. c) 4 m/s.

Both dimensionless power and Strouhal number seem to reduce for all wings with the increase of the airflow velocity. Concerning the higher values of the dimensionless power it is presented by the BionicBird wings for all graphs in Figure 3.19, while when only considering manufactured wings the Swallow wing m presents the higher values for all the three graphs in Figure 3.19, even though if for an airflow velocity of 1 m/s it is at a throttle of 50% and for 2 and 4 m/s it is presented at a throttle of 25%. Regarding the minimum values at 1 and 2 and 4m/s, they seem to belong to a throttle position of 100% of the Rectangular wing and Rectangular wing 2.

For the bigger Strouhal numbers, they were achieved by the BionicBird original wing for a throttle of 100%. Concerning the manufactured wings the higher values were achieved by the Swallow wing, all at a throttle of 100% and for the graphs in Figure 3.19. On the other hand, the smaller values were shown by the Rectangular wing at a throttle of 25% in Figure 3.19.

Besides this it should be noted that the manufactured wings consume less power per oscillation with the increase of the airflow velocity, when compared to the BionicBird original wing.

Chapter 4

Conclusions and Future work

This last chapter is divided into two subchapters. In the first one, a conclusion of all the work performed during this study will be made, while on the second one future work will be proposed, as well as suggestions to improve the study.

4.1 Conclusions

The main objective of this dissertation was to evaluate the influence of geometrical parameters of the wing on their power when subjected to different airflow velocities. Also, the influence of the wing size, shape, and structure on amplitude, frequency, average power, reduced frequency, dimensionless amplitude, dimensionless power, and Strouhal number was studied. After that, a comparison between the wings was made to better evaluate the power of the manufactured wings and to determine the ones that got the higher or lower results in each one of the studied cases.

For this whole process, an experiment facility was built, along with an electrical system that was created in order to use the drone without any time limit of operation and to reliably obtain the average power. With this phase completed, and with the help of the high-speed camera, the visualization of the phenomenon was possible. Also, to vary the airflow velocity the wind tunnel was used along with its frequency controller.

The first part of the results was dedicated to the determination of the amplitude, and the frequency at different airflow velocities and their corresponding dimensionless parameters. Also, a comparison between the wings with different structural and design methods was performed. For the first pair of wings (Rectangular wing and Rectangular wing 2) the differences were not significant, while on the second pair of Elliptical wing, there was a difference of at least 0.05 m in the lowest amplitude range and 3 Hz in the higher frequency. Results regarding the third pair showed that the Raven wing m had the lowest and the higher values of 0.03 m and 0.04 m, respectively, although the bigger difference occurred in the dimensionless amplitude where Raven wing m exceeded Raven wing in 0.8. Finally for the fourth pair of wings, even though their difference concerning measures does not seem significant, when we observe the results, it shows that the Swallow wing m obtained a dimensionless amplitude 0.8 lower and a 3.5 Hz higher frequency than the Swallow wing.

Besides this, the second part of the results was devoted to the analysis of the average power, dimensionless power, and Strouhal number. Increasing Reynolds numbers decrease Strouhal numbers for all wings to a value that becomes closer to the optimal range of natural flyers, while the average power of the manufactured wings diminished with the increase of airflow speed, something that was not achieved by the BionicBird original wing for all throttle positions.

On the last part of the results, a comparison of all wings for all the considered parameters mentioned earlier was made. The Swallow wing was the one that achieved the higher amplitudes, higher dimensionless amplitudes, and higher average power for most cases, like it was showed before, while BionicBird original wing got the bigger frequencies, Strouhal numbers and dimensionless powers but smaller average power values. Concerning both Rectangular wing and Rectangular wing 2, and depending on the airflow velocity, they got the lower amplitudes, lower dimensionless amplitudes, lower Strouhal numbers, and higher values of reduced frequencies. The Swallow wing m achieved the higher frequencies for most airflow velocities, when only considering the non-manufactured wings. Regarding the lower frequencies, they were achieved by Raven wing m and Swallow wing m depending on the airflow velocity.

In conclusion, it is important to mention that the designed wings seem to consume fewer watts per hertz at higher airflow velocities since it was observed that the increase of the airflow velocity lowered the average power to frequency ratio. Despite this, the dimensionless power to Strouhal number ratio also seems to reduce with the increase of the airflow velocities. Also, the manufactured wings consume less power per oscillation with the increase of the airflow velocity.

4.2 Future work

On this last subchapter, some suggestions for future works are provided, to increase the knowledge about this subject and improve obtained results.

The first suggestion is to find a way to measure both thrust and lift of wings, and with that obtain propulsive efficiency to find the most efficient wing. Another suggestion would be to remake the tests but changing the main spar of the wings (Swallow, Swallow m, Raven, Raven m) and compare it with the obtained results. Also, some tests with different wing shapes and with the same design point would be interesting, or even try different materials or thinner membranes on the manufacturing process like a 2-micron mylar.

It should be noted that there is still a lack of studies on this area, and with the advance of technology, biomimetic drones will become more lightweight, and this will be an important area of study in a near future.

References

- [1] Goodheart, J. B. (2011). Tracing the History of the Ornithopter: Past, Present, and Future. *Journal of Aviation/Aerospace Education & Research*, 21(1). <https://doi.org/10.15394/jaaer.2011.1344>
- [2] Chin, D. D., Matloff, L. Y., Stowers, A. K., Tucci, E. R., & Lentink, D. (2017). Inspiration for wing design: How forelimb specialization enables active flight in modern vertebrates. *Journal of the Royal Society Interface*, 14(131). <https://doi.org/10.1098/rsif.2017.0240>
- [3] Shy, W., Yongsheng, L., Tang, J., Vileru, D., & Liu, H. (2007). *Aerodynamics of Low Reynolds Number Flyers*. 199 <https://doi.org/10.1017/CBO9780511551154>
- [4] Taylor, G. K., Nudds, R. L., & Thomas, A. L. R. (2003). *Flying and swimming animals cruise at a Strouhal number tuned for high power efficiency*. 707–711. <https://doi.org/10.1038/nature02000>.
- [5] Li, D., Zhao, S., Da Ronch, A., Xiang, J., Drofelnik, J., Li, Y., Zhang, L., Wu, Y., Kintscher, M., Monner, H. P., Rudenko, A., Guo, S., Yin, W., Kirn, J., Storm, S., & Breuker, R. De. (2018). A review of modelling and analysis of morphing wings. *Progress in Aerospace Sciences*, 100(September 2017), 46–62. <https://doi.org/10.1016/j.paerosci.2018.06.002>
- [6] Billingsley, D., Slipher, G., Grauer, J., & Hubbard, J. (2009). Testing of a passively morphing ornithopter wing. *AIAA Infotech at Aerospace Conference and Exhibit and AIAA Unmanned...Unlimited Conference, April*. <https://doi.org/10.2514/6.2009-1828>
- [7] Wissa, A. A., Tummala, Y., Hubbard, J. E., & Frecker, M. I. (2012). Passively morphing ornithopter wings constructed using a novel compliant spine: Design and testing. *Smart Materials and Structures*, 21(9). <https://doi.org/10.1088/0964-1726/21/9/094028>
- [8] Mueller, D., & Gerdes, J. W. (2009). D. Mueller, J. Gerdes, and S. K. Gupta. Incorporation of passive wing folding in flapping wing miniature air vehicles. ASME Mechanism and Robotics Conference, August 30-September 2. *Mechanical Engineering*. <https://doi.org/10.1115/DETC2009-87543>.
- [9] Stowers, A. K., & Lentink, D. (2015). Folding in and out: Passive morphing in flapping wings. *Bioinspiration and Biomimetics*, 10(2), 1–16. <https://doi.org/10.1088/1748-3190/10/2/025001>
- [10] Tanaka, H., Okada, H., Shimasue, Y., & Liu, H. (2015). Flexible flapping wings with self-organized microwrinkles. *Bioinspiration and Biomimetics*, 10(4), 46005. <https://doi.org/10.1088/1748-3190/10/4/046005>

- [11] Send, W., Fischer, M., Jebens, K., Mugrauer, R., Nagarathinam, A., & Scharstein, F. (2012). Artificial hinged-wing bird with active torsion and partially linear kinematics. *28th Congress of the International Council of the Aeronautical Sciences 2012, ICAS 2012, 2*, 1148–1157.
- [12] *SmartBird* | Festo Corporate. (n.d.). Retrieved December 3, 2020, from <https://www.festo.com/group/en/cms/10238.htm?fbclid=iwar2kttncywpangfzlyjlogbhjj-e-kfctniasjsamw6yorxd4twudsszgc>.
- [13] *BionicSwift* | Festo Corporate. (n.d.). Retrieved December 3, 2020, from <https://www.festo.com/group/en/cms/13787.htm?fbclid=iwar19o7zbhtcnl84qvomtcjynlp-bwhhoitfiguxlfyqznfkap8cspdcocyfo>.
- [14] Bunget, G., Seelecke, S., & Place, T. J. (2008). *Design and fabrication of a bio-inspired flight micro-air vehicle*. 1–8. ASME 2008, Conference on Smart Materials Adaptive Structures and Intelligent Systems.
- [15] Colorado, J., Barrientos, A., Rossi, C., & Breuer, K. S. (n.d.). *Biomechanics of smart wings in a bat robot: morphing wings using SMA actuators*. <https://doi.org/10.1088/1748-3182/7/3/036006>. *Bioinspiration & Biomimetics*, Vol.7, No.3.
- [16] *Bird Wing Shapes*. (n.d.). Retrieved June 14, 2020, from <http://www.paulnoll.com/Oregon/Birds/flight-shape.html>
- [17] Hassanalain, M., Abdelkefi, A., Wei, M., & Ziaei-Rad, S. (2017). A novel methodology for wing sizing of bio-inspired flapping wing micro air vehicles: theory and prototype. *Acta Mechanica*, *228*(3), 1097–1113. <https://doi.org/10.1007/s00707-016-1757-4>
- [18] Barata, J. M. M., Silva, T. J. A., Neves, F. M. S. P., & Silva, A. R. R. (2017). Experimental analysis of forces during take-off of birds. *AIAA Information Systems-AIAA Infotech at Aerospace*, *2017, January*, 1–8. <https://doi.org/10.2514/6.2017-1373>
- [19] Barata, J. M. M., Neves, F. M. S. P., Manquinho, P. A. R., & Silva, T. A. J. (2016). Propulsion for Biological Inspired Micro-Air Vehicles (MAVs). *Open Journal of Applied Sciences*, *06*(01), 7–15. <https://doi.org/10.4236/ojapps.2016.61002>
- [20] Pennycuik, C. J. (1996). Wingbeat frequency of birds in steady cruising flight: New data and improved predictions. *Journal of Experimental Biology*, *199*(7), 1613–1618.
- [21] Greenewalt, Crawford H. 1962. "Dimensional relationships for flying animals." *Smithsonian Miscellaneous Collections*. 144 (2)

- [22] Hu, H., Kvmar A. G., Abate, G., & Albertani, R. (2010). An experimental investigation on the aerodynamic performances of flexible membrane wings in flapping flight. *Aerospace Science and Technology*, 14(8), 575–586. <https://doi.org/10.1016/j.ast.2010.05.003>
- [23] Pornsin-sirirak, T. N., Tai, Y. C., Nassef, H., & Ho, C. M. (2001). *Titanium-alloy MEMS wing technology for a micro aerial vehicle application*. Sensors and Actuators A: Physical, Vol.89, No.1-2 pp. 95-103.
- [24] Ghommem, M., Hassanalian, M., Al-Marzooqi, M., Throneberry, G., & Abdelkefi, A. (2019). Sizing process, aerodynamic analysis, and experimental assessment of a biplane flapping wing nano air vehicle. *Proceedings of the Institution of Mechanical Engineers, Part G: Journal of Aerospace Engineering*, 233(15), 5618–5636. <https://doi.org/10.1177/0954410019852570>
- [25] Mazaheri, K., & Ebrahimi, A. (2010). Experimental study on interaction of aerodynamics with flexible wings of flapping vehicles in hovering and cruise flight. *Archive of Applied Mechanics*, 80(11), 1255–1269. <https://doi.org/10.1007/s00419-009-0360-8>
- [26] Mazaheri, K., & Ebrahimi, A. (2011). Experimental investigation on aerodynamic performance of a flapping wing vehicle in forward flight. *Journal of Fluids and Structures*, 27(4), 586–595. <https://doi.org/10.1016/j.jfluidstructs.2011.04.001>
- [27] Lin, C. S., Hwu, C., & Young, W. Bin. (2006). The thrust and lift of an ornithopter's membrane wings with simple flapping motion. *Aerospace Science and Technology*, 10(2), 111–119. <https://doi.org/10.1016/j.ast.2005.10.003>
- [28] Mueller, D., Bruck, H. A., & Gupta, S. K. (2010). Measurement of thrust and lift forces associated with drag of compliant flapping wing for micro air vehicles using a new test stand design. *Experimental Mechanics*, 50(6), 725–735. <https://doi.org/10.1007/s11340-009-9270-5>
- [29] Krashanitsa, R. Y., Silin, D., Shkarayev, S. V., & Abate, G. (2009). Flight Dynamics of a Flapping-Wing Air Vehicle. *International Journal of Micro Air Vehicles*, 1(1), 35–49. <https://doi.org/10.1260/1756-8293.1.1.35>
- [30] Yang, W., Wang, L., & Song, B. (2018). *Dove: A biomimetic flapping-wing micro air vehicle*. <https://doi.org/10.1177/1756829317734837>. International Journal of Micro Air vehicles, Vol.10 (1), 70-84.
- [31] Srigrarom, S., & Chan, W. L. (2015). Ornithopter type flapping wings for autonomous micro air vehicles. *Aerospace*, 2(2), 235–278. <https://doi.org/10.3390/aerospace2020235>

- [32] Park, J. H., & Yoon, K. (2008). *Designing a Biomimetic Ornithopter Capable of Sustained and Controlled Flight*. *Journal of Bionic Engineering*, Vol.5, No. 1, 39-47.
- [33] Mishra, S., Tripathi, B., Garg, S., Kumar, A., & Kumar, P. (2015). Design and Development of a Bio-Inspired Flapping Wing Type Micro Air Vehicle. *Procedia Materials Science*, 10(Cnt 2014), 519–526. <https://doi.org/10.1016/j.mspro.2015.06.001>
- [34] Altenbuchner, C., Hubbard, J. E., & Wissa, A. A. (2013). Free flight validation of a flexible-multi-body structural dynamics model of a bioinspired ornithopter. *51st AIAA Aerospace Sciences Meeting Including the New Horizons Forum and Aerospace Exposition 2013, January*, 1–16.
- [35] Hassanalian, M., & Abdelkefi, A. (2017). Methodologies for weight estimation of fixed and flapping wing micro air vehicles. *Meccanica*, 52(9), 2047–2068. <https://doi.org/10.1007/s11012-016-0568-y>
- [36] Pourtakdoust, S. H., & Aliabadi, S. K. (2012). Evaluation of flapping wing propulsion based on a new experimentally validated aeroelastic model. *Scientia Iranica*, 19(3), 472–482. <https://doi.org/10.1016/j.scient.2012.03.004>
- [37] Kim, D. K., Kim, H. Il, Han, J. H., & Kwon, K. J. (2008). Experimental investigation on the aerodynamic characteristics of a bio-mimetic flapping wing with macro-fiber composites. *Journal of Intelligent Material Systems and Structures*, 19(3), 423–431. <https://doi.org/10.1177/1045389X07083618>
- [38] Farmand-Ashtiani, E., Cugnoni, J., & Botsis, J. (2014). Experimental Mechanics of Composite, Hybrid, and Multifunctional Materials, Volume 6. *Conference Proceedings of the Society for Experimental Mechanics Series*, 6, 77–83. <https://doi.org/10.1007/978-3-319-00873-8>
- [38] Jackowski, Z. J. (2009). Design and construction of an autonomous ornithopter. *Thesis*. <http://18.7.29.232/handle/1721.1/52809>. Bachelor Thesis.
- [40] Floreano, D., Srinivasan, M. V., Zufferey, J. C., & Ellington, C. (2010). Flying insects and robots. *The Sealable Design of Flapping Micro-Air Vehicles Inspired by Insect Flight*, 185–205. <https://doi.org/10.1007/978-3-540-89393-6>
- [41] Hsu, C. K., Evans, J., Vytla, S., & Huang, P. G. (2010). Development of flapping wing Micro Air Vehicles-design, CFD, experiment and actual flight. *48th AIAA Aerospace Sciences Meeting Including the New Horizons Forum and Aerospace Exposition, January*, 1–11. <https://doi.org/10.2514/6.2010-1018>

- [42] Bejgerowski, W., Gerdes, J. W., Bruck, H. A., Wilkerson, S., & Gupta, S. K. (2010). *Design and fabrication of a multi-material compliant flapping wing drive mechanism for miniature air vehicles*. 301, 1–12. ASME 2010: International Design Engineering Technical Conferences and Computers and Information in Engineering Conference.
- [43] Nguyen, Q., Chan, W. L., & Debiassi, M. (2014). Design, Fabrication, and Performance Test of a Hovering-Based Flapping-Wing Micro Air Vehicle Capable of Sustained and Controlled Flight. *International Micro Air Vehicle Conference and Flight Competition*, 18–25. IMAV 2014. Delft, Netherlands.
- [44] Chand, A. N., Kawanishi, M., & Narikiyo, T. (2014). *Design Analysis, Modelling and Experimental Validation of a Bird-like Flapping-Wing Flying Robot*. 42–49. IMAV 2014: International Micro-Air Vehicles Conference and Competition.
- [45] Yang, L. J., Hsu, C. K., Ho, J. Y., & Feng, C. K. (2007). Flapping wings with PVDF sensors to modify the aerodynamic forces of a micro aerial vehicle. *Sensors and Actuators, A: Physical*, 139(1-2 SPEC. ISS.), 95–103. <https://doi.org/10.1016/j.sna.2007.03.026>
- [46] Grauer, J. A., & Hubbard, J. E. (2009). Inertial measurements from flight data of a flapping-wing ornithopter. *Journal of Guidance, Control, and Dynamics*, 32(1), 326–331. <https://doi.org/10.2514/1.37495>
- [47] Harmon, R. L., Grauer, J., Hubbard, J. E., Conroy, J., Humbert, S. J., Sitaraman, J., & Roge, B. (2008). Experimental determination of ornithopter membrane wing shapes used for simple aerodynamic modeling. *Collection of Technical Papers - AIAA Applied Aerodynamics Conference, August*, 1–17. <https://doi.org/10.2514/6.2008-6237>
- [48] Muniappan, A., Baskarand, V., & Duriyanandhan, V. (2005). Lift and thrust characteristics of flapping wing Micro Air Vehicle (MAV). *43rd AIAA Aerospace Sciences Meeting and Exhibit - Meeting Papers, January*, 4035–4045. <https://doi.org/10.2514/6.2005-1055>
- [49] Mahardika, N., Viet, N. Q., & Park, H. C. (2011). Effect of outer wing separation on lift and thrust generation in a flapping wing system. *Bioinspiration and Biomimetics*, 6(3). <https://doi.org/10.1088/1748-3182/6/3/036006>
- [50] Tsai, B. J., & Fu, Y. C. (2009). Design and aerodynamic analysis of a flapping-wing micro aerial vehicle. *Aerospace Science and Technology*, 13(7), 383–392. <https://doi.org/10.1016/j.ast.2009.07.007>
- [51] Moreira, H. (2010). An Experimental Study on the design of the ornithopter and tiltrotor configurations. *Master Thesis*. Inst. Superior Técnico, Technical Univ. of Lisbon, Portugal.

- [52] Croon, G. C. H. E. De, Clercq, K. M. E. De, Ruijsink, R., & Remes, B. (2009). *Design, aerodynamics, and vision-based control of the DelFly*. 1(2), 71–98.
- [53] Bakhtiari, A., Ehtemadi Haghighi, S., & Maghsoudpour, A. (2019). Experimental and analytical analysis of aerodynamic lift of an ornithopter at low and high angles of attack. *Proceedings of the Institution of Mechanical Engineers, Part G: Journal of Aerospace Engineering*, 233(6), 2023–2031. <https://doi.org/10.1177/0954410018771175>
- [54] Sika AG. (2013). *Biresin CR122 DataSheet*.
- [55] Riley Surface World. (1995). *Carbolite NR200F Bench Top Oven DataSheet*.
- [56] *Bionic bird - MetaFly-MetaBird, Biomimetic drones for indoor and outdoor*. (n.d.). Retrieved December 17, 2020, from <https://bionibird.com/world/?fbclid=iwar37aw4n2ne5z5mtk7qooszkruxyojarjrypvvsjxlzoukzhxsavdghv7fo>.
- [57] *Kaiser Videolight 6 1000 Watt 93304 - Video lights - Photopoint*. (n.d.). Retrieved December 19, 2020, from https://www.photopoint.ee/en/lightning/49322-kaiser-videolight-6-1000-watt93304?fbclid=iwarodcgqpxmg6tyhpf4z_osroijoajtznz3umci62avscos_nnho2pst-ig.
- [58] Technology Ltd, P. (2000). *Ultra-compact PC oscilloscopes PicoScope ® 2000 Series*. Retrieved December 19, 2020, from <https://www.picotech.com/download/datasheets/picoscope-2000-series-data-sheet.pdf?fbclid=iwarOghdkfgt1x1unvkdhxyjcvra5ybbhs-cqfu-fq634g9cawwopqltgrks>.
- [59] Bousson, K., Maia, N. F. L., & Lebres, A. S. (2011). Model Uncertainty Approach to Aircraft Angular Rate Estimation Using Kalman - Bucy Filtering. *International Review of Aerospace Engineering (I.RE.AS.E)*, 4(December), 307–314.
- [60] *1-D digital filter - MATLAB filter*. (n.d.). Retrieved January 21, 2021, from https://www.mathworks.com/help/matlab/ref/filter.html?fbclid=IwAR1SqAVb_PbojazLbZU7Hct-_BB7Lsbb7asRanSAyAztulv23IPNasGIFns

Appendix

Appendix A

Theta vs Frequency for the nine wings

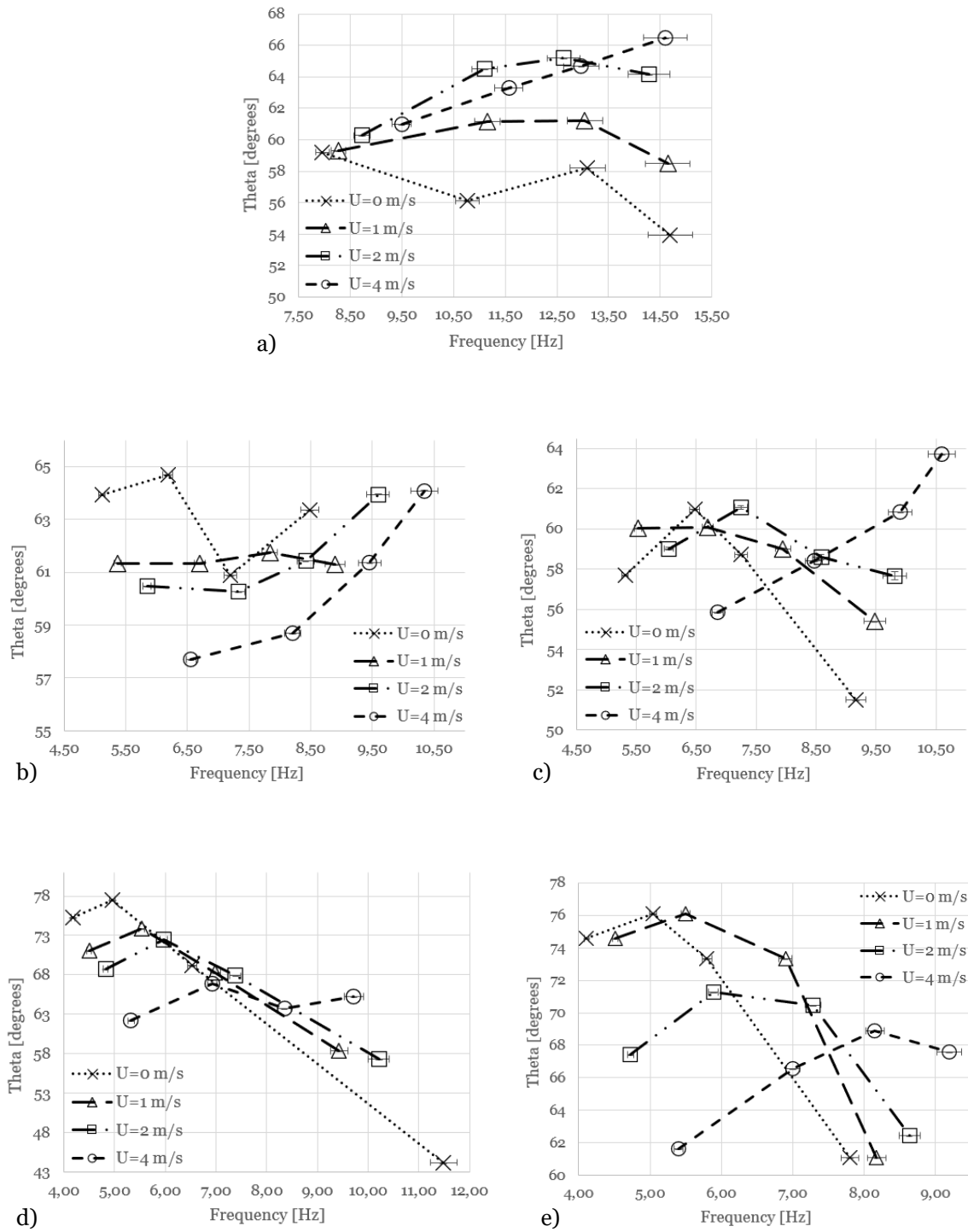


Figure A.1: Theta vs Frequency at different airflow velocities for: a) BionicBird original wing. b) Rectangular wing. c) Rectangular wing 2. d) Elliptical wing. e) Elliptical wing 2.

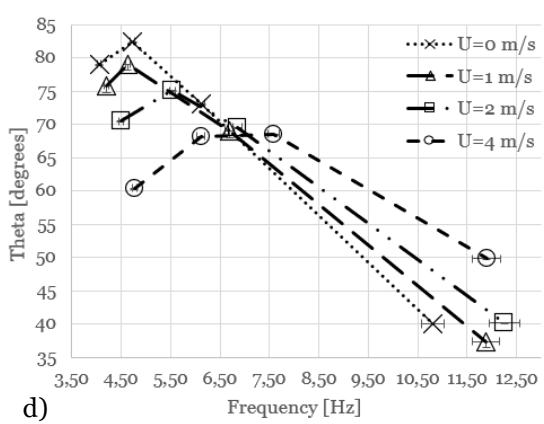
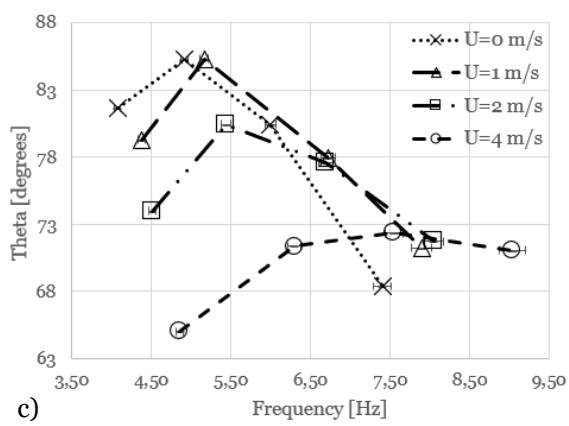
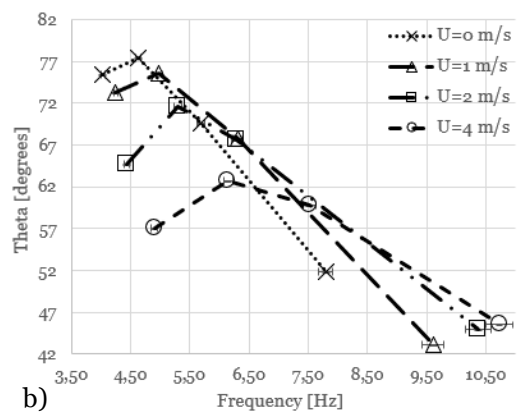
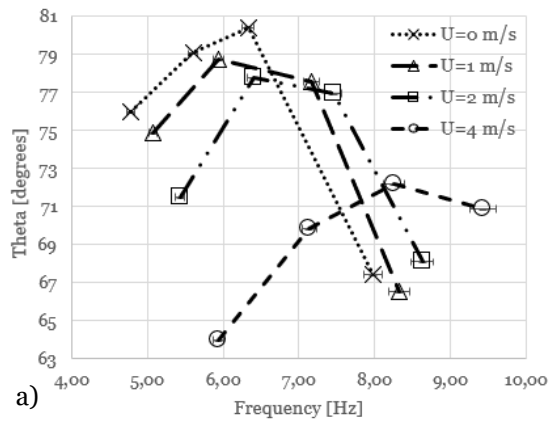


Figure A.2: Theta vs Frequency at different airflow velocities for: a) Raven wing. b) Raven wing m. c) Swallow wing. d) Swallow wing m

Appendix B

Dimensionless amplitude values at $U=0$ m/s for
the nine wings

Table B.1: Dimensionless amplitude for the 9 wings at $U = 0$ m/s.

	Throttle			
	25%	50%	75%	100%
BionicBird original wing	1,152	1,075	1,152	1,075
Rectangular wing	0,7	0,65	0,7	0,7
Rectangular wing 2	0,7	0,75	0,65	0,6
Elliptical wing	1,647	1,647	1,422	0,973
Elliptical wing 2	1,572	1,572	1,572	1,273
Raven wing	1,444	1,444	1,444	1,238
Raven wing m	1,793	1,793	1,65	1,291
Swallow wing	2,059	2,142	1,977	1,812
Swallow wing m	2,059	1,977	1,812	1,071

Appendix C

Average Power vs Frequency and
Dimensionless Power vs Strouhal number for
the nine wings

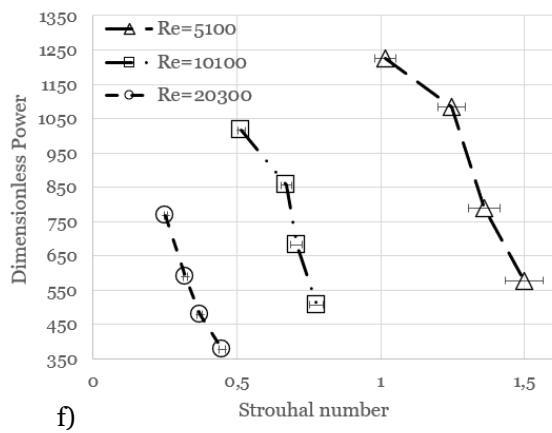
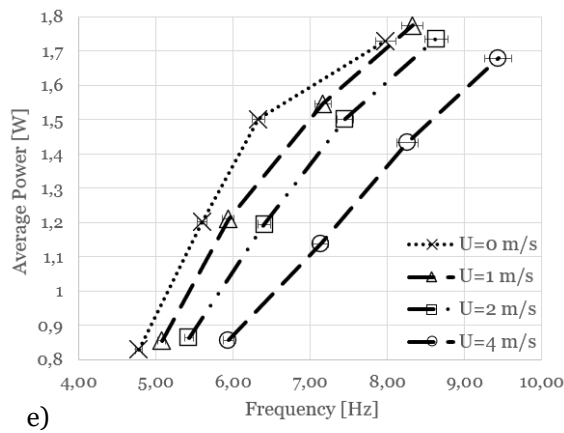
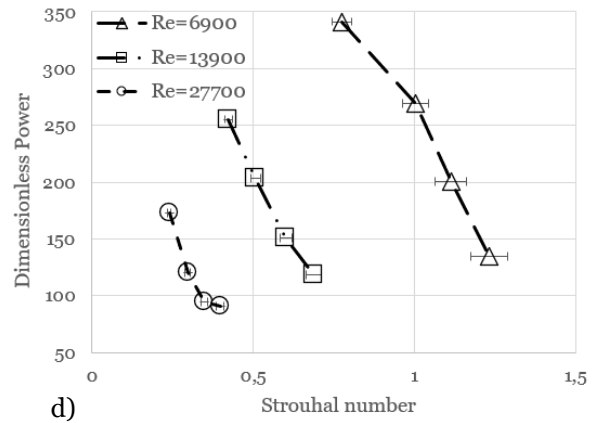
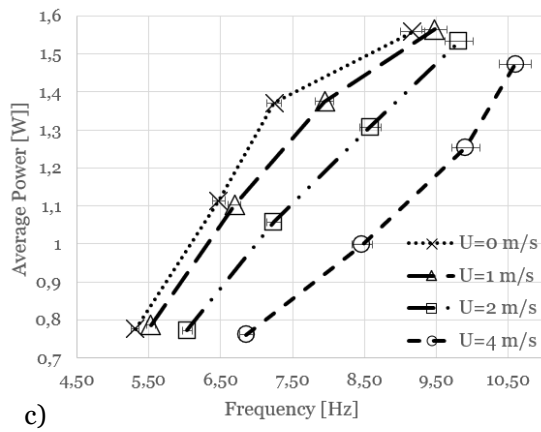
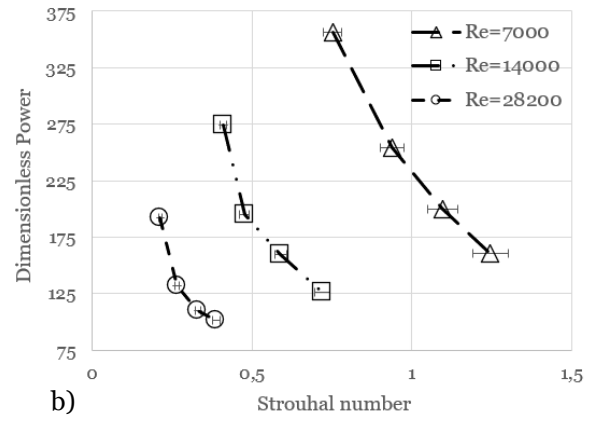
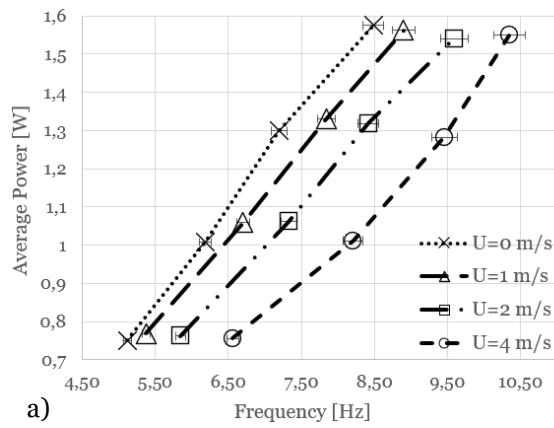


Figure C.1: a), c) and e): Average Power vs Frequency at different airflow velocities for Rectangular wing, Rectangular wing 2 and Raven wing, respectively. b), d) and f): Dimensionless Power vs Strouhal number for Rectangular wing, Rectangular wing 2 and Raven wing, respectively, at different Reynolds numbers.

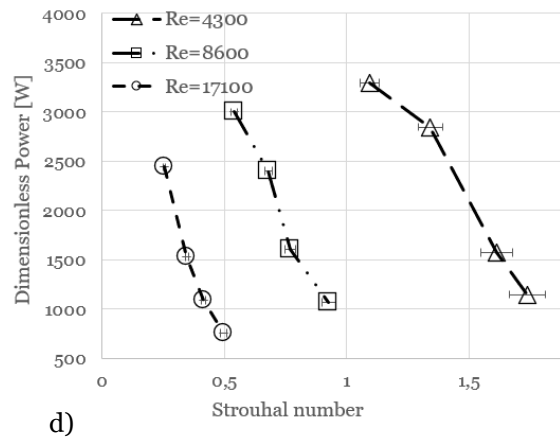
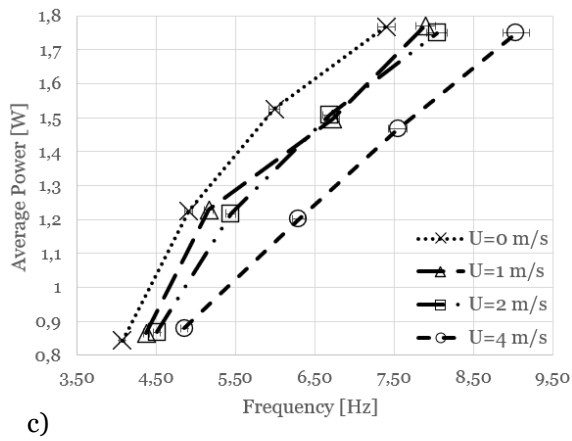
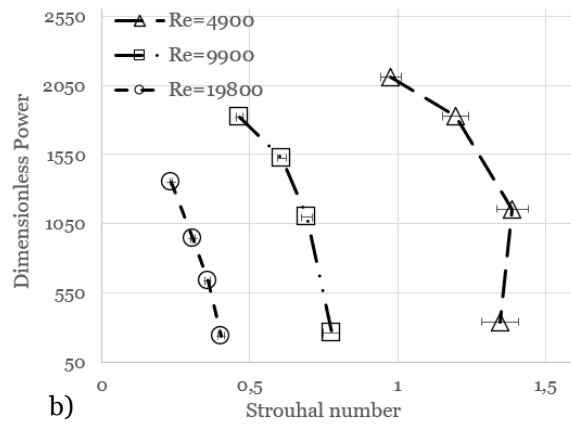
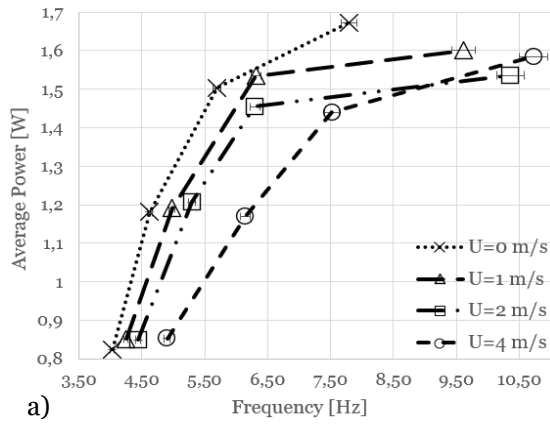


Figure C.2: a) and c): Average Power vs Frequency at different airflow velocities for Raven wing m and Swallow wing, respectively. b) and d): Dimensionless Power vs Strouhal number for Raven wing m and Swallow wing, respectively, at different Reynolds numbers.

Appendix D

Dimensionless power values at $U=0$ m/s for the
nine wings

Table D.1: Dimensionless power for the 9 wings at $U = 0$ m/s.

	Throttle			
	25%	50%	75%	100%
BionicBird original wing	14231,25	7425,66	4701,43	3613,94
Rectangular wing	408,83	310,70	254,11	188,11
Rectangular wing 2	377,63	300,07	263,42	148,19
Elliptical wing	2830,52	2412,74	1300,95	248,44
Elliptical wing 2	2810,58	2065,94	1731,44	845,06
Raven wing	1424,87	1281,42	1112,07	638,73
Raven wing m	2389,49	2271,94	1547,83	673,69
Swallow wing	3992,09	3315,35	2271,26	1395,09
Swallow wing m	4862,78	4307,06	2497,22	451,14